PROGRAMMABLE TWO-PORT POLARIZATION INDEPENDENT ELECTRO-OPTICALLY TUNABLE WAVELENGTH FILTER IN LITHIUM NIOBATE

A Dissertation

by

YANG PING

Submitted to the Office of Graduate Studies of
Texas A&M University
in partial fulfillment of the requirements for the degree of

DOCTOR OF PHILOSOPHY

December 2006

Major Subject: Electrical Engineering

PROGRAMMABLE TWO-PORT POLARIZATION INDEPENDENT ELECTRO-OPTICALLY TUNABLE WAVELENGTH FILTER IN LITHIUM NIOBATE

A Dissertation

by

YANG PING

Submitted to the Office of Graduate Studies of
Texas A&M University
in partial fulfillment of the requirements for the degree of

DOCTOR OF PHILOSOPHY

Approved by:

Chair of Committee,	Ohannes Eknoyan
Committee Members,	Chin B. Su
	Christi K. Madsen
	Donald R. Smith
Head of Department,	Costas N. Georghiades

December 2006

Major Subject: Electrical Engineering

ABSTRACT

Programmable Two-Port Polarization Independent Electro-Optically Tunable Wavelength Filter in Lithium Niobate. (December 2006)

Yang Ping, B.S., Tsinghua University;

M.S., Texas A&M University

Chair of Advisory Committee: Dr. Ohannes Eknoyan

Programmable two-port polarization independent electro-optically wavelength tunable filters based on asymmetric Mach-Zehnder structure in $LiNbO_3$ substrate have been developed for 1.55 μm application. The operation principle is based on Mach-Zehnder interference and TE↔TM polarization conversion. Fabrication parameters for channel waveguides, polarization converters and bandpass filters have been optimized. Straight channel waveguides 7 μm in width were produced by diffusing 1116 Å thick Ti into $LiNbO_3$ substrate at 1035°C for 10 hours. Single mode guiding has been realized for both TE and TM polarization. Insertion loss of 2.9 dB for TE polarization input and 3.3 dB for TM polarization input were achieved on a 46 mm long sample. Single sideband programmable polarization mode converters were produced with 16 electrode sets, each containing 64 grating periods. Programmability was achieved by applying spatially periodic weighted independent voltages to interdigital electrode sets, and controlled electronically via a personal computer through a digital-to-analog converter array chip. Maximum conversion efficiency of more than 99% was realized for both TM→TE and TE→TM, and was observed at 1530.48 nm. Two-port polarization independent

electro-optically tunable wavelength filters were produced based on the results obtained above. The 3 dB bandwidth is 1.1 nm and the nearest side lobes to the main transmission are down by about 9 dB for uniform coupling. Side lobes are reduced to about 20 dB below peak transmission after apodization, and the 3 dB bandwidths increased to ~ 1.3 nm as a result. Seven channels (channel -4, -2, -1, 0, +1, +2 and +4) were selectable by programming the voltages on each electrode set. Channel spacing is 1.1~1.2 nm. The tuning ranges from 1524.04 to 1533.56 nm. Fiber-to-fiber insertion loss of the filter at center frequency is 4.3 dB for TE input and 4.2 dB for TM input. The polarization dependent loss is < 0.5 dB for all selectable channels. The temporal response to a 21 V step change in applied voltages was measured to be 586 ns for the 10%-90% rise time and 2.308 μs for the 90%-10% fall time.

This research work provides a convenient scheme for making programmable two-port tunable bandpass filters and ROADMs.

To My Loved Ones

ACKNOWLEDGMENTS

I would like to express my gratitude to all those who helped me complete this dissertation. I want to thank Dr. Ohannes Eknoyan for serving as my committee chair and for his stimulating suggestions and encouragement during these past years. I would also like to thank Dr. Henry. F. Taylor for having discussions with me and giving valuable advice. Thanks to Dr. Chin B. Su and Dr. Christi K. Madsen for providing advice and help in addition to being on my committee. Thanks to Dr. Donald R. Smith for serving on my committee and helping with my dissertation.

I am grateful to Mr. Robert A. Atkins and Mr. James Gardner, for their technical training and support with my research. Without their help, this dissertation would never have been finished.

And needless to say, I am grateful to all of my friends and colleagues, Pingsheng, Donghua, Jane, Ohm, Niruth, Hsin-Hui, Zhaoxia, Ryoung-Han, Yong-Wook, Renato, Chao, Nick and Miao, for their friendship and help. I also appreciate Changdong, for helping me in testing the device.

I would like to give my special thanks to Bin for being with me every single moment and giving me support. And finally, I give thanks from the depth of my heart to my parents and my sister, for their love and encouragement throughout all these years.

TABLE OF CONTENTS

TABLE OF CONTENTS (Continued)

TABLE OF CONTENTS (Continued)

Page

LIST OF FIGURES

LIST OF FIGURES (Continued)

FIGURE Page

LIST OF FIGURES (Continued)

LIST OF TABLES

CHAPTER I

INTRODUCTION

With the recent rapid growth of Internet users and the simultaneous increase of new Internet applications, such as E-commerce and video conferencing, there is a pressing need to increase the transmission capacities of communication networks. The bandwidth of existing SONET and ATM networks is limited by the electronic bottlenecks. Recently, wavelength-division multiplexer (WDM) [1] systems were introduced in backbone links to remove this limit. By using WDM technologies, an optical fiber is capable of supporting multiple wavelength channels, each of which can operate at data rate of 10Gb/s or 40Gb/s. WDM technologies are still expanding to meet the new and unanticipated demand for network bandwidth.

A simple and important building block for WDM networks is the Optical Add/Drop Multiplexers (OADMs) [2], which are elements that are capable of adding and dropping wavelength (channels) from an optical link while preserving the integrity of other channels. In practice, OADM can operate in either static (fixed) mode or reconfigurable mode. Most OADM systems deployed in today's metro dense WDM (DWDM) networks are static. The channel scheme is fixed once these systems are established. Any changes to such static systems require removal or addition of built-in components, which results in errors and disruption in traffic during reconfiguration [3]. The Reconfigurable Optical Add/Drop Multiplexers (ROADMs) have the advantages of better cost effectiveness and

---

This thesis follows the style and format of *IEEE Journal of Lightwave Technology.*

flexibility than the static OADMs, because they enable carriers to provision individual wavelength on demand without changing the networks' physical configuration. ROADMs are seeing renewed interest in wake of the optical overbuilt today and they are viewed as a means to efficiently scale the underlying infrastructure. On September 24 2003, Verizon announced it has deployed Photuris V32000 in a multi-node network at Texas A&M University, which is the first publicly announced completed implementation of a ROADM for metro core/regional application in production network [4].

There are several different types of ROADM architecture. One architecture utilizes switches with a back-to-back multiplexer/demultiplexer to achieve add/drop functionality. Another ROADM type uses tunable optical filter to selectively add/drop a designated channel. The tuning based type is more cost effective, and we will focus on this kind of architecture. A number of optical filter approaches have been proposed and developed [5-7]. Based on the mechanisms of wavelength filtering, they can be grouped into three categories as the following [5]:

- Filters that are based on the wavelength dependence of interferometric phenomena, such as Fabry-Perot filters and Mach-Zehnder filters.
- Filters that are based on the wavelength dependence of coupling between orthogonal polarizations of optical fields induced by external perturbations, such as acousto-optic and electro-optic filters.
- Filters that are based on semiconductor resonant structures. Such devices are capable of providing gain as well as wavelength selectivity.

Different optical tunable filters exhibit different tuning speeds, from milliseconds to

nanoseconds. The slow-speed tunable filters are generally tuned by temperature or mechanical effect, they are in an advanced stage and many commercial technologies and devices are already available [6]. On the other hand most high-speed tunable filters are still in different research stages. Of these technologies, only EOTF [8, 9] can be tuned in sub-microsecond time periods, which is necessary for fast packet-switched networks [10] and can provide a relatively large tuning rate as well. EOTFs can be realized in ferroelectric birefringent materials like lithium tantalate ($LiTaO_3$) and lithium niobate ($LiNbO_3$). At Texas A&M University efforts have been directed towards EOTFs over the past few years to establish a foundation in this field. Several EOTF designs and devices have been proposed and demonstrated in $LiTaO_3$ and $LiNbO_3$ [11-15]. Wavelength tuning is accomplished by changing the refractive index of the waveguide through the linear electrooptic (Pockels) effect, where the change of the refractive index of the guiding optical medium is linearly proportional to an applied electrical field that is imposed through an external voltage.

A. Functional description of tunable WDM filters

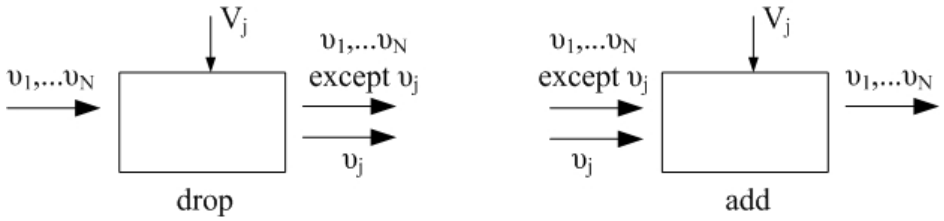

Fig. 1. Four-port spectral splitters.

The add/drop splitter is a type of ROADM which has recently become an important

WDM component. The four-port spectral splitters, which are schematically illustrated in Fig. 1, add or drop a subset of frequency channels from a larger set of N channels [16]. The two-port bandpass filter, as shown in Fig. 2, selects just a single WDM channel from a set of input channels. The applied voltage V_j in these two figures are varied to tune the frequency channel for adding, dropping or bandpassing.

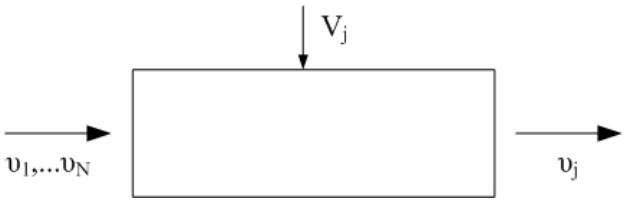

Fig. 2. Two-port bandpass filter.

B. Previous EOTF designs

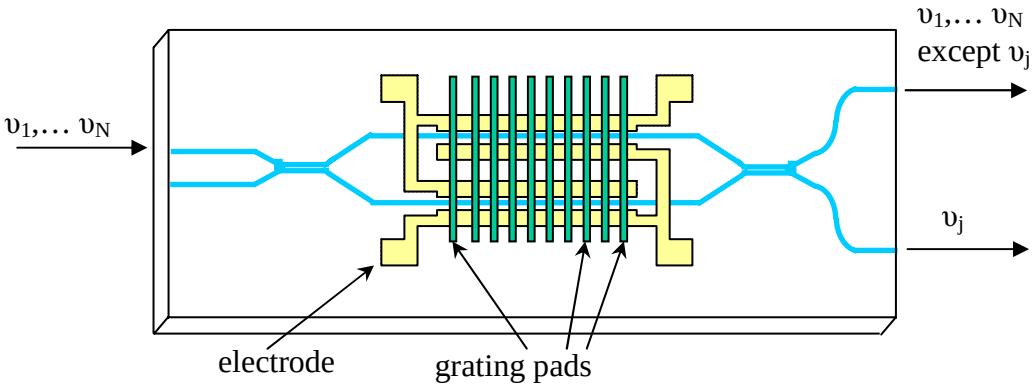

Fig. 3. Schematic illustration of a four-port ROADM.

EOTFs operating as four-port ROADM was demonstrated in $LiTaO_3$ [11], and $LiNbO_3$ [13, 14] whose structure is illustrated in Fig. 3. Single mode waveguides for both

TE and TM polarization are fabricated in birefringent electrooptic substrate ($LiNbO_3$) by titanium (Ti) in-diffusion. The two input and two output ports are separated by polarization beam splitters (PBSs) connected by middle waveguide regions in which polarization conversion and electrooptic tuning occurs. A spatially periodic strain-inducing dielectric film on the surface of the middle section produces polarization conversion through the strain-optic effect, and electrodes centered on the waveguides allow voltage tuning.

Wavelength selectivity is determined by the phase-matching condition described by

$$\Delta = \frac{2\pi\nu\left|n_{TM} - n_{TE}\right|}{c} \pm \frac{2\pi}{\Lambda}, \tag{1}$$

where Δ is the phase mismatch constant, υ is the optical frequency, n_{TE} and n_{TM} are the effective refractive indices of the waveguide, c is the light speed in free space and Λ is the spatial period of the grating pads. It follows that the deviation in frequency υ from the phase-matched frequency ν_0, corresponding to Δ=0, can be expressed as

$$\nu - \nu_0 = \frac{c\Delta}{2\pi\left|n_{TM} - n_{TE}\right|}, \tag{2}$$

and (n_{TM}-n_{TE}) is approximately equal to the difference in crystal refractive indices n_1-n_3.

Wavelength tuning is achieved by an applied voltage through the surface electrodes, which changes the birefringence $\left|n_{TM}-n_{TE}\right|$ via the Pockels effect in the waveguide arms and hence the wavelength for which the phase-matching condition is satisfied.

An alternative integrated optic design for the EOTF that does not require PBSs has been proposed [8] and demonstrated recently in $LiNbO_3$ substrate [15]. In this case, the PBSs are replaced by a new “relaxed beam splitter” RBS design. The RBS requirement is

that the sum of the power splitting ratio for TM incident light plus the power splitting ratio for TE incident light equals 1. The new design differs from the conventional designs in two other respects: (1) the interferometer is asymmetric with an optical path difference for the waveguides between the beam splitters of a half-wavelength, and (2) the relative positions of the polarization coupling regions in the two waveguides are displaced by half the spatial period of the perturbation responsible for the coupling. The new design can be used in implementing four-port ROADMs and is also applicable to a simple two-port bandpass filter with symmetric branch beam splitter (Fig. 4.). In this case, when an incident wavelength-multiplexed optical signal (λ_1, $\lambda_{2,}\ldots\lambda_n$) enters the input port, the intensity of the guided light splits into two equal parts at the first Y-branch which are directed toward the upper and lower mode converter regions. After passing through the polarization conversion/tuning sections, the mode fields recombine interferometrically at the second Y-branch. Only fields at the converted wavelength λ_j appear in phase and thus combine to emerge from the output port of the single mode channel waveguide, while all other λs radiate into the substrate.

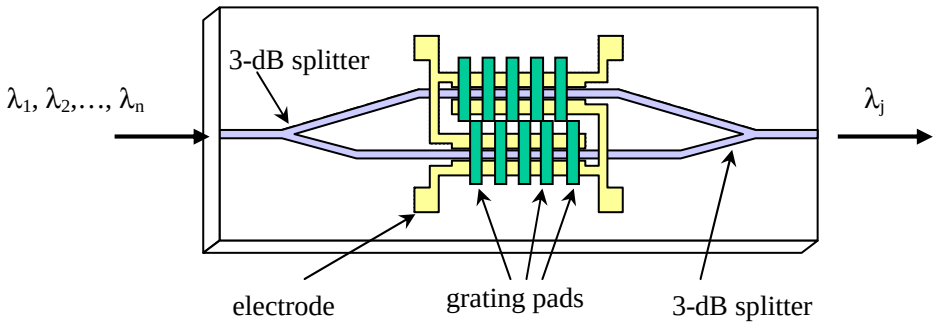

Fig. 4. Two-port bandpass wavelength filter.

Complete discussion on the EOTFs will be addressed in later parts.

C. Objectives

The primary objective of this project is to demonstrate a new family of components, the “electro-optic matched filter” (EMF), for wavelength switching in fiber optic networks. The EMF, which is a programmable EOTF device, can offer 1) rapid tuning speed to minimize the network access time; 2) wide tuning range to maximize the number of channels that can be selected in the optical network; 3) small crosstalk to avoid interference between adjacent channels. In this research, TE↔TM polarization converters and two-port channel selecting filters are demonstrated in x-cut $LiNbO_3$ substrate using EMF approach. The expected key features for EMF include fast tuning speed (< μs), potential for wide tuning range (>100 dense WDM channels), single chip integration, ability to select single or multiple channels, insensitivity to signal polarization, and low optical loss.

A brief theoretical review is given in Chapter II. An analysis of the EMFs followed by the device fabrication process is presented in Chapter III. Experimental results are discussed in Chapter IV. Finally, conclusions are summarized in Chapter V.

CHAPTER II

THEORETICAL REVIEW

In this chapter, a brief review of wave propagation properties and optical waveguides based on Maxwell's Equations is given. Optical indicatrix in uniaxial crystals is discussed and electro-optic effect is explained. Coupled mode theory is presented to describe TE↔TM mode conversion.

A. Wave propagation

Optical propagation inside a dielectric crystal is mainly a wave phenomenon. The governing equations for electromagnetic wave propagation are Maxwell's Equations:

$$\nabla \times \mathbf{E} = -\mu_0 \frac{\partial \mathbf{B}}{\partial t} \tag{3}$$

$$\nabla \times \mathbf{H} = \mathbf{J} + \frac{\partial \mathbf{D}}{\partial t} \tag{4}$$

$$\nabla \cdot \mathbf{D} = \rho \tag{5}$$

$$\nabla \cdot \mathbf{B} = 0 \tag{6}$$

and

$$\mathbf{D} = \varepsilon_0 \mathbf{E} + \mathbf{P} = \varepsilon \mathbf{E} \tag{7}$$

$$\mathbf{B} = \mu_0 (\mathbf{H} + \mathbf{M}) = \mu \mathbf{H} \tag{8}$$

where **E** and **H** represent electric and magnetic field vectors, **D** and **B** are the electric and magnetic displacement density vectors, **J** and ρ are current and charge densities, ε_0 and μ_0 are the permittivity and permeability of free space, **P** and **M** are the electric and magnetic

polarization of the medium, receptively. For source free homogeneous dielectric medium, **J** and ρ are zero, μ corresponds to the free space permeability constant, and ε is a diagonal matrix when a proper coordinate system is chosen and can be expressed as,

$$\boldsymbol{\varepsilon} = \begin{pmatrix} \varepsilon_1 & 0 & 0 \\ 0 & \varepsilon_2 & 0 \\ 0 & 0 & \varepsilon_3 \end{pmatrix}. \tag{9}$$

Taking the curl of both sides of equation (3), substituting **B** with equation (8), using $\nabla \times \nabla \times \mathbf{E} = \nabla(\nabla \cdot \mathrm{E}) - \nabla^2 \mathbf{E}$ and equations (4), (5), (7), yields

$$\nabla^2 \mathbf{E} - \varepsilon \mu_0 \frac{\partial^2 \mathbf{E}}{\partial t^2} = 0. \tag{10}$$

For a monochromatic wave with angular frequency ω, the electric field **E** should take the form

$$\mathbf{E}(\mathbf{r}, t) = \mathbf{E}(\mathbf{r}) e^{-i\omega t}. \tag{11}$$

Equation (10) can be rewritten using equation (11) as

$$\nabla^2 \mathbf{E}(\mathbf{r}) + k_0^2 n^2 \mathbf{E}(\mathbf{r}) = 0 \tag{12}$$

where $k_0 = \omega / c$ is the propagation constant in free space and $n = \sqrt{\varepsilon_r \mu_r}$ is the refractive index of the material.

B. Optical waveguides

An optical waveguide is generally a thin high refractive index layer surrounded by lower refractive index materials. A simple case is the step-index infinite planar slab waveguide in dielectric materials, which is depicted in Fig. 5.

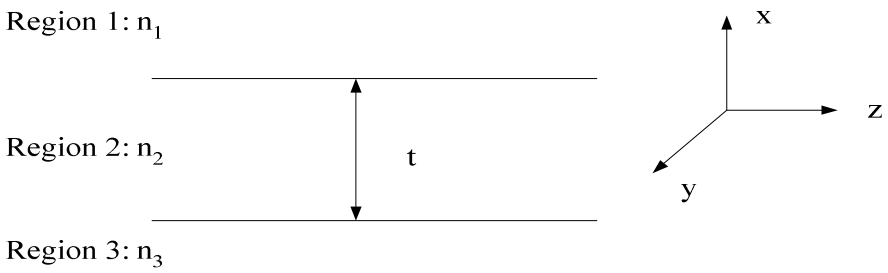

Fig. 5. Planar dielectric waveguide structure.

A mode in such a waveguide at a given frequency is described by a solution of equation (12). The solutions are subject to the electromagnetic boundary conditions at the interface between two dielectrics [17]:

$$\begin{aligned} E_{1t} &= E_{2t} \\ H_{1t} &= H_{2t} \\ D_{1n} &= D_{2n} \\ B_{1n} &= B_{2n}. \end{aligned} \tag{13}$$

Consider the case of z-propagating wave with propagation constant β and no y variation, which is shown in Fig. 5, and applying equation (13) to equation (12) and the waveguide structure, yields [18]

$$\begin{aligned} \text{Region 1: } & \frac{\partial^2}{\partial x}E(x) + [k_0{}^2 n_1{}^2 - \beta^2]E(x) = 0 \\ \text{Region 2: } & \frac{\partial^2}{\partial x}E(x) + [k_0{}^2 n_2{}^2 - \beta^2]E(x) = 0 \\ \text{Region 3: } & \frac{\partial^2}{\partial x}E(x) + [k_0{}^2 n_3{}^2 - \beta^2]E(x) = 0 \end{aligned} \tag{14}$$

where E(x) is either an x- or y- component of E(x).

Assuming $n_2 > n_3 > n_1$, the characteristics of waveguide modes can be analyzed by considering various β values. In the range of $\beta < k_0 n_1$, the solution of E(x) is sinusoidal in

all the three regions. This is called radiation mode and the wave is therefore not guided.

For $k_0n_1<\beta<k_0n_3$, solutions in region 2 and 3 are sinusoidal and are exponentially decaying in region1. This is commonly referred to as substrate radiation modes.

When $k_0n_3<\beta< k_0n_2$, the solution is sinusoidal in region 2 and exponential in region 1 and 3, making it possible to have a bounded solution for E(x) in the middle region that satisfies the boundary conditions and decays in the outer regions. The optical wave in this case is confined to the middle layer and its vicinity. Thus, these are guided modes.

The final case, $\beta>k_0n_2$, yields a solution where the field distribution increases exponentially away from the waveguide, which is not realizable.

The optical field distributions of all above cases are illustrated in Fig. 6.

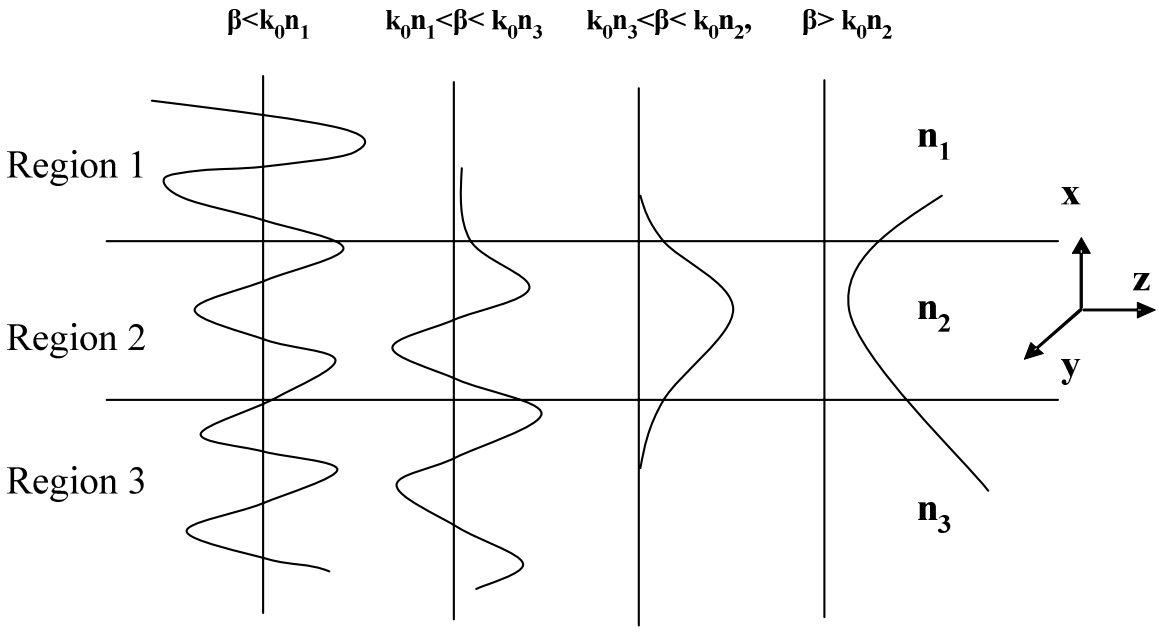

Fig. 6. The electrical field distributions corresponding to different values of β in a three-layer waveguide with $n_2>n_3>n_1$.

From the above discussion, it is clear that the condition for the existence of a guided mode in a planar slab dielectric waveguide with $n_2>n_3>n_1$ is

$$k_0 n_3 < \beta < k_0 n_2. \tag{15}$$

This also implies that confined modes are possible only when $n_2>n_3, n_1$, that is, the inner layer has a large refractive index than that of outside layers.

Table 1. Summary of field components for slab waveguides
($\phi(x)$ stands for E_y in TE modes or H_y in TM mode).

TE Modes	TM Modes
$E_z = 0$	$H_z = 0$
$E_x = 0$	$H_x = 0$
$H_y = 0$	$E_y = 0$
$E_y = \phi(x)$	$H_y = \phi(x)$
$H_x = -\frac{\beta}{k}\sqrt{\frac{\varepsilon_0}{\mu_0}}\varphi(x)$	$E_x = \frac{\beta}{k}\frac{1}{n^2}\sqrt{\frac{\mu_0}{\varepsilon_0}}\varphi(x)$
$H_z = -\frac{i}{k}\sqrt{\frac{\varepsilon_0}{\mu_0}}\varphi'(x)$	$E_z = \frac{i}{k}\frac{1}{n^2}\sqrt{\frac{\mu_0}{\varepsilon_0}}\varphi'(x)$

The waveguide structure shown in Fig. 1 can generally support a finite number of guided modes, which can be further divided into two groups based on the polarization directions. One is called transverse electric (TE) mode, the other is called transverse magnetic (TM) mode. When a plane wave with TE or TM polarization is incident on the dielectric core-cladding interface, the reflected and transmitted waves maintain the TE or TM polarization. Therefore, there is no mixing between TE or TM components in the propagation. The field components for the TE and TM modes of the slab waveguide are summarized in Table 1 [19].

C. Optical indicatrix in uniaxial crystals and electro-optic effect

The refractive index n defined in section **A** is usually a constant for isotropic materials, but it is direction and polarization dependent for anisotropic materials due to the fact that $\boldsymbol{\varepsilon}$ is a 3×3 matrix. The refractive index for a specific direction and polarization in an anisotropic material can be derived from the following equation [18]

$$\frac{x^2}{n_x^2}+\frac{y^2}{n_y^2}+\frac{z^2}{n_z^2}=1 \tag{16}$$

where x, y and z are the principal dielectric axes, that is, the directions in the crystal along which **D** and **E** are parallel. n_x, n_y and n_z are the refractive indexes along x, y and z axis respectively. In uniaxial crystals, such as $LiNbO_3$ and $LiTaO_3$, $n_x=n_y=n_o$ and $n_z=n_e$, equation (16) can be simplified as

$$\frac{x^2}{n_o^2}+\frac{y^2}{n_o^2}+\frac{z^2}{n_e^2}=1 \tag{17}$$

where the index ellipsoid is rotary symmetrical with respect to the z axis, which is also called the optic axis.

Fig. 7 illustrates the wave propagation in a uniaxial crystal. The direction of propagation is along **k**. Because of the circular symmetry about z axis, one can choose the y axis to coincide with the projection of **k** vector on the x-y plane without loss of generality. The intersection ellipse of the plane normal to **k** with the ellipsoid is shaded in the Fig. 7. The two polarization eigen states of **D** are parallel to the major and minor axes of the ellipse, and are said to be extraordinary wave (D_e) and ordinary wave (D_o),

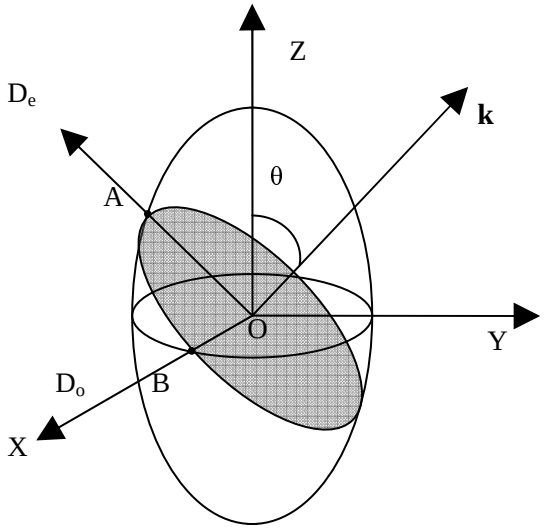

Fig. 7. Index ellipsoid of uniaxial crystals.

respectively. The length of the semi-major axis OA equals to the refractive index $n_e(\theta)$ for extraordinary wave, whereas OB which equals n_o is the one for the ordinary wave. Fig. 7 also indicates that the polarization direction and the refractive index of ordinary wave remain unchanged with respect to change of θ, which is the angle between the optic axis and the propagation direction **k**, while those of the extraordinary wave are dependent on θ.

The index of extraordinary wave is equal to OA in the Fig. 3, and is given by

$$\frac{1}{n_e^2(\theta)} = \frac{\sin^2(\theta)}{n_e^2} + \frac{\cos^2(\theta)}{n_o^2}. \tag{18}$$

In section B it was stated that, given a direction in a crystal, in general there exist two possible linearly polarized modes (TE and TM). Each mode possesses a unique polarization direction and a corresponding effective mode index of refraction (i.e., a velocity of propagation) [18], which can be easily found through equation (14).

The linear electro-optic (Pockels) effect, which is the basis for active waveguide device control, provides a change in refractive index proportional to the applied electric field [20]. The effect of an electric field on the propagation is expressed most conveniently by giving the changes in the constants $\frac{1}{n_x^2}, \frac{1}{n_y^2}, \frac{1}{n_z^2}$ of the index ellipsoid. The equation of the index ellipsoid in the presence of an electric field is expressed as [18]

$$\left(\frac{1}{n^2}\right)_1 x^2 + \left(\frac{1}{n^2}\right)_2 y^2 + \left(\frac{1}{n^2}\right)_3 z^2 + \left(\frac{1}{n^2}\right)_4 yz + \left(\frac{1}{n^2}\right)_5 xz + \left(\frac{1}{n^2}\right)_6 xy = 1. \qquad (19)$$

With zero applied electric field, equation (19) reduces to (16), i.e.

$$\left(\frac{1}{n^2}\right)_1 \Big|_{E=0} = \frac{1}{n_x^2}, \left(\frac{1}{n^2}\right)_2 \Big|_{E=0} = \frac{1}{n_y^2}, \left(\frac{1}{n^2}\right)_3 \Big|_{E=0} = \frac{1}{n_z^2},$$

$$\left(\frac{1}{n^2}\right)_4 \Big|_{E=0} = \left(\frac{1}{n^2}\right)_5 \Big|_{E=0} = \left(\frac{1}{n^2}\right)_6 \Big|_{E=0} = 0.$$

The linear change in the coefficients of the index ellipsoid due to an applied electric field (E_j^e) along the principle crystal axis is defined by

$$\Delta\left(\frac{1}{n^2}\right)_i = \sum_{j=1}^{3} r_{ij} E_j^e, \qquad (20)$$

where i=1,2,…,6 and r_{ij} is a 6×3 electro-optic tensor.

In $LiNbO_3$, $n_x=n_y=n_o$ and $n_z=n_e$ in equation (16) and the electro-optic tensor is [21]

$$\begin{bmatrix} 0 & -r_{22} & r_{13} \\ 0 & r_{22} & r_{13} \\ 0 & 0 & r_{33} \\ 0 & r_{51} & 0 \\ r_{51} & 0 & 0 \\ -r_{22} & 0 & 0 \end{bmatrix}. \qquad (21)$$

If only a z-directed electric field E_z exists in the $LiNbO_3$ crystal (Fig. 7), the modified refractive index become

$$\frac{1}{n_{x'}^2} = \frac{1}{n_o^2} + r_{13}E_z^e. \tag{22}$$

For $LiNbO_3$, $r_{13} = 8.6\times10^{-12}\ \mathrm{m/V}$, $r_{33} = 30.8\times10^{-12}\ \mathrm{m/V}$, n_o=2.29, n_e=2.20 (for λ=1.4μm, at 24.5 °C) [22]. Assuming $r_{13}E_z << n_o^{-2}$ and $r_{33}E_z << n_e^{-2}$, using the differential relation

$$dn = -\left(\frac{n^3}{2}\right)d\left(\frac{1}{n^2}\right),$$

yields

$$n_{x'} = n_o - \frac{n_o^3}{2}r_{13}E_z^e, \tag{23}$$

and similarly,

$$n_{y'} = n_o - \frac{n_o^3}{2}r_{13}E_z^e, \tag{24}$$

$$n_{z'} = n_e - \frac{n_e^3}{2}r_{33}E_z^e. \tag{25}$$

The superscript “e” is to indicate that this field component relates to the applied electrical voltage.

D. TE↔TM mode conversion

In a uniform optical waveguide without perturbation, modes satisfy the wave equation (8). By means of refractive index perturbation, a TE polarized optical wave may

convert to a TM polarized optical wave and vice versa.

D-1. The effects of electrical perturbation

The basic characteristics of TE↔TM mode conversion can be described using small perturbation of the dielectric medium polarization vector **P**, and examining its effect on the time dependent wave equation [23]. Below is the wave equation in a dielectric medium

$$\nabla^2\mathbf{E}(\mathbf{r},t)=\mu\varepsilon(r)\frac{\partial^2\mathbf{E}(\mathbf{r},t)}{\partial t^2}. \tag{26}$$

Using equation (7), (26) yields the following

$$\nabla^2\mathbf{E}(\mathbf{r},t)=\mu\varepsilon_0\frac{\partial^2\mathbf{E}(\mathbf{r},t)}{\partial t^2}+\mu\frac{\partial^2\mathbf{P}(\mathbf{r},t)}{\partial t^2}. \tag{27}$$

The total medium polarization can be taken as the sum

$$\mathbf{P}(\mathbf{r},t)=\mathbf{P}_0(\mathbf{r},t)+\mathbf{P}_{\text{pert}}(\mathbf{r},t) \tag{28}$$

where

$$\mathbf{P}_0(\mathbf{r},t)=[\varepsilon(\mathbf{r})-\varepsilon_0]\mathbf{E}(\mathbf{r},t) \tag{29}$$

is the polarization induced by $\mathbf{E(r},t\mathbf{)}$ in the unperturbed waveguide whose dielectric constant is $\varepsilon\mathbf{(r)}$. Using equation (28) and (29), equation (27) gives

$$\nabla^2\,\mathrm{E}_i(\mathbf{r},t)-\mu\varepsilon(\mathbf{r})\frac{\partial^2\,\mathrm{E}_i(\mathbf{r},t)}{\partial t^2}=\mu\frac{\partial^2}{\partial t^2}[\mathbf{P}_{\text{pert}}(\mathbf{r},t)]_i \tag{30}$$

where i represents either x, y or z.

In the case of x-cut y-propagation waveguide as shown in Fig. 8, TE polarized optical mode has transverse electrical field distribution in the z direction while TM mode

has transverse electrical field distribution in the x direction. From equation (30), a z-directed perturbation induced medium polarization (P_z) is required for TM→TE coupling, and an x-directed perturbation induced medium polarization (P_x) is needed to achieve TE→TM coupling. In order to produce TE↔TM mode conversion, both of these conditions should be fulfilled.

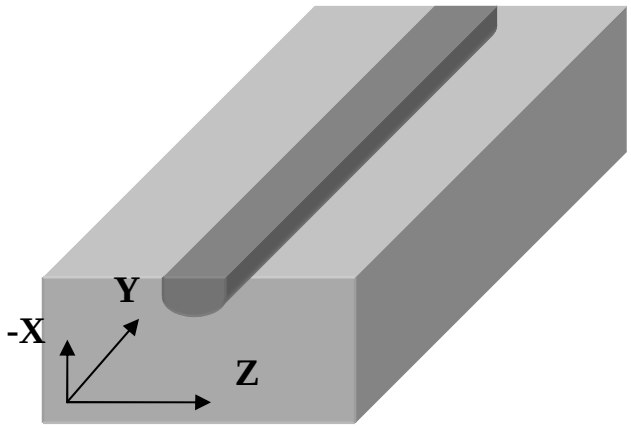

Fig. 8. An x-cut y-propagation Ti:$LiNbO_3$ waveguide.

Considering the z component of equation (7) only, it follows that

$$D_3 = \sum_{j=1}^{3} \varepsilon_{3j} E_j = \varepsilon_0 E_3 + P_3, \tag{31}$$

or

$$P_3 = \sum_{j=1}^{3} \varepsilon_{3j} E_j - \varepsilon_0 E_3. \tag{32}$$

Thus the perturbation $[\mathbf{P}_{pert}]_z$ is

$$[\mathbf{P}_{pert}]_z = \Delta P_3 = \sum_{j=1}^{3} \Delta\varepsilon_{3j} E_j. \tag{33}$$

Assuming E_z=0 and E_y is negligible (TM), equation (33) reduces to

$$\Delta P_3 = \Delta\varepsilon_{31} E_1. \tag{34}$$

Using the following identity [18]

$$\left[\frac{1}{n^2}\right]_{31} = \left[\frac{1}{n^2}\right]_5 = -\frac{\varepsilon_0 \varepsilon_{31}}{\varepsilon_{33}\varepsilon_{11}}, \tag{35}$$

gives

$$\Delta P_3 = \Delta\varepsilon_{31} E_1 = -\frac{\varepsilon_{33}\varepsilon_{11}}{\varepsilon_0} \Delta\left(\frac{1}{n^2}\right)_5 E_1. \tag{36}$$

Equation (36) relates a z directed medium polarization to an x directed optical electric field through the index change of n_5. Similarly, for a TE-polarized optical wave, the change of medium polarization component P_1 can be expressed as

$$\Delta P_1 = \Delta\varepsilon_{13} E_3 = -\frac{\varepsilon_{33}\varepsilon_{11}}{\varepsilon_0} \Delta\left(\frac{1}{n^2}\right)_5 E_3. \tag{37}$$

And the change of index n_5 can be realized via the electrooptic coefficient r_{51} by applying an electrical field in the x direction (E_x). Then from equation (20) and (21), the change of n_5 can be expressed as

$$\Delta\left(\frac{1}{n^2}\right)_5 = r_{51} E_x^e, \tag{38}$$

where $r_{51} \simeq 28\times10^{-12}\ {}^{m}\!/\!_{V}$ for $LiNbO_3$.

D-2. Polarization conversion

Polarization conversion between TE and TM mode can be described by the coupled mode equations

$$\begin{cases} \dfrac{dA}{dy} = i\kappa B e^{-i\Delta y} \\ \dfrac{dB}{dy} = i\kappa^{*} A e^{i\Delta y} \end{cases} \tag{39}$$

where A and B are the amplitudes of TE and TM mode; κ is the coupling coefficient; y is the direction of propagation. Δ is the phase mismatch constant, which was defined in equation (1) on page 5.

If κ in equation (39) is a constant along y direction, the solution to equation (39), subject to boundary conditions A(0)=1 and B(0)=0, can be given as [24]

$$\begin{cases} A(y) = e^{i\delta y}\{\cos[(\kappa^2+\delta^2)^{1/2} y] + i\dfrac{\delta}{(\kappa^2+\delta^2)^{1/2}}\sin[(\kappa^2+\delta^2)^{1/2} y]\} \\ B(y) = -ie^{-i\delta y}\dfrac{\kappa}{(\kappa^2+\delta^2)^{1/2}}\sin[(\kappa^2+\delta^2)^{1/2} y] \end{cases} \tag{40}$$

with $\delta \equiv \dfrac{\Delta}{2}$. A plot of the mode power variation with position along the propagation direction for the phase-matched (δ=0) and δ≠0 cases is illustrated in Fig. 9.

It is obvious from Fig. 9 that the conversion is most efficient when the phase match condition (δ=0) is fulfilled. A deliberate off-diagonal index change with period

$$\Lambda = \frac{2\pi}{\left|\beta_m^{TM} - \beta_m^{TE}\right|} = \frac{\lambda_0}{\left|n_{TM} - n_{TE}\right|} = \frac{\lambda_0}{\Delta n} \tag{41}$$

can be used to neutralize the phase mismatch if it is not naturally matched. The phase match condition causes the mode conversion to be wavelength selective and allow wavelength tuning by changing the birefringence Δn.

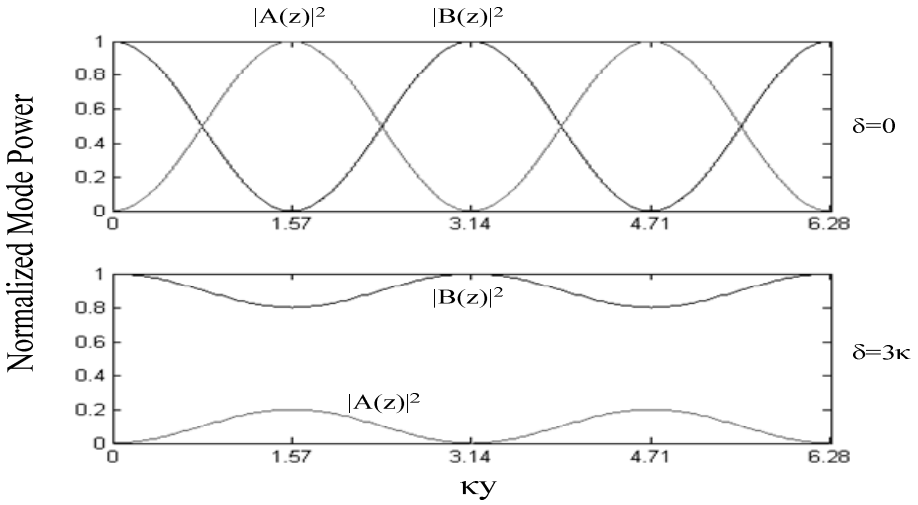

Fig. 9. Power exchange between TE and TM modes for phase-matched (δ=0) and -mismatched (δ=3κ) conditions.

To analyze the polarization conversion, we introduce a matrix description for the polarization coupling region. The matrix represents the transfer function between the output and input states of polarization. According to [24], an arbitrary state of polarization in the waveguide can be represented by a column vector

$$\mathbf{A}(y) = \begin{pmatrix} A_1(y) \\ A_2(y) \end{pmatrix} \tag{42}$$

where $A_1(y)$ and $A_2(y)$ denote TE and TM mode respectively. For example, linearly polarized TE light is described as $\begin{bmatrix} 1 \\ 0 \end{bmatrix}$, and as $\begin{bmatrix} 0 \\ 1 \end{bmatrix}$ for TM polarized light. The output polarization state $\mathbf{A}(L)$ over a polarization coupling region length of L can be related to the input $\mathbf{A}(0)$ via a 2×2 transfer matrix $\mathbf{M}^{\mathbf{C}}$ of a converter section as $\mathbf{A}(L)= \mathbf{M}^{\mathbf{C}}\cdot\mathbf{A}(0)$.

And the transfer matrix $\mathbf{M}^{\mathbf{C}}$ of a converter section is given as

$$\mathbf{M}^{\mathbf{C}} = \begin{pmatrix} a_c \exp[-i(\beta_1 + \delta)L] & b_c \exp[-i(\beta_1 + \delta)L] \\ -b_c^{*} \exp[-i(\beta_2 - \delta)L] & a_c^{*} \exp[-i(\beta_2 - \delta)L] \end{pmatrix} \tag{43}$$

Here, the asterisk denotes the complex conjugate and a_c and b_c are given as

$$\begin{cases} a_c = \cos[(\kappa^2 + \delta^2)^{1/2} L] + i \dfrac{\delta}{(\kappa^2 + \delta^2)^{1/2}} \sin[(\kappa^2 + \delta^2)^{1/2} L] \\ b_c = -i \dfrac{\kappa}{(\kappa^2 + \delta^2)^{1/2}} \sin[(\kappa^2 + \delta^2)^{1/2} L] \end{cases} . \tag{43-a}$$

The expression for δ can be derived from equation (1) and (41) as,

$$\delta = \frac{\beta_1 - \beta_2}{2} - \frac{\pi}{\Lambda} \simeq \Delta\lambda \left[\frac{d}{d\lambda} \frac{\beta_1(\lambda) - \beta_2(\lambda)}{2} \right]_{\lambda = \lambda_0} \simeq -\frac{\Delta\lambda}{\lambda_0} \frac{\pi}{\Lambda} \frac{\Delta n_{gr}(\lambda_0)}{\Delta n_{ph}(\lambda_0)} \tag{44}$$

where $\Delta\lambda = (\lambda - \lambda_0)$ is the detuning of wavelength from the phase-matched design wavelength λ_0, $\Delta n_{ph}(\lambda) = n_{TM}(\lambda) - n_{TE}(\lambda)$ denotes the wavelength dependent phase index difference for the two modes, and $\Delta n_{gr}(\lambda_0)$ is the group index difference at λ_0.

Assuming phase match condition is met ($\delta = 0$) and input is TE polarization $\begin{bmatrix} 1 \\ 0 \end{bmatrix}$, the output state can then be described from equation (43-a) as $\begin{bmatrix} \cos \kappa L \\ -i \sin \kappa L \end{bmatrix}$. Obviously, complete conversion from TE to TM polarization $\begin{bmatrix} 0 \\ 1 \end{bmatrix}$ would occur if $\kappa L = \dfrac{\pi}{2}$ (corresponding to the shortest possible choice of interaction length).

From equation (40), we define the power conversion efficiency (PCE) as

$$\mathrm{PCE} = \left|\mathrm{B(L)}\right|^2 = \left|\frac{\kappa}{(\kappa^2+\delta^2)^{1/2}}\sin[(\kappa^2+\delta^2)^{1/2}\mathrm{L}]\right|^2 \tag{45}$$

where L is length of the polarization conversion region. The calculated PCE as a function of detuning wavelength $\Delta\lambda$ with a total number of periods N=1440 at λ_0=1530nm center wavelength is plotted in Fig. 10.

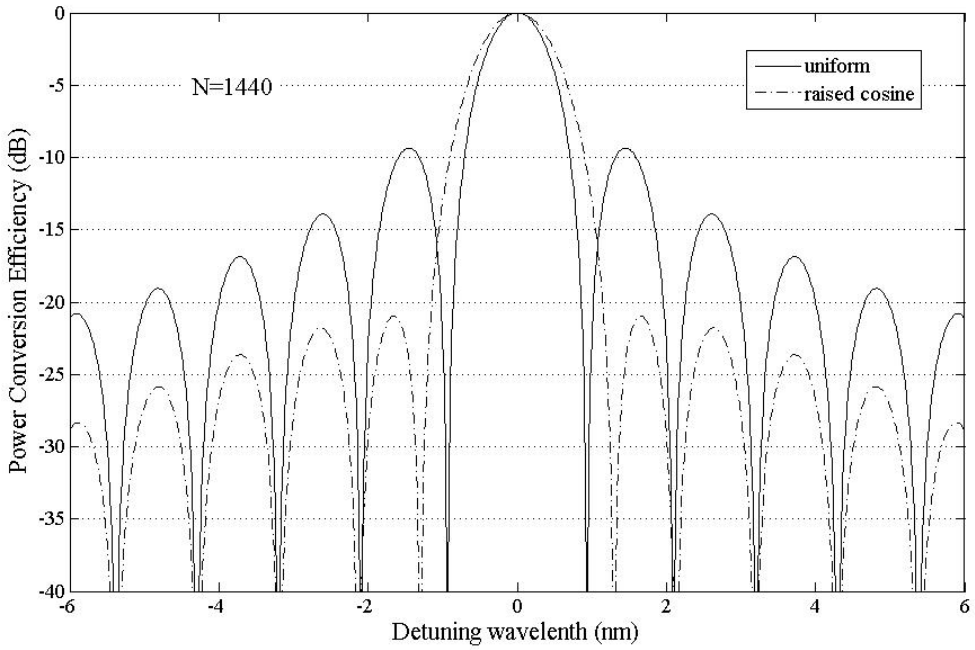

Fig. 10. Simulated PCE as a function of detuning wavelength, with N=1440 periods at 1530nm center wavelength.

The solid line is for a uniform coupling constant, while the dashed plot assumes a raised cosine apodization function

$$\kappa(y) = \kappa_0 + 0.5\kappa_0 \cos[2\pi(\frac{y}{L} - 0.5)], \tag{46}$$

which allows to reduce the side lobes approximately 20dB below peak transmission. As a

result of apodization, however, the 3dB bandwidth is broadened compared to the uniform coupling case.

A key parameter for PCE in equation (45) is the full width at half maximum (FWHM), i.e. the 3dB bandwidth, and is given by [24, 25]

$$\Delta\lambda_{3dB} \simeq \frac{2.509}{\pi}\frac{\Delta n_{ph}(\lambda_0)}{\Delta n_{gr}(\lambda_0)}\frac{\Lambda}{L}\lambda_0 . \tag{47}$$

For a uniform grating of N total periods, L=NΛ, the FWHM reduces to

$$\Delta\lambda_{3dB} \simeq \frac{2.509}{\pi}\frac{\Delta n_{ph}(\lambda_0)}{\Delta n_{gr}(\lambda_0)}\frac{\lambda_0}{N} . \tag{48}$$

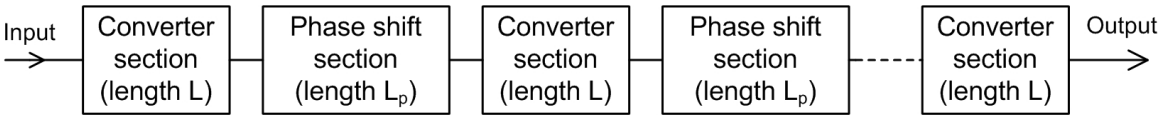

Fig. 11. Polarization converter sections in series.

To establish a matrix approach for the analysis of the device configuration proposed in this research, the situation of a series of converter sections separated by propagation regions may be considered, as shown in Fig. 11. The phase shift occurring at the propagation region between two adjacent coupling regions can be described by a transfer matrix $\mathbf{M^P}$ as

$$\mathbf{M^P} = \begin{pmatrix} e^{-j\frac{\phi}{2}} & 0 \\ 0 & e^{j\frac{\phi}{2}} \end{pmatrix} \tag{49}$$

where the experienced phase retardation is $\phi=(\beta_1-\beta_2)L_P$ with L_P the length of the

propagation region. Therefore, the transfer matrix of a single mode converter section followed by a propagation region is given by the matrix product $\mathbf{M^P \cdot M^C}$. For a device with of N mode converter sections separated by N-1 propagation sections, the overall transfer matrix can be expressed as

$$\mathbf{T}=\left(\prod_{j=2}^{N}\mathbf{M}_j^{\mathbf{C}}\mathbf{M}^{\mathbf{P}}\right)\mathbf{M}_1^{\mathbf{C}}\,. \tag{50}$$

A simulation program based on the above analysis for polarization converter device is generated in Matlab and can be found in Appendix 4.

CHAPTER III

DEVICE ANALYSIS

In this chapter, the structure of the tunable optical filter is presented and its special features are discussed. The operation principle of the device is also explained.

A. Previous design

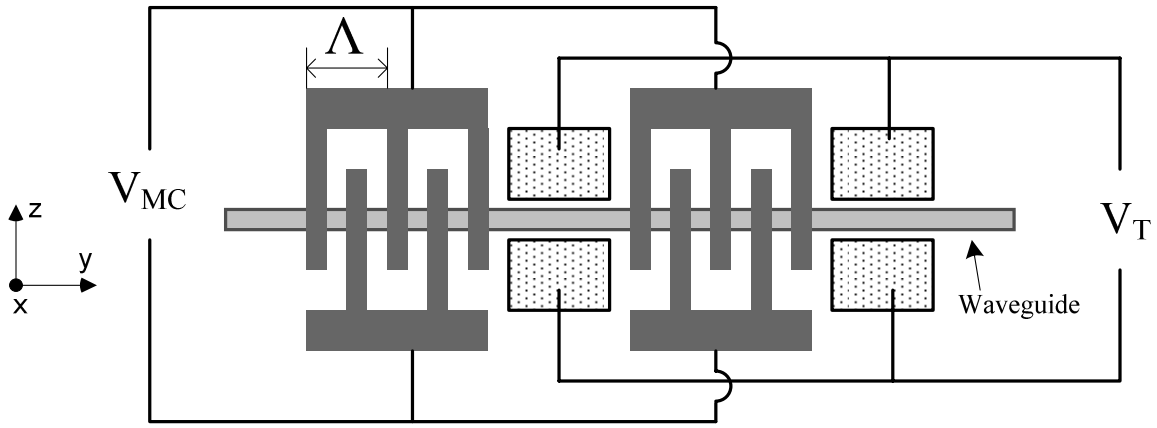

Fig. 12. Electrodes structure of previous EOTFs.

The first laboratory demonstrations of EOTFs that utilized electro-optically induced polarization coupling were reported in [9] and [26]. A schematic diagram of the structure for those devices is depicted in Fig. 12, where the electrode structure is composed of pairs of mode converter (solid part) and birefringence tuning electrodes (dots part). Voltage V_{MC} applied to the interdigital electrode gratings of period Λ produces TE↔TM mode conversion through the r_{51} coefficient via the x component of the electrical field. Periodic electrodes are used to achieve phase matching between the orthogonal modes

($\lambda_0=\Lambda\left|n_{TM}-n_{TE}\right|$). Voltage V_T applied on the tuning electrode sets changes the birefringence $\left|n_{TM}-n_{TE}\right|$ in the waveguide and hence changes the phase-matched wavelength λ_0. Polarization conversion in those devices can be described by the coupled mode equations (39) on page 20.

Here, the coupling coefficient κ can be related to the applied voltage V_{MC} as [24]

$$\kappa=\Gamma_{TE-TM}\frac{4\pi}{\lambda_0}\sqrt{n_{TE}^3 n_{TM}^3}\,r_{51}\frac{V_{MC}}{\Lambda}, \tag{51}$$

with Γ_{TE-TM} characterizing the normalized overlap parameter between the applied electrical field and the two (TE & TM) optical fields, $0<\Gamma_{TE-TM}<1$.

B. New polarization converter

A schematic diagram of the new programmable polarization converter is depicted in Fig. 13. The interdigital electrode patterns are grouped into different sets that are separated by an integer number of grating period. By applying voltages to the sets of interdigital electrodes individually, the vertical component of electrical fields (E_x) (see Fig. 13 (b)) causes TE↔TM coupling via the r_{51} electrooptic coefficient. The extent of interaction depends on the coupling coefficient κ, which is a function of the applied electrical field component E_x as described in equation (51). A uniform voltage applied on all electrode sets results in a spatially periodic κ of constant amplitude, and produces a

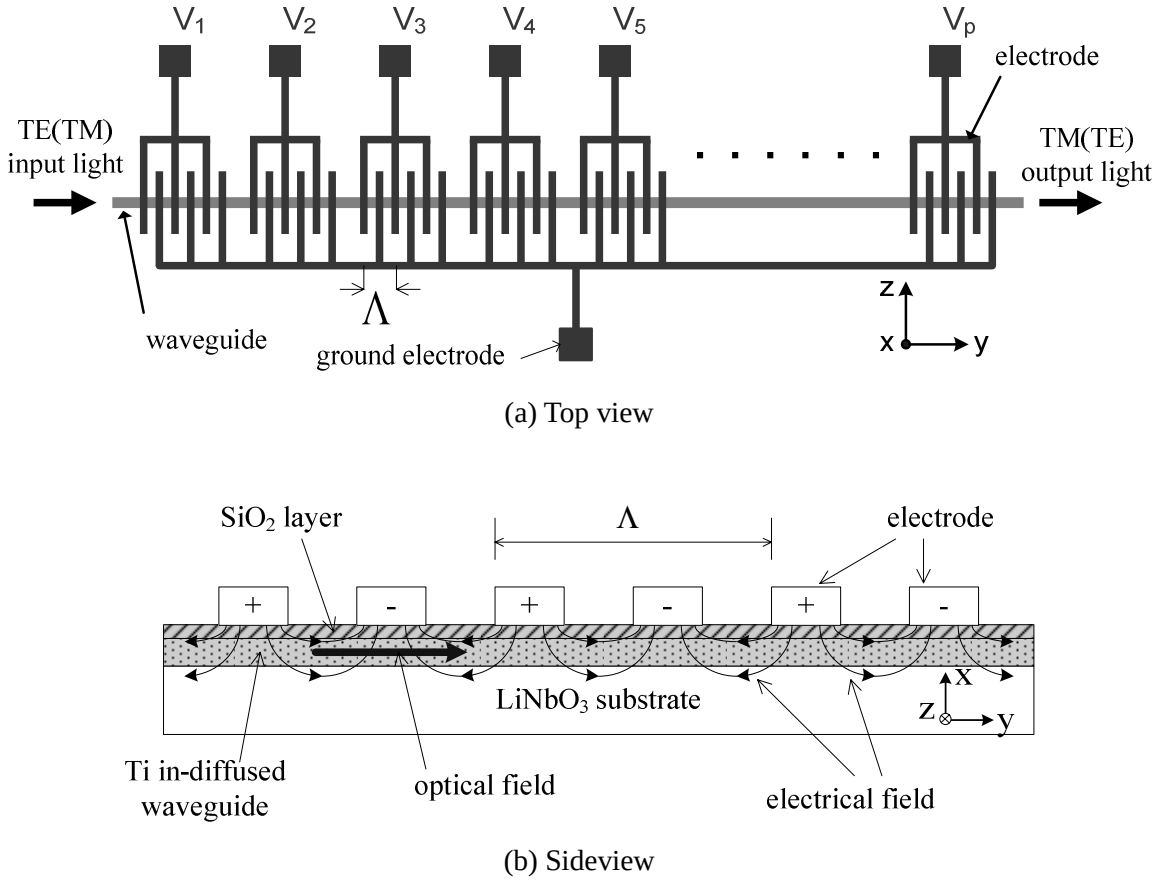

Fig. 13. New programmable polarization converter via independent electrode sets.

spectral response (channel 0, or center wavelength selection) with side lobes about ~9dB below the main peak [27]. The application of a weighting function to the coupling coefficient κ along the coupling length makes it possible to control the extent of interaction and can result in significant side lobe suppression, or apodization [26, 28, 29]. In previous EOTF devices [26], the apodization was achieved by tapering the number of interdigital finger pairs in the mode converter electrodes structure, and the same voltage was applied to the mode converter sections while a separate voltage control was used for wavelength tuning. In the proposed device configuration, the number of interdigital

fingers pairs in the individual converter electrode sets is the same, and each electrode set is controlled by an independent voltage, which makes it possible to taper the voltage distribution directly over the coupling length. For example, a raised cosine voltage distribution over the coupling length could reduce the nearest side lobes to about 20dB below main peak, while slightly increasing the filter bandwidth.

The device principle is based on the Fourier transfer relation that exists between the spatially varying coupling coefficient $\kappa(y)$ and the output spectrum [30, 31]. Therefore it is possible to obtain a desired spectral response corresponding to a certain frequency channel by independently adjusting the voltage applied on each group of electrode sets. For a device with a total number P electrode sets, selection of frequency channels is accomplished by programming the voltages $(V_j)_p$, p=1,…,P, applied on the electrode sets, where "j" is the channel number. The spacing between successive electrode sets is set to an integer number m of the interdigital grating period Λ to ensure in-phase coupling. The number of selectable channels in such an arrangement is related to the number of electrode sets by $N=\frac{P}{2}+1$ and produces two sidebands simultaneously relative to center frequency ν_0. The coupling coefficient κ is spatially dependent on the propagating length and can be ideally given as

$$\kappa_j(y) = S(y)\cos(\Delta_j y), \tag{52}$$

with S(y) an apodization function and $\Delta_j = \frac{2\pi\left|n_{TM} - n_{TE}\right|(\nu_j - \nu_0)}{c}$.

Channel 0, i.e. the center frequency of the tuning range for the device, represents the case of Δ=0 when the voltages on the electrode sets all have the same sign and when

maximum polarization conversion occurs, and is given by

$$\nu_0 = \frac{c}{\left|n_{TM} - n_{TE}\right|\Lambda}. \tag{53}$$

Channel ±1 is selected when $\Delta_1 L = 2\pi$, and channel ±2 is selected when $\Delta_2 L = 4\pi$, where L is the total length of the coupling region. Therefore, channel spacing can be calculated as

$$\Delta\nu = \frac{c}{L \cdot \Delta n}, \tag{54}$$

with $\Delta n = \left|n_{TM} - n_{TE}\right|$ the birefringence of the $LiNbO_3$ crystal.

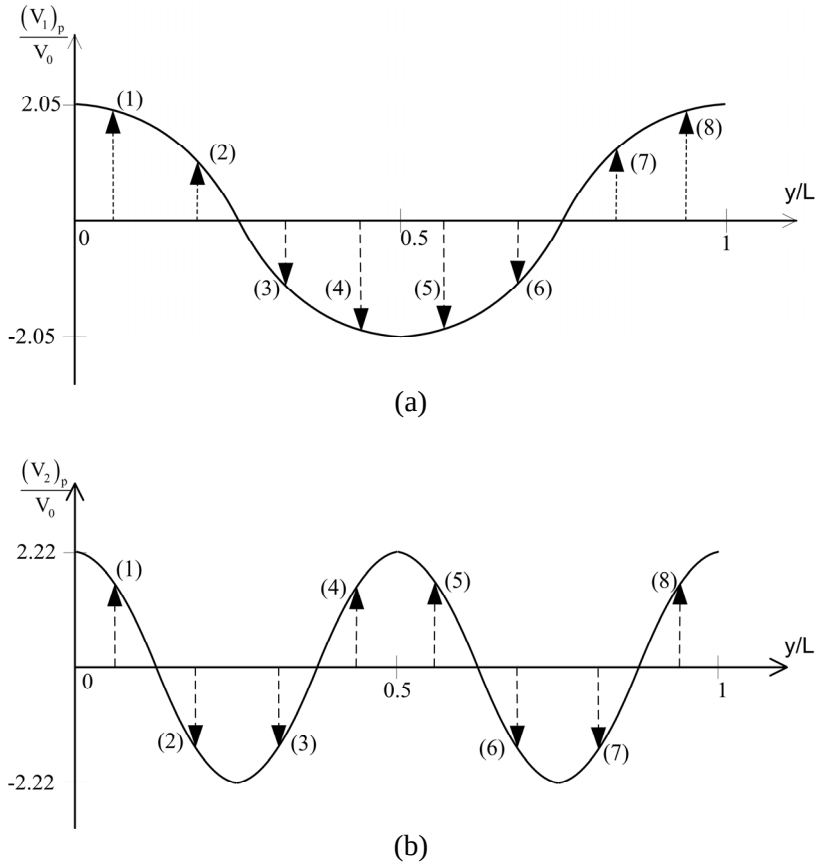

Fig. 14. Relative voltage values $(V_j)_p/V_0$ to select j^{th} channel for two sideband device (V_0 is the uniform voltage value to select channel 0): (a) channel ±1, and (b) channel ±2.

Table 2. Relative voltage values $(V_j)_p/V_0$ to select j^{th} channel for two sideband device (V_0 is the uniform voltage value to select channel 0), 8 electrode sets, uniform coupling.

Channel j	Electrode set p							
	1	2	3	4	5	6	7	8
0	1	1	1	1	1	1	1	1
±1	1.896	0.785	-0.785	-1.896	-1.896	-0.785	0.785	1.896
±2	1.571	-1.571	-1.571	1.571	1.571	-1.571	-1.571	1.571

In practice, κ(y) can not vary continuously as described by equation (52), but varies discretely and is constant within each of the electrode sets region. Fig. 14 illustrates the voltage determination algorithm for selecting ±1 channel (top, a) and ±2 channel (bottom, b) in the case of eight (P=8) electrode sets. The length of the dashed arrow indicates the voltage value that is needed on the corresponding electrode set, relative to the uniform voltage that is required for selecting the center frequency channel υ_0. A summary of the relative voltage value needed to select different frequency channels for a device with 8 electrode sets is given in Table 2.

Calculated values for the power conversion efficiency as a function of wavelength shift from center wavelength is obtained from the simulation program in Appendix 4 and plotted in Fig. 15 for a converter with (a) 8 electrode sets and (b) 16 electrode sets. As shown in the figures, excellent converter performance is predicted when apodization is employed to suppress the nearest side lobes by approximately 20dB below main peak.

From the simulation results, significant polarization conversion is not only obtained at the desired wavelength, but also at various other wavelengths away from the selected wavelength. These satellite peaks are a consequence of the coarse period in the electrode structure, introduced by the periodic arrangement of the mode converter sections [24].

Increasing the number of electrode sets will move the spectral location of these satellite peaks further away from the center wavelength, as indicated by comparing Fig. 15 (a) (8 electrode sets case) and Fig. 15 (b) (16 electrode sets case).

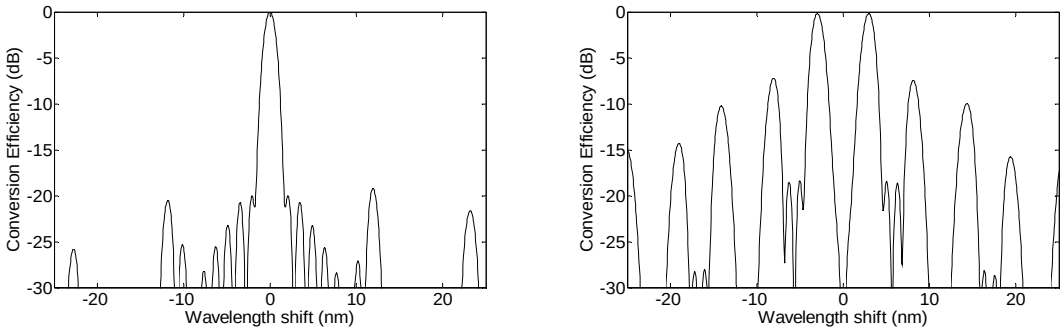

(a) 8 electrode sets: channel 0 selected (left plot) and channel ±2 selected (right plot)

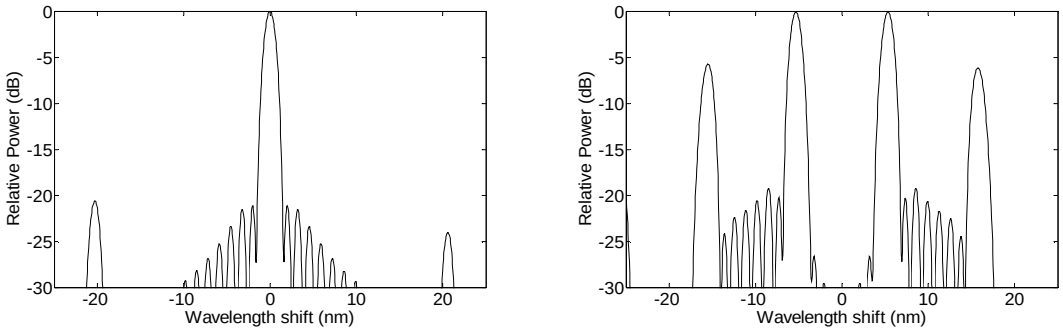

(b) 16 electrode sets: channel 0 selected (left plot) and channel ±4 selected (right plot)

Fig. 15. Calculated power conversion efficiency spectra for the polarization converter (two sideband device).

The approach characterized by equation (52) and output spectra illustrated in Fig. 15, i.e. with the spacing between electrode sets an integer number m of the grating period Λ, represents the case that the coupling coefficient κ is a real number. As a result, two sidebands equally separated from the center frequency ν_0 are selected simultaneously. Another electrode design configuration is proposed to select only one single sideband. In

such a design, the even numbered (2, 4, 6, 8…) electrode sets are left shifted by $\frac{\Lambda}{4}$ along the coupling length, which give rise to in-phase and quadrature coupling and results in a complex coupling coefficient κ given by

$$\kappa_j(y) = S(y)e^{i\Delta_j y} \tag{55}$$

with

$$\int_0^L \kappa_j(y)e^{-i\Delta_k y}dy = \frac{\pi}{2}\delta_{jk}, \tag{56}$$

where $\delta_{jk}=1$ if $j=k$ and $\delta_{jk}=0$ if $j\neq k$. In this case, instead of taking all the cosine values as the basis of voltages applied to the 8 electrode sets (as in Fig. 14), sine values are now used for the even numbered (2, 4, 6, 8) electrode sets as illustrated in Fig. 16.

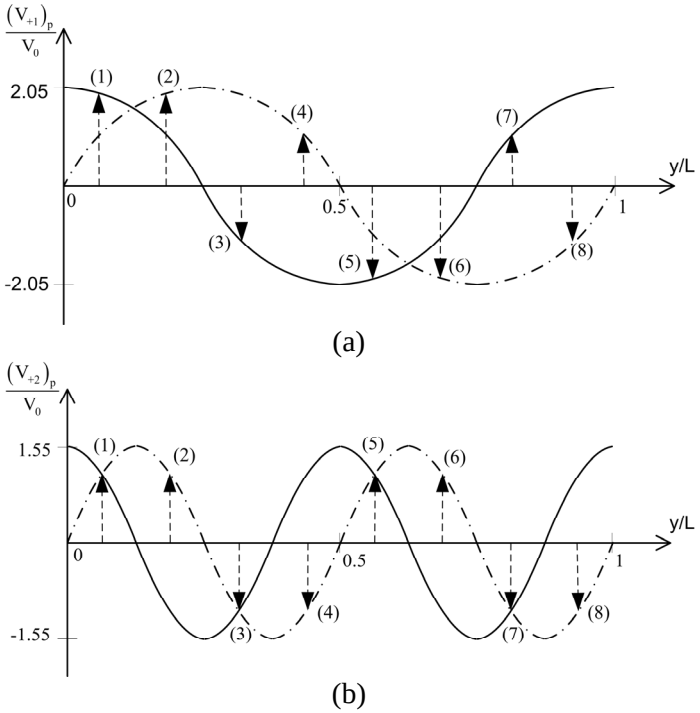

Fig. 16. Relative voltage values $(V_j)_p/V_0$ to select j^{th} channel for single sideband device (V_0 is the uniform voltage value to select channel 0): (a) channel +1, and (b) channel +2.

Table 3. Relative voltage values $(V_j)_p/V_0$ to select j^{th} channel for single sideband device (V_0 is the uniform voltage value to select channel 0), 8 electrode sets, uniform coupling.

Channel	Electrode set p							
j	1	2	3	4	5	6	7	8
-2	1.096	-1.096	-1.096	1.096	1.096	-1.096	-1.096	1.096
-1	1.896	-1.896	-0.785	-0.785	-1.896	1.896	0.785	0.785
0	2	0	2	0	2	0	2	0
+1	1.896	1.896	-0.785	0.785	-1.896	-1.896	0.785	-0.785
+2	1.096	1.096	-1.096	-1.096	1.096	1.096	-1.096	-1.096

The selection of center frequency ν_0 is obtained by applying a uniform voltage on every other electrode set to make $\Delta=0$. Table 3 summarizes the ratio of voltage values needed to select different frequency channels for the single-sideband device, relative to the uniform voltage value required for selection of the center frequency channel υ_0. Theoretical plots for single sideband polarization converter with apodization are also presented in Fig. 17.

Detailed discussion about channel selection for the EMF devices is given in Appendix 1.

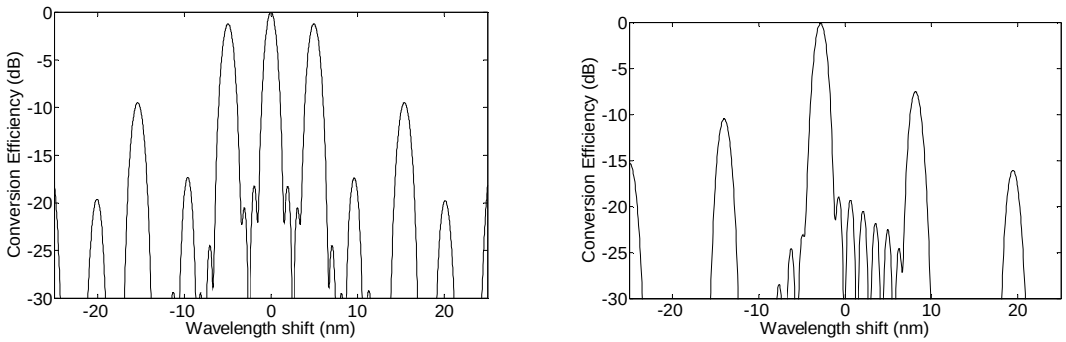

(a) 8 electrode sets: channel 0 selected (left plot) and channel -2 selected (right plot)

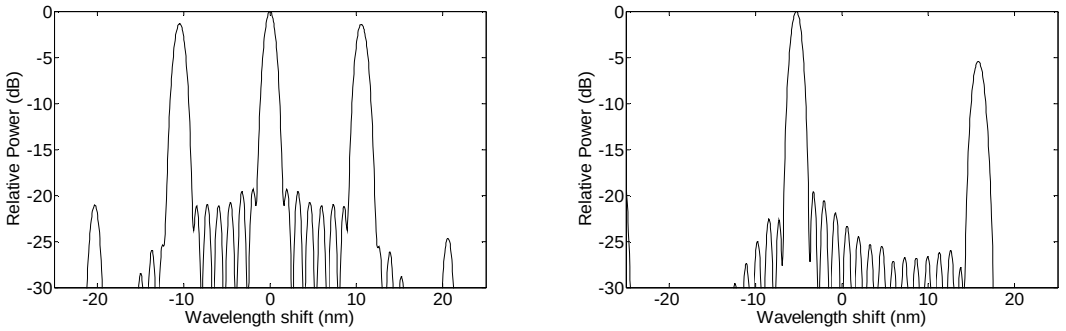

(b) 16 electrode sets: channel 0 selected (left plot) and channel -4 selected (right plot)

Fig. 17. Calculated power conversion efficiency spectra for the polarization converter with apodized coupling (single sideband device).

C. Two-port bandpass electro-optic matched filter (EMF)

A two-port bandpass electro-optic matched filter (EMF) is proposed as an extended application for the new programmable polarization converter and its diagram is depicted in Fig. 18. The configuration is similar to previous devices [15] shown in Fig. 4, and has the following features: (1) the Mach-Zehnder waveguide interferometer is asymmetric with an optical path difference for the waveguides between the beam splitters of a half-wavelength (π phase difference); (2) the relative positions of the polarization coupling regions in the two waveguide arms are displaced by half the spatial period of the

perturbation responsible for the coupling; (3) a group of electrode sets replaces the grating pads in Fig. 4 for the polarization coupling region and no separate electrode set is needed for wavelength tuning. The new device functions in a similar way as the previous device in [15]: a broadband optical signal (λ_1, $\lambda_{2,}$…λ_n) enters the input port, the intensity of the guided light splits into two equal parts at the first Y-branch which are directed toward the upper and lower mode converter regions. Then, the mode fields recombine interferometrically at the second Y-branch. Only fields at the selected converted wavelength λ_j appear in phase and thus are able to combine and emerge from the output port of the single mode channel waveguide, while all other λs radiate into the substrate. Detailed discussion of the waveguide interferometer with unequal arms can be found in Appendix 3 [32].

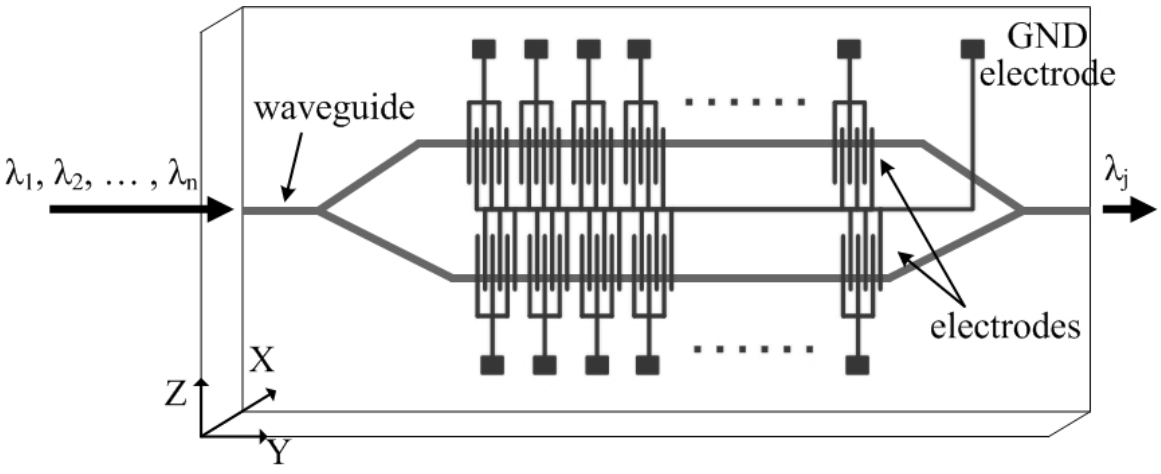

Fig. 18. EMF bandpass channel selection filter.

This project is directed towards the functionality demonstration of EMFs for

channel selection. In summary, the characteristics of EMFs include:

- Wide tuning range. The number of selectable channels N is equal to $\frac{P}{2}+1$. For a given total polarization coupling region length L, the tuning range can be increased by simply increasing the number of electrode sets P, with a corresponding decrease in the number of electrodes per set.
- Ability to select single or multiple channels. The coupling coefficient κ is proportional to the applied voltage on each electrode set. Thus, multiple channels can be chosen simultaneously by applying voltages which are the sum of required voltages for single channel selection.
- Other features similar to previous EOTF designs [14, 15], include rapid tuning speed, polarization independence, low fiber-to-fiber insertion loss.

D. Device fabrication process

The EMF device is realized in x-cut, y-propagating $LiNbO_3$ substrate (Crystal Technology Inc.). Channel waveguides are defined by in-diffusion of 7μm-wide and 1100Å-thick Ti strips for 11 hours at 1025^{o}C in wet air ambient. Both end faces of the crystal were polished after diffusion to provide endfire coupling into and out of the waveguides. Interdigital electrode sets are delineated on the surface of $LiNbO_3$ with 2000Å thick Aluminum (Al) film. An RF sputtered SiO_2 buffer layer of thickness 2000Å is deposited on the crystal prior to the metal electrodes to prevent strong attenuation of the TM-polarized light by the metal electrodes on the surface.

The quality of the SiO_2 insulating layer between the metal electrodes and the

$LiNbO_3$ substrate is critical for the EMF device, since high voltages (up to ±30V) are applied across 5.25μm wide electrode gap. Impurities and charges within the oxide layer can interfere with the electrical field near the waveguide region when voltage is applied. Such charges yield perturbation in the desired electrical field and affect the electro-optic effect and cause deterioration of the device performance.

Low temperature PECVD deposited SiO_2 was successfully used in previous devices [9, 26], but our lab lacks such equipment. RF sputtered SiO_2 [33-35] film is used in our device as a good alternative. Efforts have been made to optimize the parameters in RF sputter process for achieving minimum impurities and charges within the oxide layer. Detailed information on RF sputter process is given in Appendix15. To improve the SiO_2 film quality, the sample is annealed in wet O_2 ambient for 25 mins @ 900^oC after SiO_2 deposition.

The basic configuration of EMF devices (programmable polarization converter and bandpass filter) is illustrated in Fig. 13 and Fig. 18. Since the electrode pads are small (~1×1mm) and each electrode set requires different voltage control, normal electrical wires can not be used for connection to the electrode pads. Miniature-electrode probes are commonly used for small electrode pads, but are not appropriate for this device due to the large number of probes needed (8, 16 or even more). Instead, wire bonding was used to link the small electrode pads through a side patch with large electrode pads that can connect to the voltage supplies. Fig. 19 illustrates how the wire connections are accomplished. Small electrode pads on the $LiNbO_3$ sample are connected to the small pads on the side patch using K&S 4523D Digital Manual Wire Bonder (Kulicke & Soffa Inc.). 1 mil Al wire is bonded at room temperature as shown in Fig. 19. Each small pad

on the side patch is readily connected to a big pad after electrodes patterning, and electrical wires from the voltage supply are bonded on the big pads with conductive electrical epoxy (EE129-4, Epoxy Technology, Inc.). The electrical epoxy is cured at room temperature for 48 hours and can be removed by soaking in methanol for 1~2 hours.

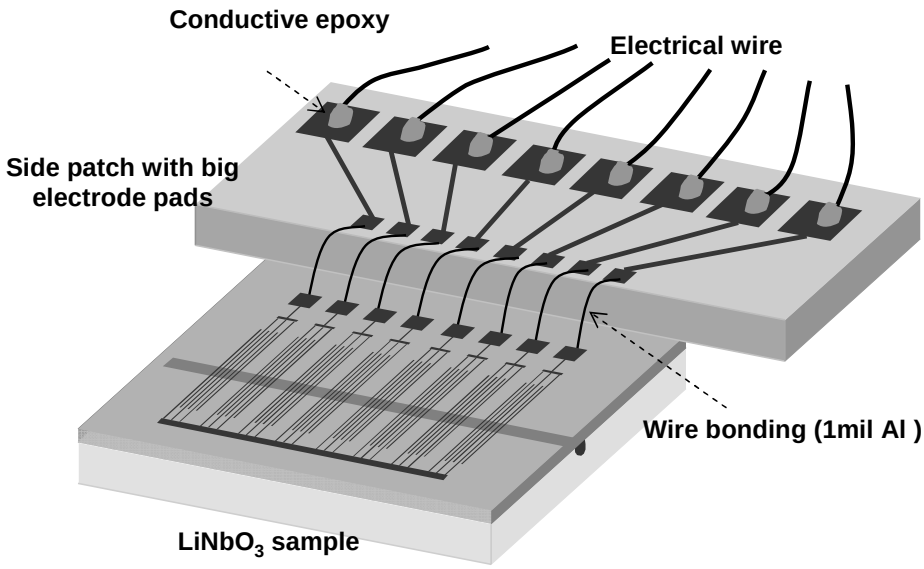

Fig. 19. Wire connection for an EMF polarization converter.

CHAPTER IV

OPTICAL TESTING AND RESULTS ANALYSIS

In this chapter, the optical testing and measurement results of straight channel waveguides, Mach-Zehnder interferometers, polarization converters and two-port bandpass filters are presented and discussed.

A. Channel waveguide

Good quality channel waveguides are the basis for the entire electro-optically tunable filter device. A good quality waveguide means low insertion loss for both TE and TM polarized light, where insertion loss is the total amount of optical intensity lost through a device and is defined as

$$\text{Insertion loss (dB)} = \text{-}10 \cdot \log \frac{P_{out}}{P_{in}}. \tag{57}$$

Waveguide insertion loss is a combination of propagation loss, Fresnel loss and mode mismatch loss. Fresnel loss, also called Fresnel reflection loss, is due to the reflection at the two end interfaces of the substrate. It can be expressed as follow

$$\text{Fresnel loss(dB)} = -2 \cdot 10 \cdot \log \left[1 - \left(\frac{n-1}{n+1} \right)^2 \right]. \tag{58}$$

The schematic diagram of the optical testing setup for the insertion loss measurement is shown in Fig. 20. A pigtailed 1.55μm DFB laser diode driven by current source (ILX Lightwave, Model LDX-3412) at 32mA was used as the optical power source. The laser diode was spliced to a single mode fiber (Corning SMF-28^{TM}) and then

passed through a fiber polarization controller (Thorlabs Inc., Model FDC 10), which was used to control the polarization state of the light launched into the device. The emerging light at the output of the device was butt coupled to another single mode fiber. The output light was directed through the fiber to a Ge photodetector (Newport, Model 818-IR), which is connected to a power meter (Newport, Model 1825-c).

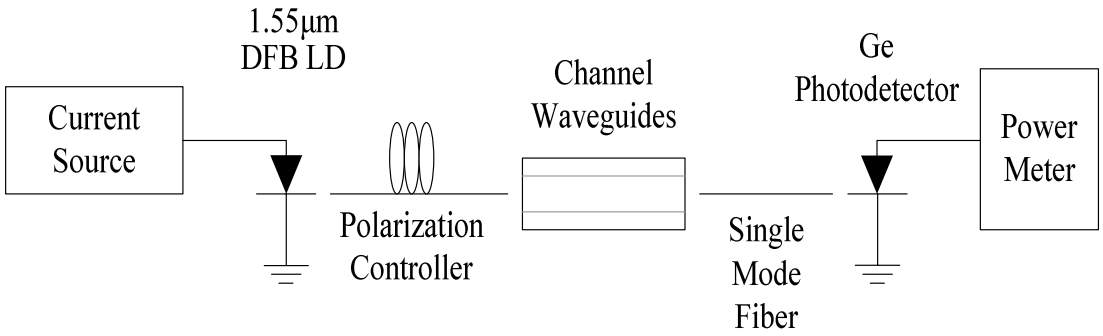

Fig. 20. Testing setup for insertion loss measurement.

B. Mach-Zehnder interferometer waveguide

The Mach-Zehnder interferometers are key elements for the electro-optically tunable filter. Two different Mach-Zehnder interferometer configurations were produced on the same sample: symmetric Mach-Zehnder interferometer configuration with equal waveguide arms; and asymmetric Mach-Zehnder interferometer configuration with a half-wavelength optical path difference between the two waveguide arms. Their schematic configurations are shown in Fig. 21 and the detailed dimensions are given in Appendix 18. The full splitting angle is decreased from 1.2º [15, 36] to 1º to minimize the bending loss at the Y-branch. Waveguide samples which carry both symmetric and asymmetric Mach-Zehnder interferometer waveguides were optimized towards the

following two goals:

- symmetric Mach-Zehnder interferometer should exhibit maximum output power, i.e. minimum insertion loss;
- asymmetric Mach-Zehnder interferometer should exhibit minimum output power due to destructive interference (theoretically zero output).

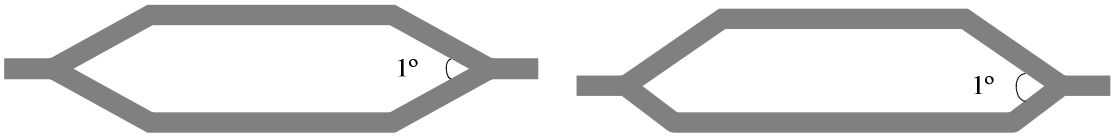

(a) symmetric, equal arms; (b) asymmetric, unequal arms.

Fig. 21. Two different Mach-Zehnder interferometer configurations.

7μm wide straight channel waveguide (SC), symmetric interferometer (SI) and asymmetric interferometer (FI) are fabricated and characterized on sample P46. The Ti film thickness is 1116Å and the sample was diffused in wet ambient at 1035ºC for 9+1 hours. A summary of the insertion loss variation with diffusion time is presented in Table 4.

Table 4. Insertion loss variation with diffusion time for straight channel waveguides (SC), symmetric interferometers (SI) and asymmetric interferometers (FI) for sample P46, Ti thickness=1116Å, diffused at 1035ºC for 9+1 hours.

Diffusion time	FI#2		SC#2		SI	
	TE input	TM input	TE input	TM input	TE input	TM input
9 hours	17.63 dB	29.37 dB	2.72 dB	2.85 dB	3.92 dB	5.70 dB
9+1 hours	23.83 dB	31.05 dB	2.97 dB	3.32 dB	4.31 dB	5.20 dB

C. TE↔TM polarization converter

To evaluate TE↔TM polarization converters, optical testing was carried out using a broadband light source. The setup is shown schematically in Fig. 22.

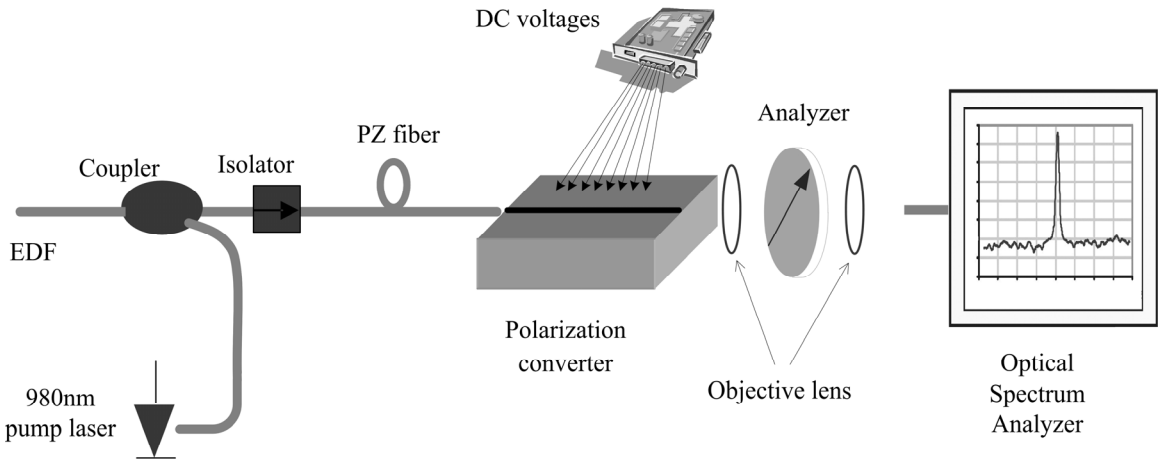

Fig. 22. Optical testing setup for polarization mode converter.

A 10m long erbium-doped fiber (EDF) was pumped by a 980nm laser diode (Lasertron, MA, Model QLM9S473-217) through a WDM coupler and Amplified Spontaneous Emission (ASE) light from the Erbium-Doped Fiber Amplifier (EDFA) was used as the broadband light source (Fig. 23 shows the ASE output spectrum driven at 70mA). An optical isolator was included at the output of the coupler to prevent external cavity self-oscillation. The light was then guided though a polarizing fiber (PZ fiber, 3M Corp.), whose end can be rotated to select either TE or TM polarization input to the device. The output light from the device was collimated by an objective lens (20X) and passed through a polarization analyzer, which can be set to either TE or TM mode by rotation. Afterwards, the light beam was focused by another objective lens (20X) and was

coupled into a single mode fiber. The output light spectrum from the fiber was monitored on an Optical Spectrum Analyzer (OSA, Anristru, Model MS9710C).

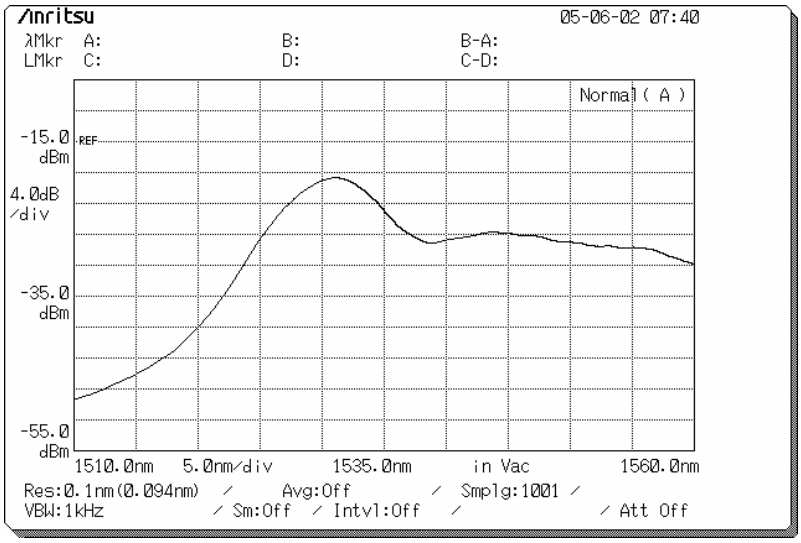

Fig. 23. Spectral density as a function of wavelength for the ASE output driven at pump current of 70mA.

For TE↔TM conversion measurement, the input PZ fiber was set to either TE or TM polarization and the output power for TE and TM mode was measured by rotating the analyzer to choose either TE or TM. TE→TM or TM→TE mode conversion efficiency can be determined by

$$\begin{aligned} \text{TE input}: \ \eta &= \frac{P_{TM}}{P_{TM}+P_{TE}} \\ \text{TM input}: \ \eta &= \frac{P_{TE}}{P_{TE}+P_{TM}} \end{aligned} \tag{59}$$

where P_{TE} and P_{TM} are the output power of TE and TM mode components, respectively.

Sample P33 with electrode configuration (Fig. 13) for single-sideband TE↔TM

mode conversion was fabricated on x-cut y-propogating $LiNbO_3$ substrate. 7μm wide single mode channel waveguides were produced by diffusing 1150Å thick Ti film at 1035ºC in wet ambient for 12 hours. 1800Å thick RF sputtered SiO_2 film was deposited on the crystal surface as an insulation layer between the electrodes and the waveguide. The deposited film was annealed at 900ºC for 25 mins. Interdigital electrode sets with spatial period Λ=21μm were delineated on the surface of $LiNbO_3$ with 2000Å thick Al film. A total of 16 independent electrode sets were used with each set containing 64 periods Λ. The separation between adjacent electrode sets alternates between $\left(72 \pm \frac{1}{4}\right)\Lambda$. Channel selection is achieved by independently changing the voltages on each electrode set. A single chip with 40 digital-to-analog converter (DAC) outputs from Analog Devices Inc. (part #: AD5379), followed by 16 Op-Amp (OPA445AP, Texas Instruments Inc.) arrays, was used to provide separate voltages to the electrode sets with a range of ±38V. Programmability was accomplished via a personal computer which controls the outputs of the 40-channel DAC. Optical testing was carried out after cooling the substrate to 17ºC through a thermoelectric cooler to shift the center frequency near the peak of the erbium doped fiber output spectra.

The transmission spectrum of the center frequency υ_0 for a mode converter on sample P33 with TM polarization input is shown in Fig. 24, which were obtained with a uniform voltage of 24 V applied on every other electrode set. Both the converted (TE) and unconverted (TM) portion are shown. Clearly, the mode conversion is highly wavelength dependent and the maximum conversion occurs at 1530.48nm, indicating a birefringence $\Delta n_{ph}(\lambda_0)$ of 0.0729 for Λ=21μm from equation (41). The 3dB bandwidth

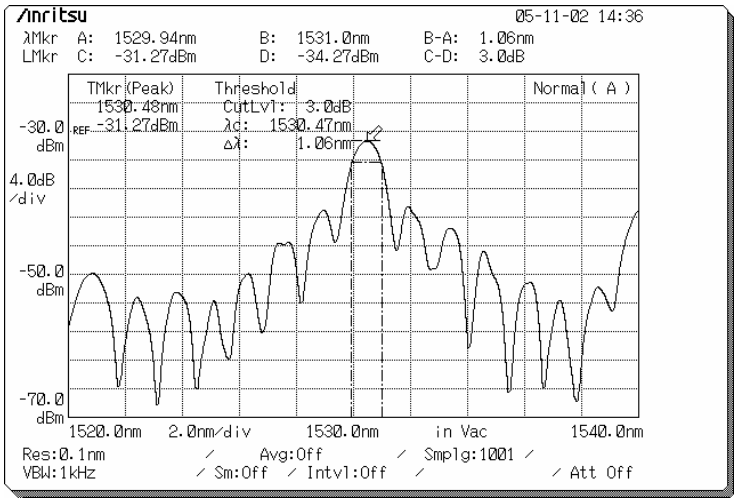

(a) converted (TE) output spectrum

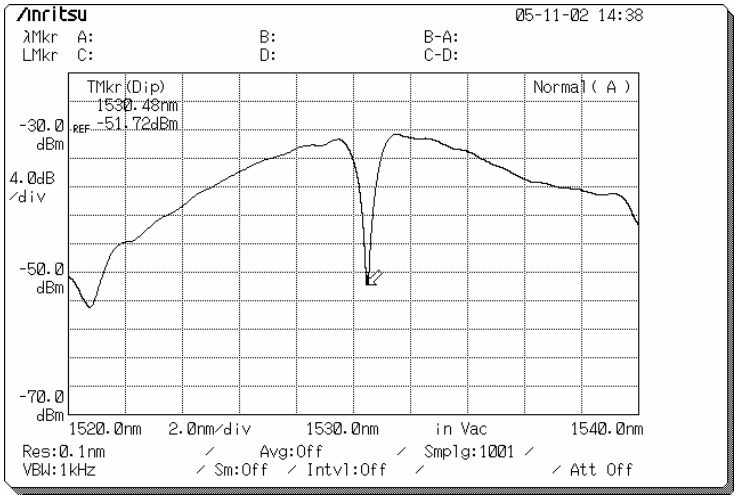

(b) unconverted (TM) output spectrum

Fig. 24. Channel 0 output spectrum of mode converter (sample P33) with TM input polarization.

is 1.06nm as indicated in Fig. 24 (a) and is in close agreement with equation (48). The nearest side lobes are about 9.7dB below the main peak and agree closely with the 9.5dB value anticipated for uniform coupling. As predicted from simulation results, satellite peaks appear at about ±10 nm away from the center wavelength, which is a result of the coarse period in the electrode structure. Similar testing results have been achieved for TE

polarization input on the same converter and its spectral response is compared to that of TM polarization input in Fig. 25. Both curves match each other closely and indicate polarization independence of the converter. In Fig. 25 and all following output spectral plots for polarization converter, relative power represents the output of the converter normalized to the spectral output from a channel waveguide on the same sample but without electrode sets and obtained for the same level of optical input power.

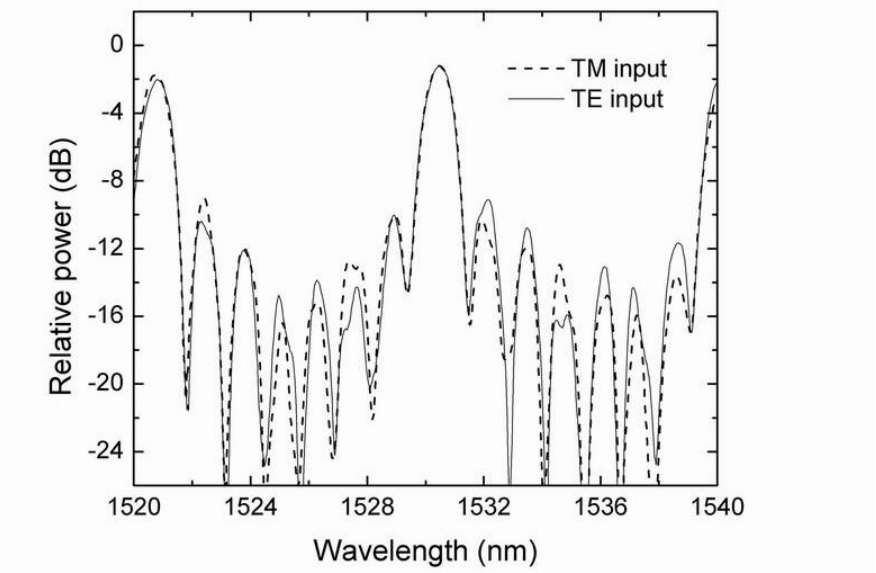

Fig. 25. Output spectra for the center frequency of the tuning range obtained with uniform coupling (voltage) for sample P33.

The polarization conversion efficiency was evaluated independently by coupling TM or TE polarized light at the input port and was calculated using equation (59). The spectral response of TE↔TM conversion efficiency for uniform coupling is shown in Fig. 26. The maximum conversion efficiencies are 99.1% for TM→TE and 99.6% for TE→TM, both observed at 1530.48nm.

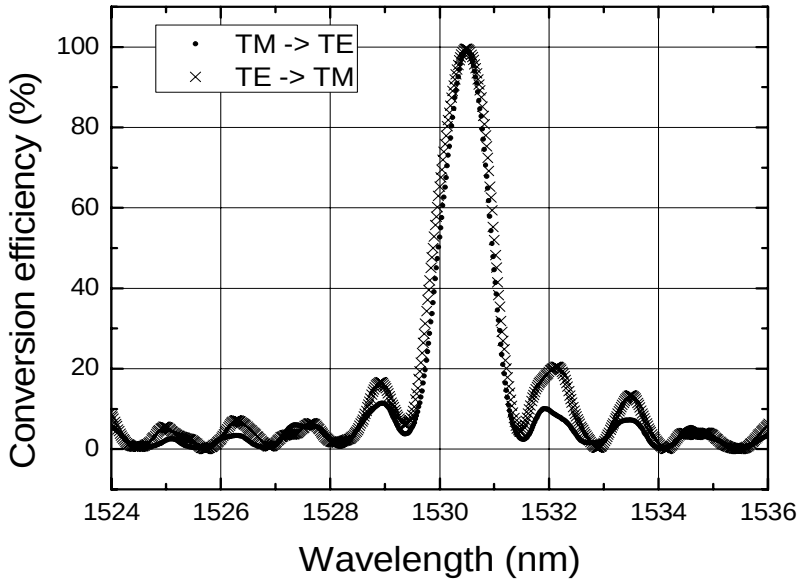

Fig. 26. The polarization conversion efficiency as a function of wavelength for TM and TE input, sample P33, channel 0.

The results shown in Fig. 25 were achieved by applying uniform voltages on the electrode sets. An apodization function can be used to taper the voltage distribution over the coupling length to reduce to side lobes. Fig. 27 shows that by applying a raised cosine shaped voltage distribution, nearest side lobes are notably reduced by about 17 dB below the main transmission peak, compared to a calculated 20 dB value, for both input polarization (TM input and TE input). The 3dB bandwidth is increased to 1.22nm due to apodization. The appearance of adjacent side lobes at ~-13 dB is not predicted in the theoretical analysis and is most likely caused by surface charges or moving charges in the SiO_2 layer that prevents the realization of the desired electric field distribution for apodization.

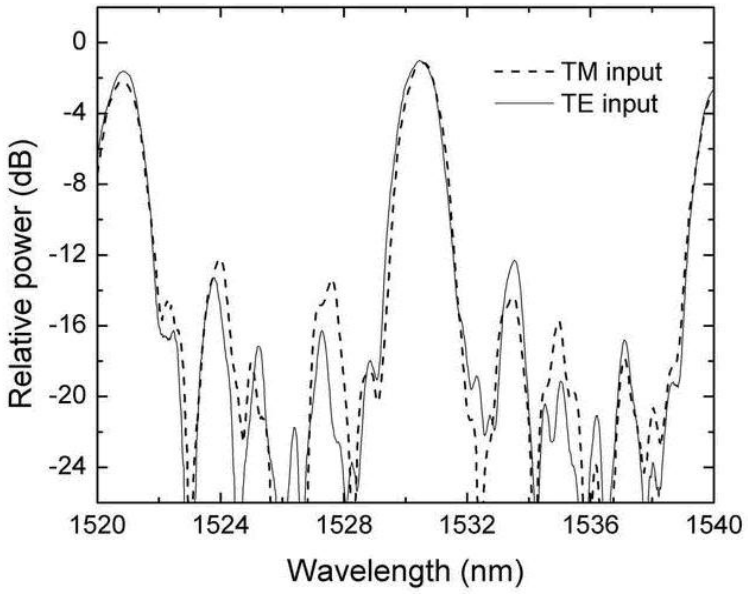

Fig. 27. Output spectra for the center frequency of the tuning range obtained with apodized coupling (voltage) for sample P33.

Fig. 28 shows the apodized single sideband optical output spectra for both TE and TM input cases when the voltages were adjusted for various channels selection by applying spatially periodic weighted independent voltage amplitude on each electrode set. The apodization function used in both cases was a raised cosine function, and the tuning ranges from 1525.6 to 1535.2 nm in each case. The missing output spectra for channels +3 and -3 in Fig. 28, is due to a rather large broadening of the main peak spectrum which occurred in apodization and ultimately merged with the nearest side lobes.

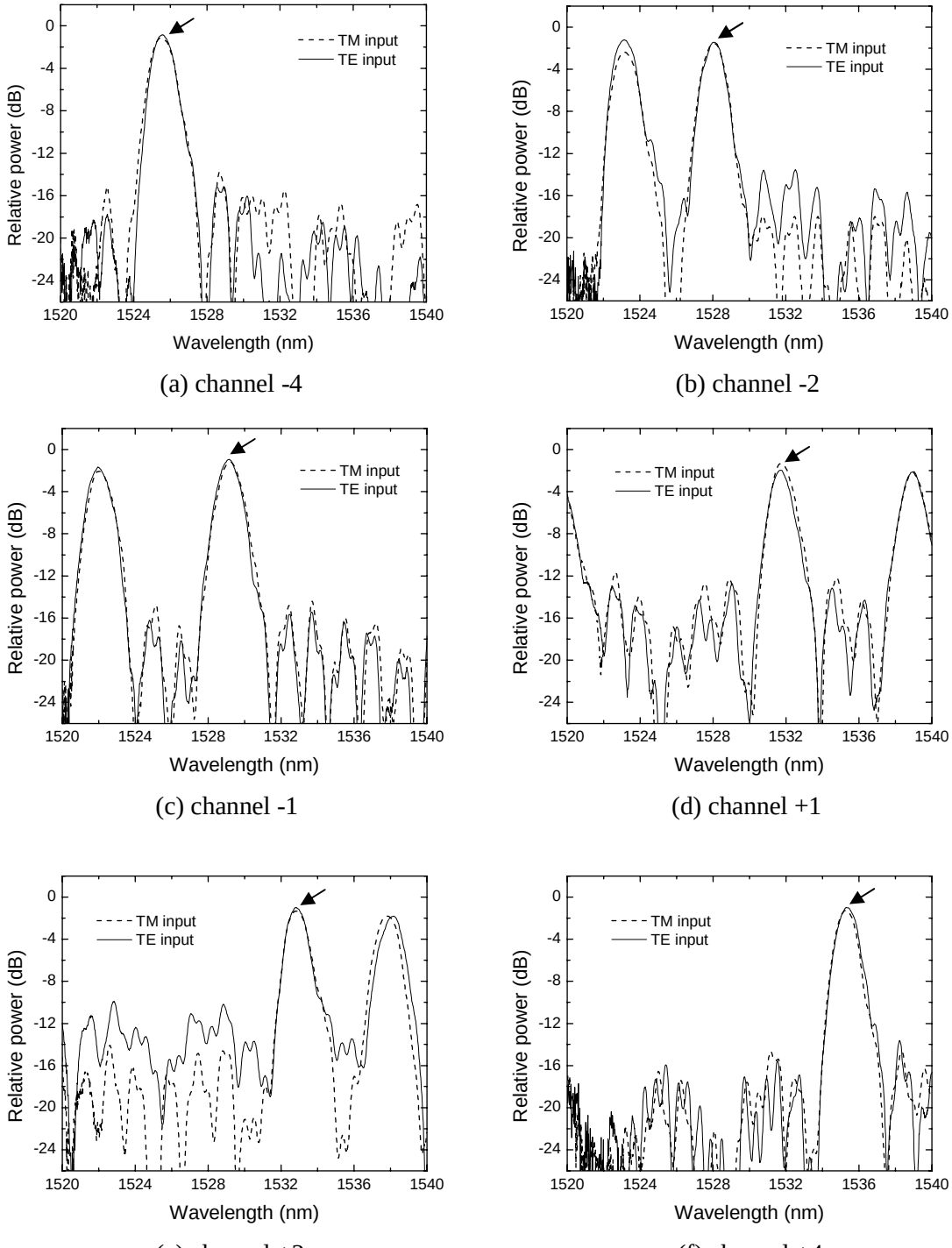

(a) channel -4 (b) channel -2

(c) channel -1 (d) channel +1

(e) channel +2 (f) channel +4

Fig. 28. Transmission characteristics of the selected channels obtained by applying independently weighted apodized voltages to the interdigital electrode sets. The arrows indicate the selected channels.

D. Two-port electrooptically tunable bandpass filter

Based on the obtained results for Mach-Zehnder interferometer waveguides and polarization converter, a complete bandpass filter sample (P46) containing filters of the configuration illustrated in Fig. 18 was produced following the fabrication procedure described in Chap. III. Asymmetric Mach-Zehnder interferometers were fabricated on x-cut, y-propagating $LiNbO_3$ by in-diffusion of 7μm wide 1116Å thick Ti stripes for 9+1 hours at 1035°C in wet air ambient. The end facets of the sample were then polished. The final length of the sample after polishing was 4.6 cm and the interferometer waveguides were tested and characterized as described earlier in section B. Then 1700Å thick SiO_2 film was deposited on the sample surface by RF sputtering as an insulation layer between the electrodes and the waveguide. The deposited film was annealed at 900ºC for 25 min in wet ambient. Interdigital electrode sets with spatial period Λ=21μm were delineated by positive photolithography on the surface of $LiNbO_3$ with 1800Å thick Al film by E-Beam evaporation. 16 independent electrode sets were used for each interferometer waveguide arm, and each set contained 64 periods Λ. The separation between adjacent electrode sets alternates between $\left(72 \pm \frac{1}{4}\right)\Lambda$. Details of the electrodes structure are shown in Appendix 19. The total length of the coupling region is about 2.4 cm. The relative positions of the polarization coupling region in the two interferometer waveguide arms are displaced in the propagation direction by half of the spatial period Λ. Optical testing was carried out for the bandpass filter with a setup similar to that of the polarization mode converter testing setup in Fig. 22, except that the light from the output of the filter is coupled into a single mode fiber directly which is then connected to the optical spectrum analyzer.

D-1. Spectral response of the bandpass filter at center frequency

The output spectrum of channel 0 of a bandpass filter device FI#2 on sample P46 with TM and TE polarization input is shown in Fig. 29 (a) and (b), which were obtained with a uniform voltage of 21 V applied on every other electrodes set. To demonstrate polarization independence, the output spectrum with input light polarized at 45º between TM and TE is also shown in Fig. 29 (c). At room temperature, the center wavelength is observed at 1523 nm. This is shorter than the expected wavelength, and could be due to the high temperature (900ºC) annealing procedure after RF SiO_2 deposition which changes the birefringence $\Delta n(\lambda_0)$ in the $LiNbO_3$ waveguide. The plots in Fig. 29 and all following spectral output plots were obtained by cooling the sample substrate to 18ºC through a thermoelectric cooler to shift the center wavelength of the tuning range closer to the EDFA transmission peak at 1530 nm.

As shown in Fig. 29, peak transmission for channel 0 is observed at 1528.88 nm for all three polarization input (TM, TE and 45º between TM and TE) indicating birefringence $\Delta n_{ph}(\lambda_0) \simeq 0.0728$ at 18ºC. The 3dB bandwidth is about 1.1 nm and is in good agreement with the expected value of 1.08 nm from equation (48)

$$\Delta\lambda_{3dB} \simeq \frac{2.509}{\pi} \frac{\Delta n_{ph}(\lambda_0)}{\Delta n_{gr}(\lambda_0)} \frac{\lambda_0}{N},$$

where $\Delta n_{gr}(\lambda_0) \simeq 0.08$ as measured separately by means described in [24]. The nearest side lobes to the main transmission are down by about 9dB and agree closely with the 9.5dB value anticipated for uniform coupling.

Reduction of side lobes for channel 0 was accomplished by tapering the voltage

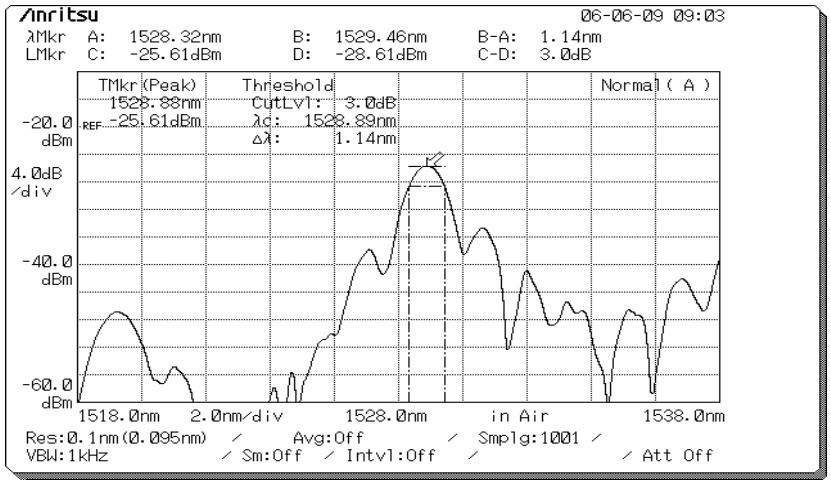

(a) TM polarization input, λ_0=1528.88 nm, FWHM=1.14 nm

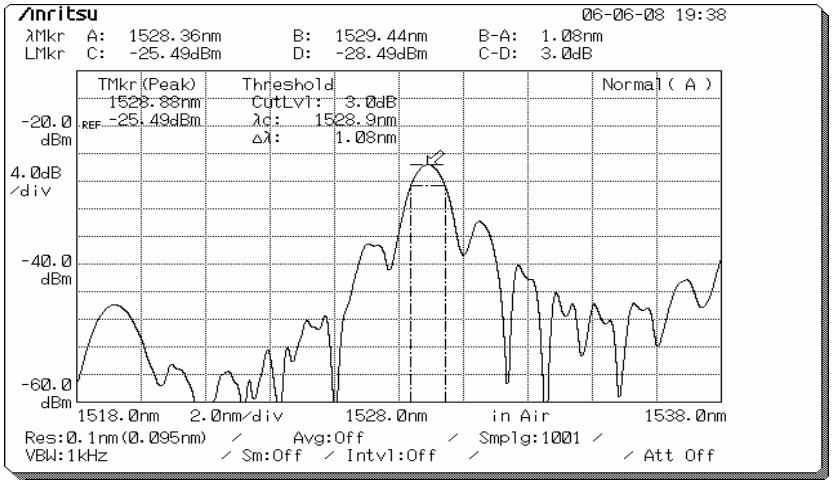

(b) TE polarization input, λ_0=1528.88 nm, FWHM=1.08 nm

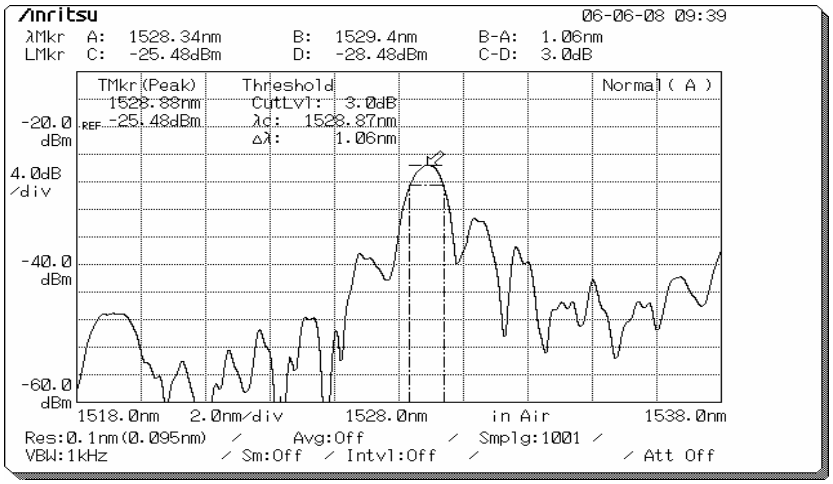

(c) 45º between TM and TE polarization input, λ_0=1528.88 nm, FWHM=1.06 nm

Fig. 29. Output spectra for the center frequency of the tuning range (channel 0) obtained with uniform coupling (voltage), sample P46, device FI#2.

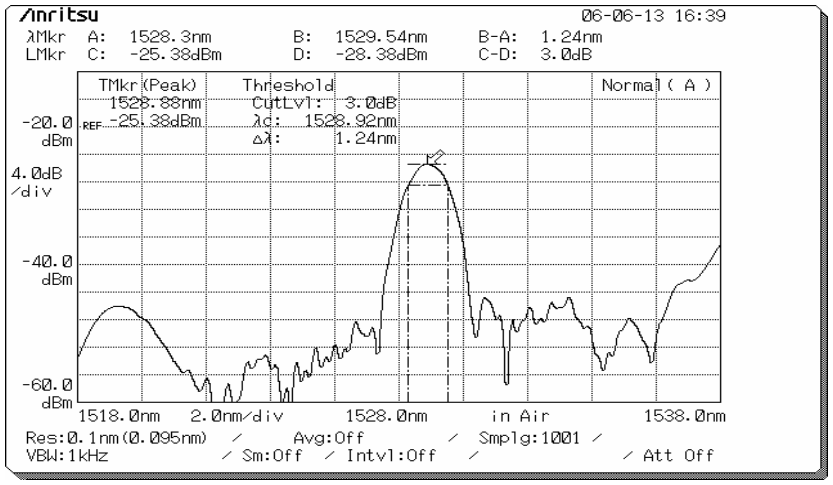

(a) TM polarization input, λ_0=1528.88 nm, FWHM=1.24 nm

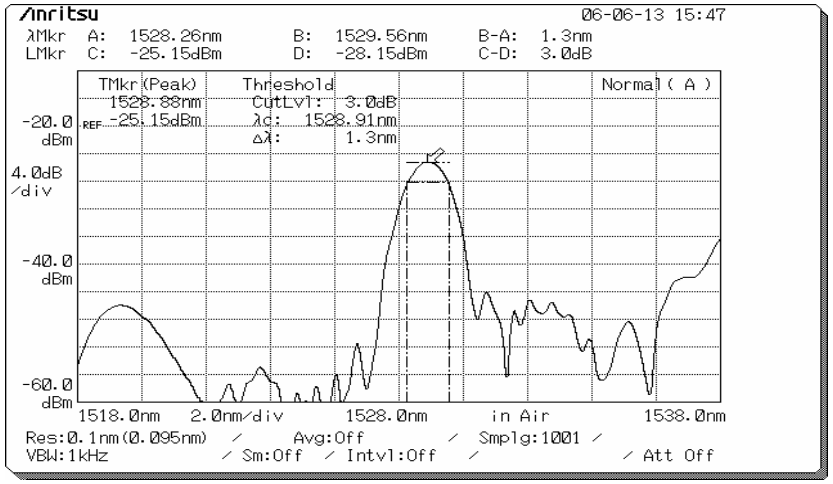

(b) TE polarization input, λ_0=1528.88 nm, FWHM=1.3 nm

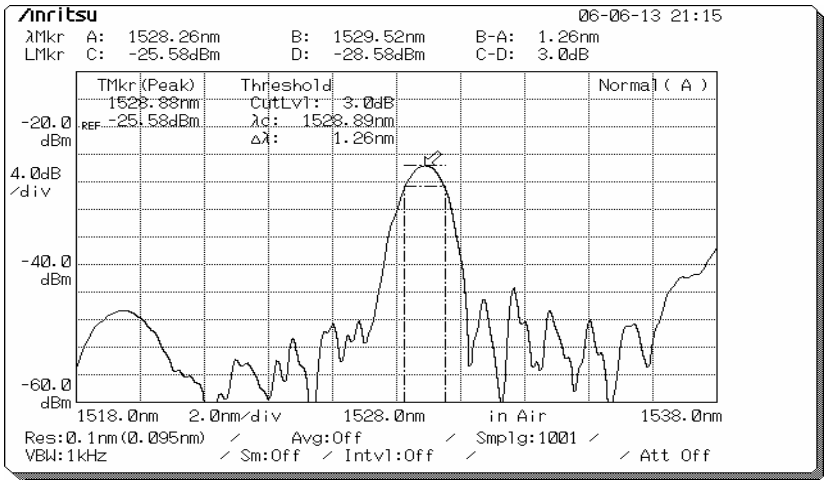

(c) 45º between TM and TE polarization input, λ_0=1528.88 nm, FWHM=1.26 nm

Fig. 30. Output spectra for the center frequency of the tuning range (channel 0) obtained with apodized coupling (voltage), sample P46, device FI#2.

applied on different electrode sets using a raised cosine function distribution. The results are shown in Fig. 30. Output spectra for all three input cases are given: TM, polarization, TE polarization and 45º between TM and TE polarization.

As depicted in Fig. 30, the center wavelength for channel 0 after apodization remains 1528.88 nm. Side lobes are reduced to about 20 dB below peak transmission for all three polarization input cases and agree with the theoretical prediction value. The 3dB bandwidth increases to ~ 1.3 nm as a result of apodization.

The transmission spectra for both TM and TE polarization input are re-plotted together in Fig. 31 and both curves match each other closely. The relative power represents the output of the filter normalized to the spectrum of the broadband source of the input erbium doped fiber.

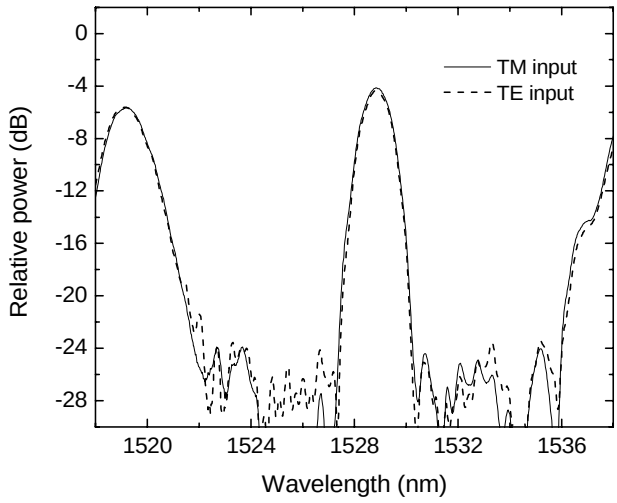

Fig. 31. Output spectra at relative power for channel 0 obtained with apodized coupling (voltage), sample P46, device FI#2.

In Fig. 32, the output spectrum testing result at 45º between TM and TE polarization input for channel 0 with apodized coupling is compared to the calculated

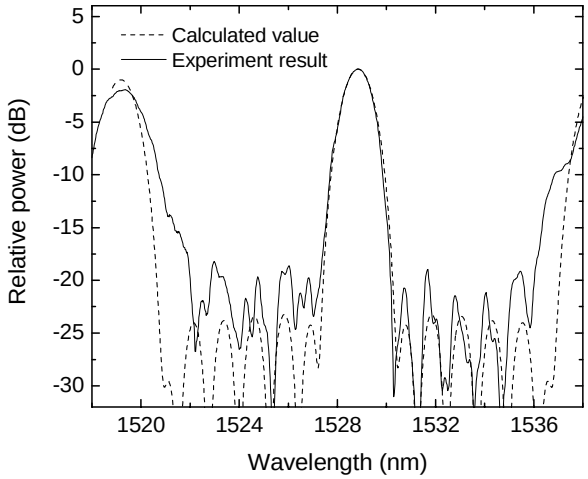

Fig. 32. Comparison of the output spectrum testing result at 45° polarization input for channel 0 with apodized coupling vs. the calculated spectrum response, sample P46, device FI#2.

spectrum response. The apodization function used was given as $1+0.6\cos(2\pi(y/L-0.5))$. The overall power level of the testing curve is raised up by 4.15 dB to compensate for the insertion loss through the device. The center transmission lobe matches the calculated curve closely. The mismatch in the side lobes is most likely caused by surface charges in the SiO_2 layer that prevents the realization of the desired electric field distribution for apodization. Slight dislocation in the electrode sets position induced by photolithography and etching process may also contribute to this problem.

D-2. Spectral response of various channels

Various channels selection is achieved by adjusting the voltages applied on each electrode sets according to a weighting factor which is proportional to the amplitudes of two cosine functions shifted by $\pi/2$ due to the $\Lambda/4$ offset distance between two successive electrode sets. Fig. 33 shows the output spectra for different channels with uniform coupling.

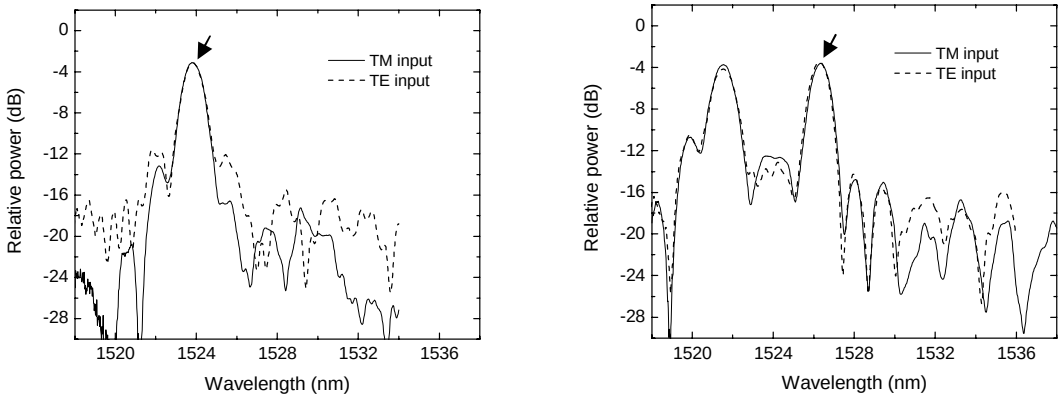

(a) channel -4 (b) channel -2

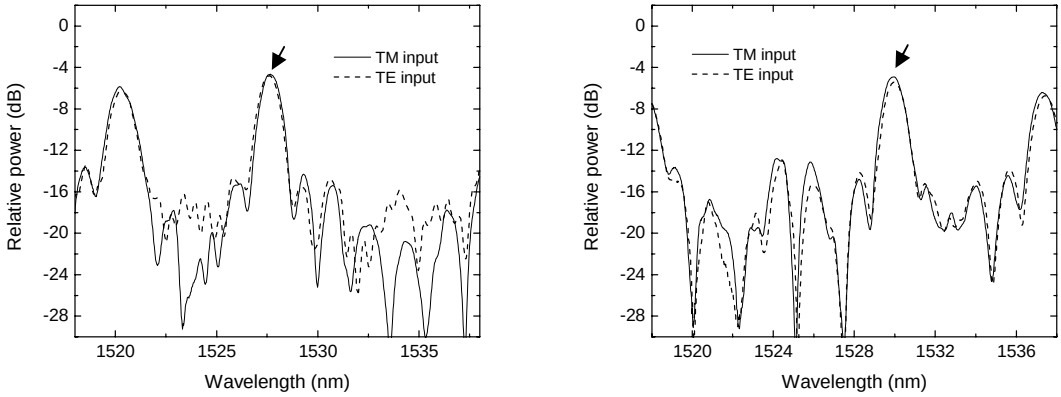

(c) channel -1 (d) channel +1

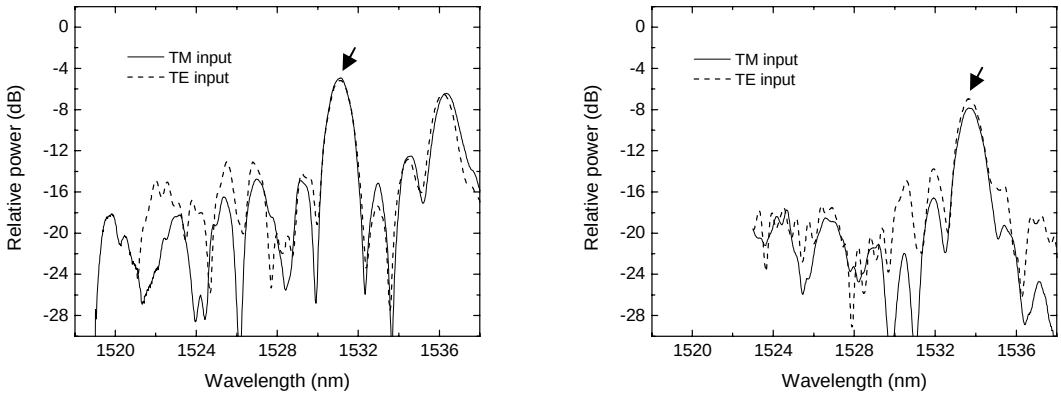

(e) channel +2 (f) channel +4

Fig. 33. Output spectra for different channels with uniform coupling, sample P46, device FI#2. The arrows indicate the selected channel.

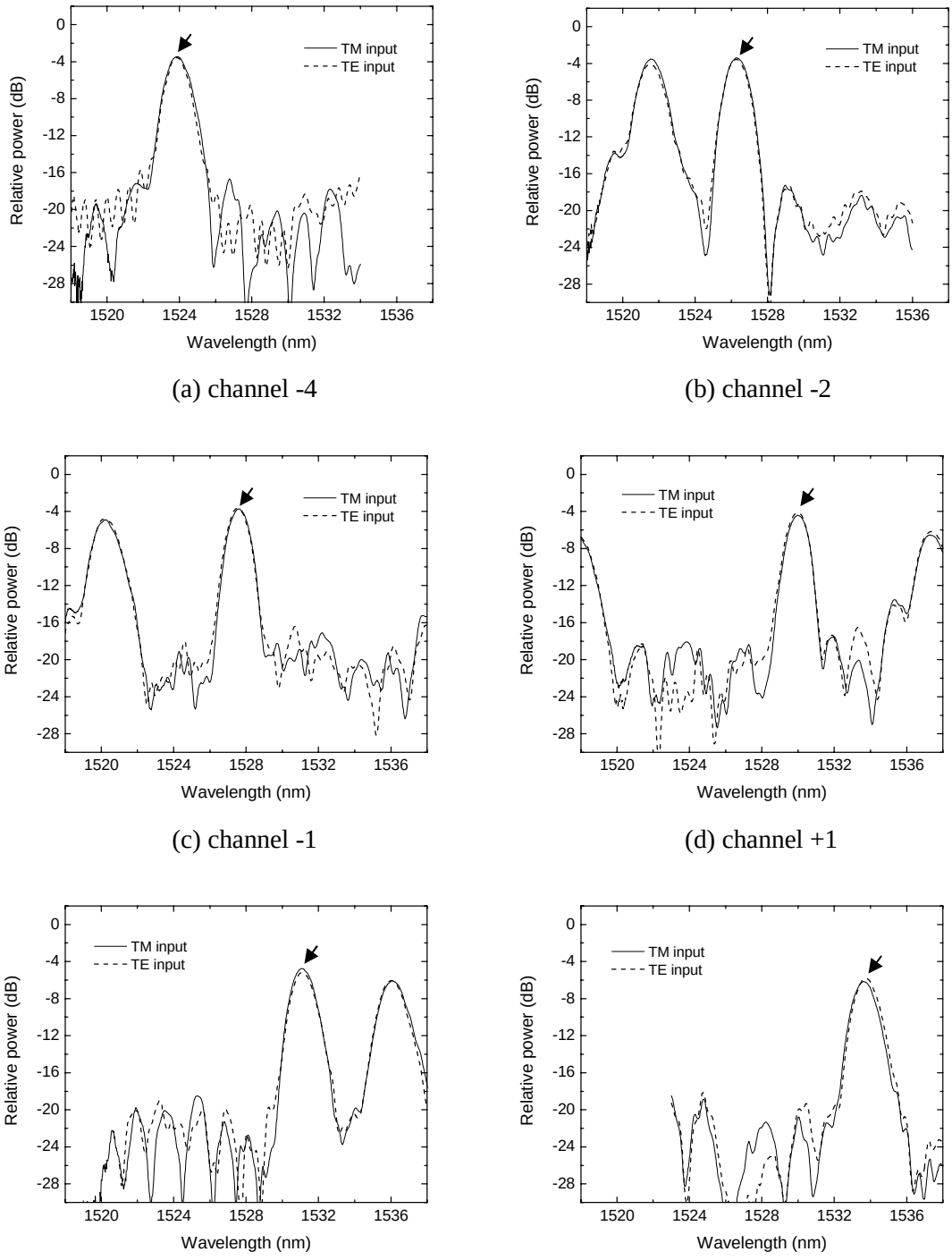

(a) channel -4 (b) channel -2

(c) channel -1 (d) channel +1

(e) channel +2 (f) channel +4

Fig. 34. Output spectra for different channels with apodized coupling, sample P46, device FI#2. The arrows indicate the selected channel.

Fig. 34 illustrates the output spectra when apodization was used to suppress side lobes for all channels. Some side lobes are higher than the calculated value of -20 dB. The height and shape of these side lobes can be changed by small adjustment of the applied voltages from their calculated values. This indicates the cause is mostly likely due to the presence of surface charges in the SiO_2 layer, which interfere with the voltage that is applied for apodization thus preventing the realization of the desired electrical field for apodization.

D-3. Channel spacing and tuning range

The peak transmission wavelengths for different channels with apodized coupling are plotted in Fig. 35. Channel spacing is 1.1~1.2 nm between adjacent channels which is close to the calculated value of 1.3 nm from equation (54). The tuning ranges from 1524.04 to 1533.56 nm in both TM and TE polarization input cases.

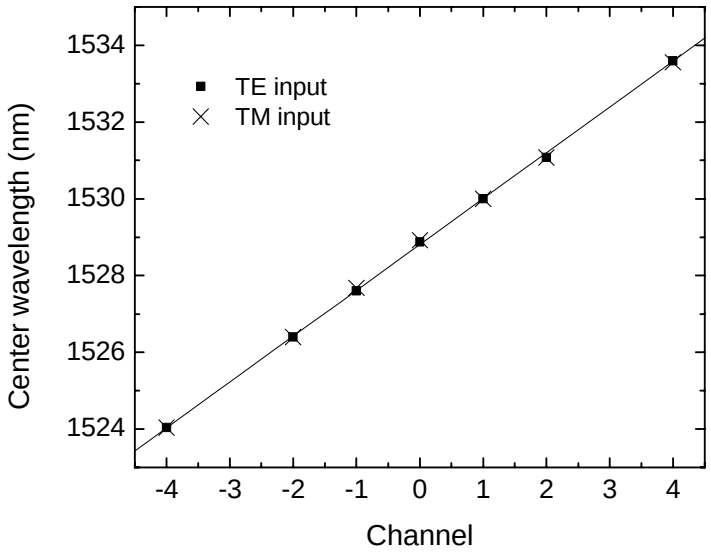

Fig. 35. Peak transmission wavelengths for different channels with apodized coupling.

D-4. Wavelength dependent loss and polarization dependent loss

Table 5. Insertion loss (dB) at peak transmission wavelength for each channel with apodized coupling.

Channel number	-4	-3	-2	-1	0	+1	+2	+3	+4
TE input	-3.58	NA	-3.56	-3.68	-4.36	-4.15	-5.20	NA	-5.81
TM input	-3.45	NA	-3.40	-3.72	-4.15	-4.41	-4.75	NA	-6.15

Fiber-to-fiber insertion loss of the filter is measured by comparing the power level at the output peak transmission wavelength to the power level of the input broadband source of the erbium doped fiber at the same wavelength. The values for each channel can be determined from Fig. 34 directly by observing the power level at the peak transmission for each channel and are summarized in Table 5. Fig. 36 plots the insertion loss at different wavelengths.

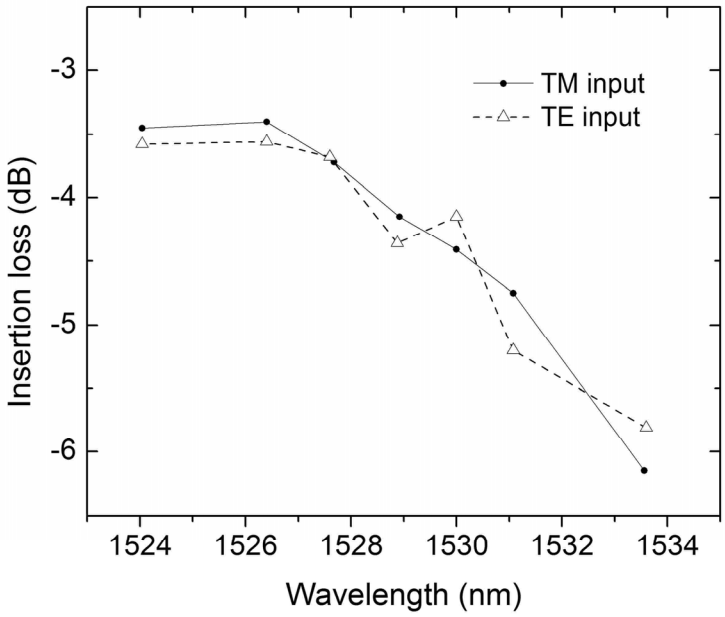

Fig. 36. Fiber-to-fiber insertion loss vs. wavelength with apodized coupling.

Polarization dependent loss, which is the difference between TM and TE input mode loss, is less than 0.5 dB for all channels as illustrated in Fig. 36.

It is shown that at shorter wavelength (~1524 nm) the filter exhibits lower insertion loss than at longer wavelength (~1533.5 nm). This may be due to the fact that optical wave encounters different insertion loss at different wavelength even on a straight channel waveguide which is not covered by mode coupling electrodes pairs, as illustrated in Fig. 37.

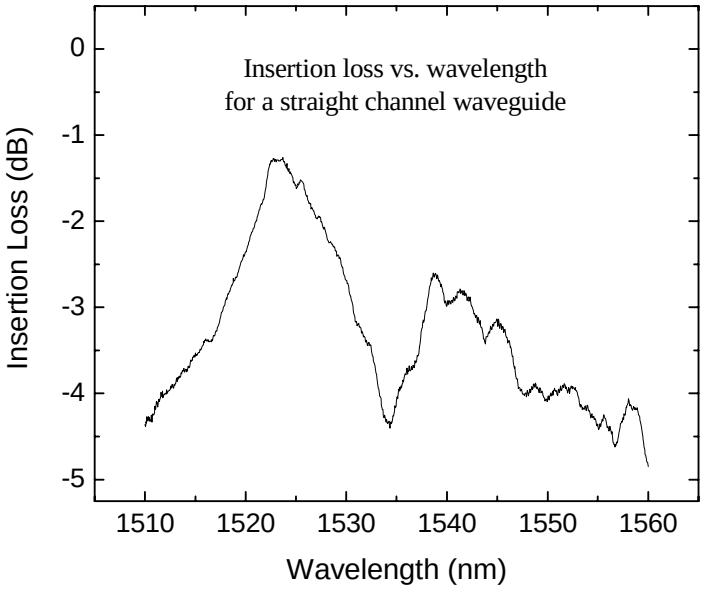

Fig. 37. Insertion loss vs. wavelength for a straight channel waveguide which is not covered with electrodes pairs, on sample P46.

D-5. Response time of the filter

The electro-optic filter inherently exhibits fast tuning speed. The tuning response time is primarily limited by electrodes design and the speed of electronics in power supplies that are used to supply voltages on the electrode sets [13]. Fig. 38 shows the

output optical signal response to a 21 V step change in the voltages applied on every other electrode sets.

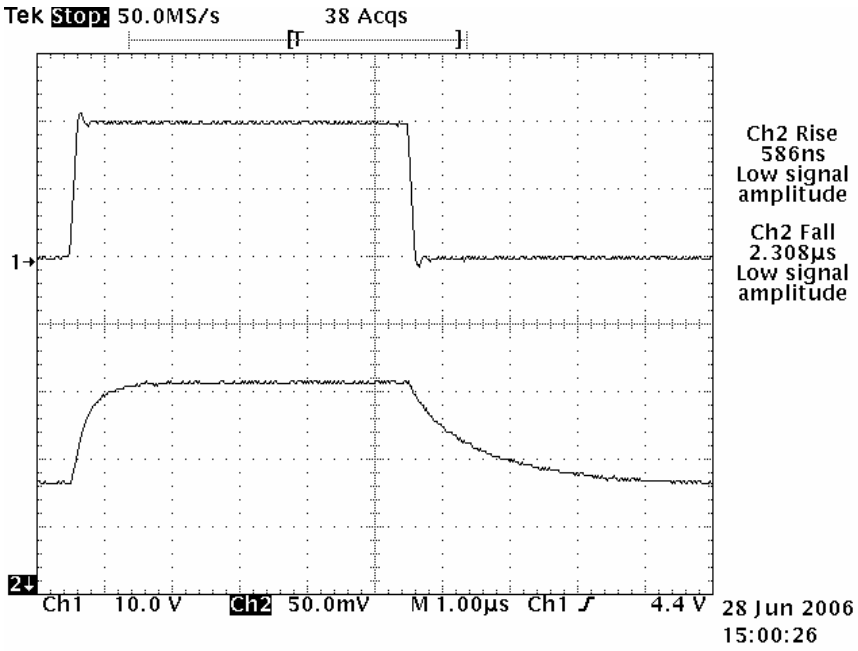

Fig. 38. Temporal response of the filter with 21 V step change in tuning voltages. Upper trace is applied voltage, lower trace is optical output.

Trace 1 is the applied voltage signal on the electrodes, and trace 2 is the optical output signal obtained with an APD photodetector. The 10%-90% rise time is 586 ns and the 90%-10% fall time is 2.308 µs. The fact that fall time is much longer than rise time indicates the existence of moving charges in the SiO_2 layer, which relax after the applied voltage drops to zero. A better quality SiO_2 layer should therefore decrease the fall response time. Both rise time and fall time can be further improved by better electrodes design and better wire connections to decrease the resistance between the voltage supply and electrodes (e.g. avoid using conductive epoxy in wire connection).

E. Suggestion for future work

An important expansion of this research is a tunable four-port polarization independent optical add-drop filter. The design is illustrated in Fig. 39. It consists of one directional coupler near the input side, another one near the output side and two electrooptic polarization converter sections. It differs from the conventional filters design in the following respects [8]: (1) polarization beam splitters (PBS's) are not required; (2) the optical path difference between the two waveguide arms of the interferometer is half-wavelength; (3) the relative positions of the polarization coupling regions in the two waveguides arms are displaced in the propagation direction by half of the spatial period of the perturbation responsible for polarization coupling. The 2nd and 3rd features have been demonstrated in this research.

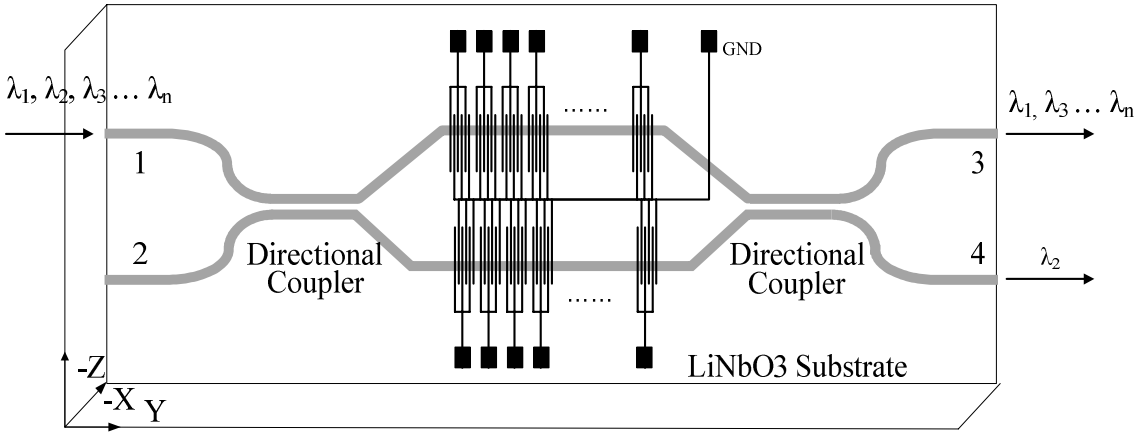

Fig. 39. 4-port add-drop filter configuration for EMFs.

In this structure, an incident wavelength-multiplexed signal (λ_1, λ_2, λ_3,…λ_n) into port 1 would drop only a phase-matched wavelength (say λ_2) to output 4, and all other

wavelengths would emerge from output 3. The drop wavelength can be selected by means of an applied tuning voltage through the surface electrodes.

To expand the total tuning range of this type of electrooptically phase matched filter devices, the number of electrode sets P needs to be increased. For 100 GHz (~0.8nm) channel spacing as used in WDM system, a total length of about 4 cm electrodes mode coupling region divided into 198 individual sets is required to address 100 channels, for a total tuning range of 80 nm.

CHAPTER V

CONCLUSIONS

Electro-optic tunable filters (EOTFs) are enabling technology for WDM systems. For that purpose, two-port electro-optically wavelength tunable filters based on asymmetric Mach-Zehnder structure in $LiNbO_3$ substrate using Ti-indiffusion technology has been developed for 1.55μm application. To produce the filter, fabrication parameters for channel waveguides, Mach-Zehnder interferometer waveguides and polarization converters were optimized.

Straight channel waveguides 7μm in width were produced by diffusing 1116 Å thick Ti into $LiNbO_3$ substrate at 1035°C for 10 hours. Single mode guiding has been realized for both TE and TM polarization. Insertion loss of 2.9 dB for TE polarization input and 3.3 dB for TM polarization input were achieved on a 46 mm long sample.

Mach-Zehnder interferometer performance was characterized by testing the output power of both symmetric Mach-Zehnder interferometer and asymmetric Mach-Zehnder interferometer waveguides on the same sample. The performance was optimized by maximizing the output power of the symmetric interferometer and minimizing the output power of the asymmetric interferometer. Devices were produced with Ti film thickness of 1116 Å. Best results were obtained by diffusing the sample at 1035°C for 9+1 hours. For the symmetric interferometer, fiber-to-fiber insertion loss of 4.3 dB for TE polarization and 5.2 dB for TM polarization were achieved.

Programmable polarization mode converters with 16 electrode sets each containing 64 grating period Λ were produced on a straight channel waveguide. The separation

between adjacent electrode sets alternates between $\left(72 \pm \frac{1}{4}\right)\Lambda$ to select one-sideband single channel. Programmability was achieved by applying spatially periodic weighted independent voltages to interdigital electrode sets. A driving circuit for voltage application to the various electrode sets was implemented using a digital-to-analog converter (DAC) array and controlled via a personal computer. Optical testing was carried out when the substrate was cooled at 17ºC to shift the center frequency near the peak of the erbium doped fiber output spectrum. Maximum conversion efficiency of more than 99% was achieved for both TM→TE and TE→TM, and was observed at 1530.48 nm. For uniform coupling, the 3dB bandwidth is 1.06nm and the nearest side lobes are about 9.7 dB down from the main peak. A raised cosine shaped voltage distribution was used to suppress the side lobes to about 17 dB below the main transmission peak for both input polarization. The 3dB bandwidth increased to 1.22nm as a result of apodization. Channel selection is achieved by independently changing the voltages on each electrodes set. A total of 7 channels were selectable for a 16 electrode sets case: channel -4, -2, -1, 0, +1, +2 and +4, with channel +3 and channel -3 missing. The wavelength tuning ranges from 1525.6 to 1535.2 nm. A similar approach for the two-sideband device was demonstrated in [37].

A two-port programmable polarization-independent electro-optically wavelength tunable filter has been produced based on the above results. Center wavelength of the tuning range is observed at 1528.88 nm at 18ºC for three tested polarization input cases (TM, TE, and 45º between TM and TE). The 3dB bandwidth is about 1.1 nm and the nearest side lobes to the main transmission are down by about 9 dB for uniform coupling.

Side lobes are reduced to about 20 dB below peak transmission after apodization and the 3dB bandwidths increase to ~ 1.3 nm as a result. Satellite peaks appear at ~ ±10 nm away from center frequency. The spectral locations of these satellite peaks can be pushed further away from the center by increasing the number of electrode sets P. Seven different channels (channel -4, -2, -1, 0, +1, +2 and +4) were selected by programming the voltages on each electrodes set. Channel spacing is about 1.1~1.2 nm. The tuning ranges from 1524.04 to 1533.56 nm for both TM and TE polarization input. Fiber-to-fiber insertion loss of the filter at center frequency is 4.3 dB for TE input and 4.2 dB for TM input. Polarization dependent loss is < 0.5 dB for all the selected channels. The temporal response to a 21 V step change in applied voltages was measured to be 586 ns for the 10%-90% rise time and 2.308 μs for the 90%-10% fall time.

REFERENCES

1. B. Mukherjee, *Optical Communication Networks.* New York: McGraw-Hill, 1997.
2. H. Zhu and B. Mukherjee, “Online connection provisioning in metro optical WDM networks using reconfigurable OADMS (ROADMS)”, *The 13th IEEE Workshop on Local and Metropolitan Area Networks*, pp. 7-10, Apr. 2004.
3. N. Ben-Horrin, G. Kronenthal and A. Queller, “Reconfigurability ROADMap: extending static OADM,” *Lightwave*, pp. 31, Nov. 2003.
4. L. Wiebel, “Optical technology, ROADM, mounts a comeback,” *EE Times*, Sep. 25, 2003.
5. H. Kobrinski and K. Cheung, “Wavelength-tunable optical filters: Applications and technologies,” *IEEE Communications Magazine*, pp. 53-63, Oct. 1989.
6. D. Sadot and E. Boimovich, “Tunable optical filters for dense WDM networks,” *IEEE Communications Magazine*, pp. 50-55, Dec. 1998.
7. J. M. H Elmirghani and H. T. Mouftah, “Technologies and architectures for scalable dynamic dense WDM networks,” *IEEE Communications Magazine*, pp. 58-66, Feb. 2000.
8. H. F. Taylor and O. Eknoyan, “Guided wave acousto-optic and electro-optic tunable filter designs with relaxed beam-splitter requirements,” *Applied Optics*, vol. 39, no. 1, pp.124-128, Jan. 2000.
9. W. Warzanskyj, F. Heismann and R. C. Alferness, “Polarization-independent electro-optically tunable narrow-band wavelength filter,” *Applied. Physics Letters*, vol. 53, no. 1, pp. 13-15, Jul. 1988.

10. P. E. Green, Jr., *Fiber Optic Networks*. Englewood Cliffs, NJ: Prentice Hall, 1993.
11. Z. Tang, O. Eknoyan and H. F. Taylor, "Polarization-independent electro-optically tunable wavelength filter in $LiTaO_3$," *Electronics Letters*, vol. 30, no. 21, pp. 1758-1759, 1994.
12. H. F. Taylor and O. Eknoyan, "Guided wave acousto-optic and electro-optic tunable filter designs with relaxed beam splitter requirements," *Applied Optics*, vol. 39, no. 1, pp. 124-128, Jan. 2000.
13. P. Tang, O. Eknoyan and H. F. Taylor, "Rapidly tunable polarisation independent optical add drop multiplexer in Ti:$LiNbO_3$," *Electronics Letters*, vol. 38, pp. 242-244, Feb. 2002.
14. P. Tang, O. Eknoyan and H. F. Taylor**, "**Rapidly tunable optical add-drop multiplexer (OADM) using a static-strain-induced grating in $LiNbO_3$," *Journal of Lightwave Technoogy,* vol. 21, no. 1, pp. 236-245, Jan. 2003.
15. Y. Ping, O. Eknoyan and H. F. Taylor, "Polarisation-independent tunable bandpass filter utilising symmetric branch beam splitters," *Electronics Letters*, vol. 40, no. 15, pp. 960-962, Jul. 2004.
16. H. F. Taylor, "Tunable spectral slicing filters for dense wavelength-division multiplexing," *Journal of Lightwave Technoogy,* vol. 21, no. 3, pp. 837-847, Mar. 2003.
17. D. K. Cheng, *Fundamentals of Engineering Electromagnetics*. Upper Saddle River, NJ: Prentice Hall, 1993.
18. Amnon Yariv, *Quantum Electronics*, 3rd edition. New York: John Wiley & Sons, 1989.

19. T. E. Murphy, “Integrated optical grating-based matched filters for fiber-optic communications,” M. S. Thesis. Massachusetts Institute of Technology, Cambridge, MA, 1996.
20. T. Tamir, *Guided-Wave Optoelectronics*. Berlin: Spring-Verlag, 1988.
21. H. Nishihara, M. Haruna, and T. Suhara, *Optical Integrated Circuits*. New York: McGraw-Hill, 1989.
22. D. F. Nelson and R. M. Mikulyak, “Refractive indices of congruently melting lithium niobate,” *Journal of Applied Physics*, vol. 45, no. 8, pp. 3688-3689, Aug. 1974.
23. Z. Tang, “Study of utilizing static photoelastic effect in integrated optical devices,” Ph.D. Dissertation, Texas A&M University, Department of Electrical Engineering, College Station, Texas, 1994.
24. F. Heismann, R. C. Alferness, “Wavelength-tunable electrooptic polarization conversion in birefringent waveguides”, *Journal of Quantum Electronics*, vol. 24, no. 1, pp. 83-93, Jan. 1988.
25. R. C. Alferness and L. L. Buhl, “Long-wavelength Ti:$LiNbO_3$ waveguide electro-optic TE↔TM converter,” *Electronics Letters*, vol. 19, no. 2, pp. 40-41, Jan. 1983.
26. I. R. Croston, A. D. Carr, N. J. Parsons, S. N. Radcliffe and L. J. St. Ville, “Lithium Niobate electro-optic tunable filter with high sidelobe suppression,” *Electronics Letters*, vol. 29, no. 2, pp. 157-159, Jan. 1993.
27. H. F. Taylor, “Frequency-selective coupling in parallel dielectric waveguides”, *Optics Communications*, vol. 8, no. 4, pp. 421-425, 1973.
28. H. Sakata, “Sidelobe suppression in grating-assisted wavelength-selective couplers”,

Optics Letters, vol. 17, no. 7, pp. 463-465, Apr. 1992.

29. D. P. Morgan, “Spatially-variant coupling design for co-directional mode-converting bandpass filters”, *Proceedings of SPIE*, vol. 651, pp. 139-146, 1986.
30. R. C Alferness and P. S. Cross, “Filter characteristics of codirectionallly coupled waveguides with weighted coupling”, *Journal of Quantum Electronics,* vol. 14, no. 11, pp. 843-847, Nov. 1978.
31. E. N. Leith, A. Kozma, J. Upatnieks, J. Marks and N. Massey, “Holographic data storage in three-dimensional media”, *Applied Optics*, vol. 5, no. 8, pp. 1303-1311, Aug. 1966.
32. Personal communications with O. Eknoyan, Texas A&M University, Dept. of Electrical Engineering, College Station, Texas, 2003.
33. S. Suyama, A. Okamoto, and T. Serikawa, “The effect of oxygen-argon mixing on properties of sputtered silicon dioxide films”, *Journal of the Electrochemical Society,* vol. 134, no. 9, pp. 2260-2264, Sep. 1987.
34. W. Wu and B. Chiou, “Properties of radio frequency magnetron sputtered silicon dioxide films”, *Applied Surface Science*, vol. 99, no. 3, pp. 237-243, Jul. 1996.
35. E. V. Jelenkovic and K. Y. Tong, “Effect of annealing temperature on electrical stability of radio frequency magnetron sputtered silicon oxides”, *Journal of Vacuum Science & Technology B: Microelectronics Processing and Phenomena*, vol. 15, no. 2, pp. 209-213, Mar. 1997.
36. Y. Ping, “Two-port polarization independent electro-optically tunable wavelength filter in lithium niobate”, M. S. Thesis, Texas A&M University, College Station, TX, 2003.

37. H. Okayama and M. Kawahara, “Programmable electro-optic waveguide filter”, *Applied Physics Letter*, vol. 61, no. 23, pp. 2753-2755, Dec. 1992.

38. W. K. Burns, T. G. Giallorenzi, R. P. Moeller, and E. J. West, “Interferometric waveguide modulator with polarization-independent operation,” *Applied Physics Letters*, vol. 33, no. 11, pp. 944-947, Dec. 1978.

APPENDIX 1

MECHANISM OF CHANNEL SELECTION FOR EMF DEVICE

(8 ELECTRODE SETS)

This section describes the algorithm for choosing electrode voltages to apply on an EMF device. For simplicity, only the case of 8 electrode sets is discussed. Electrode voltages selection for more complex cases (eg. 16, 32 … electrode sets) can be derived following similar steps.

Recall from Chapter III, the coupling coefficient κ is directly related to the voltage applied on each electrode set. Whether a certain frequency is selected or not is determined by

$$\int_0^L \kappa_j(y) e^{-i\Delta_k y} dy = \frac{\pi}{2}\delta_{jk},$$

where k is the channel number to be selected, j refers to each one of the electrode sets and varies in this case between 1 and 8. $\Delta_k = \frac{2\pi\left|n_{1g} - n_{3g}\right|(\nu_k - \nu_0)}{c}$ is the phase mismatch factor for a specific frequency. A channel is selected only if the above integration result equals π/2, i.e.

$$\int_0^L \kappa_j(y) e^{-i\Delta_j y} dy = \frac{\pi}{2}.$$

A. Two sideband EMFs channel selection

1. Channel 0, $\Delta_0 = 0$

Assuming uniform voltage are applied to all the electrode sets, i.e. $\kappa_0(z) = \kappa_0$, thus

$$\int_0^L \kappa_0(z)e^{-i\Delta_0 z}\cdot dz = \int_0^L \kappa_0 \cdot dz = \kappa_0 L = \frac{\pi}{2}.$$

2. Channel ±1, default condition: $\Delta_{\pm 1}L = \pm 2\pi$, $\Rightarrow \Delta_1 = \dfrac{2\pi}{L}$

$$\int_0^L \kappa_1(z)e^{-i\Delta_1 z}\cdot dz = \int_0^{\frac{L}{8}} \kappa_1(z)e^{-i\Delta_1 z}dz + \int_{\frac{L}{8}}^{\frac{L}{4}} \kappa_1(z)e^{-i\Delta_1 z}dz + \int_{\frac{L}{4}}^{\frac{3L}{8}} \kappa_1(z)e^{-i\Delta_1 z}dz + \int_{\frac{3L}{8}}^{\frac{L}{2}} \kappa_1(z)e^{-i\Delta_1 z}dz +$$
$$\int_{\frac{L}{2}}^{\frac{5L}{8}} \kappa_1(z)e^{-i\Delta_1 z}dz + \int_{\frac{5L}{8}}^{\frac{3L}{4}} \kappa_1(z)e^{-i\Delta_1 z}dz + \int_{\frac{3L}{4}}^{\frac{7L}{8}} \kappa_1(z)e^{-i\Delta_1 z}dz + \int_{\frac{7L}{8}}^{L} \kappa_1(z)e^{-i\Delta_1 z}dz.$$

Rewrite the integration as

$$\int_0^L \kappa_1(z)e^{-i\Delta_1 z}\cdot dz = \int_0^L \kappa_1(z)\cos\Delta_1 z\cdot dz - i\int_0^L \kappa_1(z)\sin\Delta_1 z\cdot dz.$$

The following two conditions must be satisfied in order to select channel ±1:

$$\begin{cases} \int_0^L \kappa_1(z)\cos\Delta_1 z\cdot dz = \dfrac{\pi}{2} \\ -i\int_0^L \kappa_1(z)\sin\Delta_1 z\cdot dz = 0 \end{cases}.$$

(1) The imaginary integration part

$$-i\int_0^L \kappa_1(z)\sin\Delta_1 z\cdot dz = -i[\int_0^{\frac{L}{8}} \kappa_1(z)\sin\Delta_1 z\cdot dz + \int_{\frac{L}{8}}^{\frac{L}{4}} \kappa_1(z)\sin\Delta_1 z\cdot dz + \int_{\frac{L}{4}}^{\frac{3L}{8}} \kappa_1(z)\sin\Delta_1 z\cdot dz + \int_{\frac{3L}{8}}^{\frac{L}{2}} \kappa_1(z)\sin\Delta_1 z\cdot dz +$$
$$\int_{\frac{L}{2}}^{\frac{5L}{8}} \kappa_1(z)\sin\Delta_1 z\cdot dz + \int_{\frac{5L}{8}}^{\frac{3L}{4}} \kappa_1(z)\sin\Delta_1 z\cdot dz + \int_{\frac{3L}{4}}^{\frac{7L}{8}} \kappa_1(z)\sin\Delta_1 z\cdot dz + \int_{\frac{7L}{8}}^{L} \kappa_1(z)\sin\Delta_1 z\cdot dz].$$

Let's assume $\kappa_1(z)$ is constant within each electrode set region, i.e.

$$\kappa_1(z) = \kappa_1 \cdot \kappa_{1i}^{'},\quad i = 1...8,$$

where κ_1 is a constant and $\kappa_{1i}^{'}$ is a proportionality constant of magnitude $\left|\kappa_{1i}^{'}\right| < 1$.

Therefore,

$$-i\int_0^L \kappa_1(z)\sin\Delta_1 z\cdot dz = -i\kappa_1\cdot\Big[\int_0^{\frac{L}{8}}\kappa_{11}'\sin\Delta_1 z\cdot dz+\int_{\frac{L}{8}}^{\frac{L}{4}}\kappa_{12}'\sin\Delta_1 z\cdot dz+\int_{\frac{L}{4}}^{\frac{3L}{8}}\kappa_{13}'\sin\Delta_1 z\cdot dz+\int_{\frac{3L}{8}}^{\frac{L}{2}}\kappa_{14}'\sin\Delta_1 z\cdot dz+$$
$$\int_{\frac{L}{2}}^{\frac{5L}{8}}\kappa_{15}'\sin\Delta_1 z\cdot dz+\int_{\frac{5L}{8}}^{\frac{3L}{4}}\kappa_{16}'\sin\Delta_1 z\cdot dz+\int_{\frac{3L}{4}}^{\frac{7L}{8}}\kappa_{17}'\sin\Delta_1 z\cdot dz+\int_{\frac{7L}{8}}^{L}\kappa_{18}'\sin\Delta_1 z\cdot dz\Big]$$
$$=i\frac{\kappa_1}{\Delta_1}\Big[\kappa_{11}'\cos\Delta_1 z\Big|_{\Delta_1 z=0}^{\Delta_1 z=\pi/4}+\kappa_{12}'\cos\Delta_1 z\Big|_{\Delta_1 z=\pi/4}^{\Delta_1 z=\pi/2}+\kappa_{13}'\cos\Delta_1 z\Big|_{\Delta_1 z=\pi/2}^{\Delta_1 z=3\pi/4}+\kappa_{14}'\cos\Delta_1 z\Big|_{\Delta_1 z=3\pi/4}^{\Delta_1 z=\pi}+$$
$$\kappa_{15}'\cos\Delta_1 z\Big|_{\Delta_1 z=\pi}^{\Delta_1 z=5\pi/4}+\kappa_{16}'\cos\Delta_1 z\Big|_{\Delta_1 z=5\pi/4}^{\Delta_1 z=3\pi/2}+\kappa_{17}'\cos\Delta_1 z\Big|_{\Delta_1 z=3\pi/2}^{\Delta_1 z=7\pi/4}+\kappa_{18}'\cos\Delta_1 z\Big|_{\Delta_1 z=7\pi/4}^{\Delta_1 z=2\pi}\Big].$$

We take the values of κ_{1i}' based on a cosine value distribution as shown in Fig. 14 (a)

$$\kappa_{11}'=\cos\left(\frac{\pi}{8}\right)=0.924,\qquad \kappa_{12}'=\cos\left(\frac{3\pi}{8}\right)=0.383,$$
$$\kappa_{13}'=\cos\left(\frac{5\pi}{8}\right)=-0.383,\quad \kappa_{14}'=\cos\left(\frac{7\pi}{8}\right)=-0.924,$$
$$\kappa_{15}'=\cos\left(\frac{9\pi}{8}\right)=-0.924,\quad \kappa_{16}'=\cos\left(\frac{11\pi}{8}\right)=-0.383,$$
$$\kappa_{17}'=\cos\left(\frac{13\pi}{8}\right)=0.383,\quad \kappa_{18}'=\cos\left(\frac{15\pi}{8}\right)=0.924.$$

Substitute the values of κ_{1i}' into the integration above, it follows that

$$-i\int_0^L \kappa_1(z)\sin\Delta_1 z\cdot dz=0\,.$$

(2) The real part integration

$$\int_0^L \kappa_1(z)\cos\Delta_1 z\cdot dz=\kappa_1\cdot\Big[\int_0^{\frac{L}{8}}\kappa_{11}'\cos\Delta_1 z\cdot dz+\int_{\frac{L}{8}}^{\frac{L}{4}}\kappa_{12}'\cos\Delta_1 z\cdot dz+\int_{\frac{L}{4}}^{\frac{3L}{8}}\kappa_{13}'\cos\Delta_1 z\cdot dz+\int_{\frac{3L}{8}}^{\frac{L}{2}}\kappa_{14}'\cos\Delta_1 z\cdot dz+$$
$$\int_{\frac{L}{2}}^{\frac{5L}{8}}\kappa_{15}'\cos\Delta_1 z\cdot dz+\int_{\frac{5L}{8}}^{\frac{3L}{4}}\kappa_{16}'\cos\Delta_1 z\cdot dz+\int_{\frac{3L}{4}}^{\frac{7L}{8}}\kappa_{17}'\cos\Delta_1 z\cdot dz+\int_{\frac{7L}{8}}^{L}\kappa_{18}'\cos\Delta_1 z\cdot dz\Big]$$
$$=\frac{\kappa_1}{\Delta_1}\Big[\kappa_{11}'\sin\Delta_1 z\Big|_{\Delta_1 z=0}^{\Delta_1 z=\pi/4}+\kappa_{12}'\sin\Delta_1 z\Big|_{\Delta_1 z=\pi/4}^{\Delta_1 z=\pi/2}+\kappa_{13}'\sin\Delta_1 z\Big|_{\Delta_1 z=\pi/2}^{\Delta_1 z=3\pi/4}+\kappa_{14}'\sin\Delta_1 z\Big|_{\Delta_1 z=3\pi/4}^{\Delta_1 z=\pi}+$$
$$\kappa_{15}'\sin\Delta_1 z\Big|_{\Delta_1 z=\pi}^{\Delta_1 z=5\pi/4}+\kappa_{16}'\sin\Delta_1 z\Big|_{\Delta_1 z=5\pi/4}^{\Delta_1 z=3\pi/2}+\kappa_{17}'\sin\Delta_1 z\Big|_{\Delta_1 z=3\pi/2}^{\Delta_1 z=7\pi/4}+\kappa_{18}'\sin\Delta_1 z\Big|_{\Delta_1 z=7\pi/4}^{\Delta_1 z=2\pi}\Big].$$

Substituting κ_{1i}' with the values from section (1) in above, it gives

$$\int_0^L \kappa_1(z)\cos\Delta_1 z\cdot dz=\frac{\pi}{2},\quad(\Delta_1=\frac{2\pi}{L})$$
$$=\kappa_0 L$$
$$\Rightarrow \kappa_1=2.0523\kappa_0$$

and $\kappa_{1i} = \kappa_{1i}^{'}\kappa_1 = 2.0523\cdot\kappa_{1i}^{'}\kappa_0$. Therefore,

$\kappa_{11} = 1.896\kappa_0$, $\kappa_{12} = 0.785\kappa_0$, $\kappa_{13} = -0.785\kappa_0$, $\kappa_{14} = -1.896\kappa_0$,

$\kappa_{15} = -1.896\kappa_0$, $\kappa_{16} = -0.785\kappa_0$, $\kappa_{17} = 0.785\kappa_0$, $\kappa_{18} = 1.896\kappa_0$.

Note that κ_0 is linearly proportional to the uniform voltage V_0 applied to select channel 0. Once we choose V_0 experimentally, we will be able to determine the voltages needed to select channel ±1.

3. Channel ±2, default condition: $\Delta_{\pm 2}L = \pm 4\pi, \Rightarrow \Delta_2 = \dfrac{4\pi}{L}$

(1) The imaginary integration part

Let's assume $\kappa_2(z)$ is constant within each electrode set region, i.e.

$$\kappa_2(z) = \kappa_2\cdot\kappa_{2i}^{'},\quad i = 1...8.$$

Therefore,

$$\begin{aligned}
-i\int_0^L \kappa_2(z)\sin\Delta_2 z\cdot dz = -i\kappa_2\cdot\Big[&\int_0^{\frac{L}{8}}\kappa_{21}^{'}\sin\Delta_2 z\cdot dz + \int_{\frac{L}{8}}^{\frac{L}{4}}\kappa_{22}^{'}\sin\Delta_2 z\cdot dz + \int_{\frac{L}{4}}^{\frac{3L}{8}}\kappa_{23}^{'}\sin\Delta_2 z\cdot dz + \int_{\frac{3L}{8}}^{\frac{L}{2}}\kappa_{24}^{'}\sin\Delta_2 z\cdot dz + \\
&\int_{\frac{L}{2}}^{\frac{5L}{8}}\kappa_{25}^{'}\sin\Delta_2 z\cdot dz + \int_{\frac{5L}{8}}^{\frac{3L}{4}}\kappa_{26}^{'}\sin\Delta_2 z\cdot dz + \int_{\frac{3L}{4}}^{\frac{7L}{8}}\kappa_{27}^{'}\sin\Delta_2 z\cdot dz + \int_{\frac{7L}{8}}^{L}\kappa_{28}^{'}\sin\Delta_2 z\cdot dz\ \Big] \\
= i\frac{\kappa_2}{\Delta_2}\Big[&\kappa_{21}^{'}\cos\Delta_2 z\Big|_{\Delta_2 z=0}^{\Delta_2 z=\pi/2} + \kappa_{22}^{'}\cos\Delta_2 z\Big|_{\Delta_2 z=\pi/2}^{\Delta_2 z=\pi} + \kappa_{23}^{'}\cos\Delta_2 z\Big|_{\Delta_2 z=\pi}^{\Delta_2 z=3\pi/2} + \kappa_{24}^{'}\cos\Delta_2 z\Big|_{\Delta_2 z=3\pi/2}^{\Delta_2 z=2\pi} + \\
&\kappa_{25}^{'}\cos\Delta_2 z\Big|_{\Delta_2 z=2\pi}^{\Delta_2 z=5\pi/2} + \kappa_{26}^{'}\cos\Delta_2 z\Big|_{\Delta_2 z=5\pi/2}^{\Delta_2 z=3\pi} + \kappa_{27}^{'}\cos\Delta_2 z\Big|_{\Delta_2 z=3\pi}^{\Delta_2 z=7\pi/2} + \kappa_{28}^{'}\cos\Delta_2 z\Big|_{\Delta_2 z=7\pi/2}^{\Delta_2 z=4\pi}\Big].
\end{aligned}$$

We take the values of $\kappa_{2i}^{'}$ based on the cosine function in Fig. 14 (b). Therefore,

$$\kappa_{21}^{'}=\cos\left(\frac{\pi}{4}\right)=0.707,\qquad \kappa_{22}^{'}=\cos\left(\frac{3\pi}{4}\right)=-0.707,$$
$$\kappa_{23}^{'}=\cos\left(\frac{5\pi}{4}\right)=-0.707,\quad \kappa_{24}^{'}=\cos\left(\frac{7\pi}{4}\right)=0.707,$$
$$\kappa_{25}^{'}=\cos\left(\frac{9\pi}{4}\right)=0.707,\qquad \kappa_{26}^{'}=\cos\left(\frac{11\pi}{4}\right)=-0.707,$$
$$\kappa_{27}^{'}=\cos\left(\frac{13\pi}{4}\right)=-0.707,\ \kappa_{28}^{'}=\cos\left(\frac{15\pi}{4}\right)=0.707.$$

Substitute the values of $\kappa_{2i}^{'}$ into the integration above, we achieve

$$-i\int_0^L \kappa_2(z)\sin\Delta_2 z\cdot dz=0\,.$$

(2) The real part integration

$$\int_0^L \kappa_2(z)\cos\Delta_2 z\cdot dz=\kappa_2\cdot\Big[\int_0^{\frac{L}{8}}\kappa_{21}^{'}\cos\Delta_2 z\cdot dz+\int_{\frac{L}{8}}^{\frac{L}{4}}\kappa_{22}^{'}\cos\Delta_2 z\cdot dz+\int_{\frac{L}{4}}^{\frac{3L}{8}}\kappa_{23}^{'}\cos\Delta_2 z\cdot dz+\int_{\frac{3L}{8}}^{\frac{L}{2}}\kappa_{24}^{'}\cos\Delta_2 z\cdot dz+$$
$$\int_{\frac{L}{2}}^{\frac{5L}{8}}\kappa_{25}^{'}\cos\Delta_2 z\cdot dz+\int_{\frac{5L}{8}}^{\frac{3L}{4}}\kappa_{26}^{'}\cos\Delta_2 z\cdot dz+\int_{\frac{3L}{4}}^{\frac{7L}{8}}\kappa_{27}^{'}\cos\Delta_2 z\cdot dz+\int_{\frac{7L}{8}}^{L}\kappa_{28}^{'}\cos\Delta_2 z\cdot dz\ \Big]$$
$$=\frac{\kappa_2}{\Delta_2}\Big[\ \kappa_{21}^{'}\sin\Delta_2 z\Big|_{\Delta_2 z=0}^{\Delta_2 z=\pi/2}+\kappa_{22}^{'}\sin\Delta_2 z\Big|_{\Delta_2 z=\pi/2}^{\Delta_2 z=\pi}+\kappa_{23}^{'}\sin\Delta_2 z\Big|_{\Delta_2 z=\pi}^{\Delta_2 z=3\pi/2}+\kappa_{24}^{'}\sin\Delta_2 z\Big|_{\Delta_2 z=3\pi/2}^{\Delta_2 z=2\pi}+$$
$$\kappa_{25}^{'}\sin\Delta_2 z\Big|_{\Delta_2 z=2\pi}^{\Delta_2 z=5\pi/2}+\kappa_{26}^{'}\sin\Delta_2 z\Big|_{\Delta_2 z=5\pi/2}^{\Delta_2 z=3\pi}+\kappa_{27}^{'}\sin\Delta_2 z\Big|_{\Delta_2 z=3\pi}^{\Delta_2 z=7\pi/2}+\kappa_{28}^{'}\sin\Delta_2 z\Big|_{\Delta_2 z=7\pi/2}^{\Delta_2 z=4\pi}\ \Big]$$
$$\Rightarrow \kappa_2=2.2214\kappa_0\,,$$

and $\kappa_{2i}=\kappa_{2i}^{'}\kappa_2=2.2214\cdot\kappa_{2i}^{'}\kappa_0$, thus,

$$\kappa_{21}=1.571\kappa_0,\ \ \kappa_{22}=-1.571\kappa_0,\ \ \kappa_{23}=-1.571\kappa_0,\ \ \kappa_{24}=1.571\kappa_0,$$
$$\kappa_{25}=1.571\kappa_0,\ \ \kappa_{26}=-1.571\kappa_0,\ \ \kappa_{27}=-1.571\kappa_0,\ \ \kappa_{28}=1.571\kappa_0\,.$$

B. Single sideband EMFs channel selection

1. Channel +1, default condition: $\Delta_1 L=2\pi$, $\Rightarrow\Delta_1=\dfrac{2\pi}{L}$

Let $\kappa_1(z)=\kappa_1\cdot\kappa_{1i}^{'}$, $i=1...8$.

$$\int_0^L \kappa_1(z)e^{-i\Delta_1 z}\cdot dz = \kappa_1\cdot[\int_0^{\frac{L}{8}} \kappa_{11}' e^{-i\Delta_1 z}dz + i\int_{\frac{L}{8}}^{\frac{L}{4}} \kappa_{12}' e^{-i\Delta_1 z}dz + \int_{\frac{L}{4}}^{\frac{3L}{8}} \kappa_{13}' e^{-i\Delta_1 z}dz + i\int_{\frac{3L}{8}}^{\frac{L}{2}} \kappa_{14}' e^{-i\Delta_1 z}dz +$$
$$\int_{\frac{L}{2}}^{\frac{5L}{8}} \kappa_{15}' e^{-i\Delta_1 z}dz + i\int_{\frac{5L}{8}}^{\frac{3L}{4}} \kappa_{16}' e^{-i\Delta_1 z}dz + \int_{\frac{3L}{4}}^{\frac{7L}{8}} \kappa_{17}' e^{-i\Delta_1 z}dz + i\int_{\frac{7L}{8}}^{L} \kappa_{18}' e^{-i\Delta_1 z}dz].$$

The imaginary part of the integration is:

$$\mathrm{Im} = i\kappa_1\cdot[-\int_0^{\frac{L}{8}} \kappa_{11}' \sin\Delta_1 z\cdot dz + \int_{\frac{L}{8}}^{\frac{L}{4}} \kappa_{12}' \cos\Delta_1 z\cdot dz - \int_{\frac{L}{4}}^{\frac{3L}{8}} \kappa_{13}' \sin\Delta_1 z\cdot dz + \int_{\frac{3L}{8}}^{\frac{L}{2}} \kappa_{14}' \cos\Delta_1 z\cdot dz -$$
$$\int_{\frac{L}{2}}^{\frac{5L}{8}} \kappa_{15}' \sin\Delta_1 z\cdot dz + \int_{\frac{5L}{8}}^{\frac{3L}{4}} \kappa_{16}' \cos\Delta_1 z\cdot dz - \int_{\frac{3L}{4}}^{\frac{7L}{8}} \kappa_{17}' \sin\Delta_1 z\cdot dz + \int_{\frac{7L}{8}}^{L} \kappa_{18}' \cos\Delta_1 z\cdot dz].$$

And the real part is given as:

$$\mathrm{Re} = \kappa_1\cdot[\int_0^{\frac{L}{8}} \kappa_{11}' \cos\Delta_1 z\cdot dz + \int_{\frac{L}{8}}^{\frac{L}{4}} \kappa_{12}' \sin\Delta_1 z\cdot dz + \int_{\frac{L}{4}}^{\frac{3L}{8}} \kappa_{13}' \cos\Delta_1 z\cdot dz + \int_{\frac{3L}{8}}^{\frac{L}{2}} \kappa_{14}' \sin\Delta_1 z\cdot dz +$$
$$\int_{\frac{L}{2}}^{\frac{5L}{8}} \kappa_{15}' \cos\Delta_1 z\cdot dz + \int_{\frac{5L}{8}}^{\frac{3L}{4}} \kappa_{16}' \sin\Delta_1 z\cdot dz + \int_{\frac{3L}{4}}^{\frac{7L}{8}} \kappa_{17}' \cos\Delta_1 z\cdot dz + \int_{\frac{7L}{8}}^{L} \kappa_{18}' \sin\Delta_1 z\cdot dz]$$

Using Fig. 16(a) for the proportionality constants, substitute the following values into the integration,

$$\kappa_{11}' = \cos\left(\frac{\pi}{8}\right) = 0.9239, \qquad \kappa_{12}' = \sin\left(\frac{3\pi}{8}\right) = 0.9239,$$
$$\kappa_{13}' = \cos\left(\frac{5\pi}{8}\right) = -0.3827, \quad \kappa_{14}' = \sin\left(\frac{7\pi}{8}\right) = 0.3827,$$
$$\kappa_{15}' = \cos\left(\frac{9\pi}{8}\right) = -0.9239, \quad \kappa_{16}' = \sin\left(\frac{11\pi}{8}\right) = -0.9239,$$
$$\kappa_{17}' = \cos\left(\frac{13\pi}{8}\right) = 0.3827, \quad \kappa_{18}' = \sin\left(\frac{15\pi}{8}\right) = -0.3827,$$

it follows that Im=0, and

$$\mathrm{Re} = \frac{\pi}{2} \equiv \kappa_0 L \quad \Rightarrow \quad \kappa_1 = 2.0523\kappa_0.$$

Thus,

$$\kappa_{11} = 1.896\kappa_0, \quad \kappa_{12} = 1.896\kappa_0, \quad \kappa_{13} = -0.785\kappa_0, \quad \kappa_{14} = 0.785\kappa_0,$$

$\kappa_{15} = -1.896\kappa_0$, $\kappa_{16} = -1.896\kappa_0$, $\kappa_{17} = 0.785\kappa_0$, $\kappa_{18} = -0.785\kappa_0$.

2. Channel -1, default condition: $\Delta_{-1}L = -2\pi$, $\Delta_{-1} = -\Delta_1$

Let $\kappa_{-1}(z) = \kappa_{-1} \cdot \kappa'_{-1i}$, $i = 1...8$

The values of $\kappa'_{-1,i}$ are chosen as

$$\kappa'_{11} = \cos\left(\frac{\pi}{8}\right) = 0.9239, \qquad \kappa'_{12} = -\sin\left(\frac{3\pi}{8}\right) = -0.9239,$$
$$\kappa'_{13} = \cos\left(\frac{5\pi}{8}\right) = -0.3827, \quad \kappa'_{14} = -\sin\left(\frac{7\pi}{8}\right) = -0.3827,$$
$$\kappa'_{15} = \cos\left(\frac{9\pi}{8}\right) = -0.9239, \quad \kappa'_{16} = -\sin\left(\frac{11\pi}{8}\right) = 0.9239,$$
$$\kappa'_{17} = \cos\left(\frac{13\pi}{8}\right) = 0.3827, \quad \kappa'_{18} = -\sin\left(\frac{15\pi}{8}\right) = 0.3827.$$

Thus,

$\kappa_{11} = 1.896\kappa_0$, $\kappa_{12} = -1.896\kappa_0$, $\kappa_{13} = -0.785\kappa_0$, $\kappa_{14} = -0.785\kappa_0$,

$\kappa_{15} = -1.896\kappa_0$, $\kappa_{16} = 1.896\kappa_0$, $\kappa_{17} = 0.785\kappa_0$, $\kappa_{18} = 0.785\kappa_0$.

3. Channel +2, default condition: $\Delta_2 L = 4\pi$

Using Fig. 16(b) for the proportionality constants, take values of $\kappa'_{2,i}$ in the following way:

$$\kappa'_{21} = \cos\left(\frac{\pi}{4}\right) = 0.707, \qquad \kappa'_{22} = \sin\left(\frac{3\pi}{4}\right) = 0.707,$$
$$\kappa'_{23} = \cos\left(\frac{5\pi}{4}\right) = -0.707, \quad \kappa'_{24} = \sin\left(\frac{7\pi}{4}\right) = -0.707,$$
$$\kappa'_{25} = \cos\left(\frac{9\pi}{4}\right) = 0.707, \qquad \kappa'_{26} = \sin\left(\frac{11\pi}{4}\right) = 0.707,$$
$$\kappa'_{27} = \cos\left(\frac{13\pi}{4}\right) = -0.707, \quad \kappa'_{28} = \sin\left(\frac{15\pi}{4}\right) = -0.707.$$

It gives Im=0, and

$$\mathrm{Re} = \frac{\pi}{2} = \kappa_0 L \qquad \Rightarrow \kappa_2 = 1.55\kappa_0 .$$

$\kappa_{21} = 1.096\kappa_0$, $\kappa_{22} = 1.096\kappa_0$, $\kappa_{23} = -1.096\kappa_0$, $\kappa_{24} = -1.096\kappa_0$,

$\kappa_{25} = 1.096\kappa_0$, $\kappa_{26} = 1.096\kappa_0$, $\kappa_{27} = -1.096\kappa_0$, $\kappa_{28} = -1.096\kappa_0$.

Similarly, to select channel -2,

$\kappa_{-2,1} = 1.096\kappa_0$, $\kappa_{-2,2} = -1.096\kappa_0$, $\kappa_{-2,3} = -1.096\kappa_0$, $\kappa_{-2,4} = 1.096\kappa_0$,

$\kappa_{-2,5} = 1.096\kappa_0$, $\kappa_{-2,6} = -1.096\kappa_0$, $\kappa_{-2,7} = -1.096\kappa_0$, $\kappa_{-2,8} = 1.096\kappa_0$.

APPENDIX 2

VOLTAGE VALUES TO SELECT VARIOUS CHANNELS

(16 ELECTRODE SETS)

Table 6. Relative voltage values $(V_j)_p/V_0$ to select j^{th} channel for single sideband device, 16 electrode sets, uniform coupling, V_0=10.5V in experiment.

		Channel						
		-4	-2	-1	0	+1	+2	+4
p^{th} electrode set	1	-1.1	-0.78	-0.39	0	0.39	0.78	1.1
	2	-1.1	0.78	1.67	2	1.67	0.78	-1.1
	3	1.1	-1.89	-1.67	0	1.67	1.89	-1.1
	4	1.1	-1.89	0.39	2	0.39	-1.89	1.1
	5	-1.1	0.78	-1.97	0	1.97	-0.78	1.1
	6	-1.1	-0.78	-1.12	2	-1.12	-0.78	-1.1
	7	1.1	1.89	-1.12	0	1.12	-1.89	-1.1
	8	1.1	1.89	-1.97	2	-1.97	1.89	1.1
	9	-1.1	-0.78	0.39	0	-0.39	0.78	1.1
	10	-1.1	0.78	-1.67	2	-1.67	0.78	-1.1
	11	1.1	-1.89	1.67	0	-1.67	1.89	-1.1
	12	1.1	-1.89	-0.39	2	-0.39	-1.89	1.1
	13	-1.1	0.78	1.97	0	-1.97	-0.78	1.1
	14	-1.1	-0.78	1.12	2	1.12	-0.78	-1.1
	15	1.1	1.89	1.12	0	-1.12	-1.89	-1.1
	16	1.1	1.89	1.97	2	1.97	1.89	1.1

Table 7. Relative voltage values $(V_j)_p/V_0$ to select j^{th} channel for single sideband device, 16 electrode sets, apodized coupling, V_0=10.5V in experiment.

		Channel						
		-4	-2	-1	0	+1	+2	+4
p^{th} electrode set	1	-0.56	-0.4	-0.2	0	0.2	0.4	0.56
	2	-0.64	0.46	0.98	1.08	0.98	0.46	-0.64
	3	0.79	-1.37	-1.21	0	1.21	1.37	-0.79
	4	0.99	-1.71	0.35	1.62	0.35	-1.71	0.99
	5	-1.21	0.86	-2.17	0	2.17	-0.86	1.21
	6	-1.41	-1	-1.43	2.38	-1.43	-1	-1.41
	7	1.55	2.68	-1.58	0	1.58	-2.68	-1.55
	8	1.64	2.83	-2.94	2.92	-2.94	2.83	1.64
	9	-1.64	-1.17	0.58	0	-0.58	1.17	1.64
	10	-1.56	1.11	-2.37	2.92	-2.37	1.11	-1.56
	11	1.41	-2.42	2.13	0	-2.13	2.42	-1.41
	12	1.21	-2.08	-0.43	2.38	-0.43	-2.08	1.21
	13	-0.99	0.71	1.78	0	-1.78	-0.71	0.99
	14	-0.79	-0.57	0/81	1.62	0/81	-0.57	-0.79
	15	0.64	1.11	0.65	0	-0.65	-1.11	-0.64
	16	0.56	0.97	1	1.08	1	0.97	0.56

APPENDIX 3

INTERFEROMETER WAVEGUIDE ANALYSIS

Following Chapter III, section C, a more specific explanation of the operating principal for the waveguide interferometer with unequal arms is presented in the following.

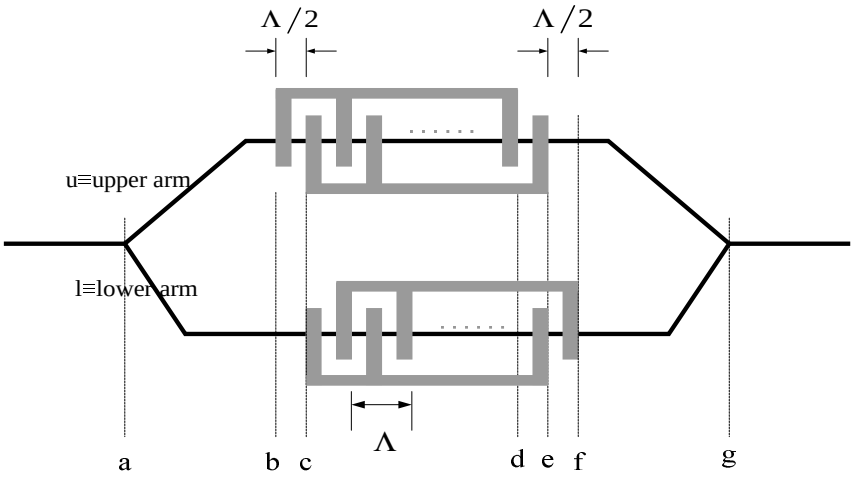

Fig. 40. Interferometer filter with unequal waveguide arms.

The interferometer filter configuration is shown in Fig. 40. In Fig. 40, the shaded parts represent the electrode grating pads and Λ is the spatial period of the perturbation. The optical path length difference from point "a" to "g" between the upper and lower waveguide arm, with upper arm longer, is $\frac{\lambda}{2}$, i.e.

$$L_{ag}^{u} - L_{ag}^{l} = \frac{\lambda}{2}.$$

Due to symmetry, the path difference from "a" to "b" between upper and lower arms is

$\frac{\lambda}{4}$, i.e.

$$L_{ab}^{u} - L_{ab}^{l} = \frac{\lambda}{4} \Rightarrow L_{ab}^{u} = L_{ab}^{l} + \frac{\lambda}{4}.$$

Assuming 3-dB splitter, which divides the power equally, then the electric fields for the lightwave are:

at point "b":

In the lower arm is

$$\mathbf{E}_{l\ (z=b)}^{w} = \frac{E_0}{\sqrt{2}} e^{-i\beta L_{ab}^{l}},$$

and in the upper arm is

$$\mathbf{E}_{l\ (z=b)}^{w} = \frac{E_0}{\sqrt{2}} e^{-i\beta L_{ab}^{u}} = \frac{E_0}{\sqrt{2}} e^{-i\beta (L_{ab}^{l} + \frac{\lambda}{4})} = \frac{E_0}{\sqrt{2}} e^{-i(\beta L_{ab}^{l} + \frac{\pi}{2})},\ (\beta = \frac{2\pi}{\lambda})$$

i.e. light at upper arm accumulates an additional phase of $\frac{\pi}{2}$ relative to lower arm. The superscript "w" indicates optical wave.

Let us consider TE polarized input for the time being, then $\beta = \beta_{TE} = \frac{2\pi}{\lambda} n_{TE}$ and let

$$\beta_{TE} L_{ab}^{l} = \frac{2\pi}{\lambda_0} n_{TE} L_{ab}^{l} \equiv \phi_{ab}^{TE}.$$

Hence

$$\mathbf{E}_{l\ (z=b)}^{w} = \frac{E_0}{\sqrt{2}} e^{-i\varphi_{ab}^{TE}}$$

$$\mathbf{E}_{u\ (z=b)}^{w} = \frac{E_0}{\sqrt{2}} e^{-i(\varphi_{ab}^{TE} + \frac{\pi}{2})}.$$

at point "e" in the upper arm:

Assuming phase match condition is satisfied at wavelength λ_0, light emerging at "e" in the upper arm fully converts to TM mode and acquires an additional phase of $\frac{\pi}{2}$ over its normal accumulated phase in the conversion region within length L_0. Thus,

$$\mathbf{E}^{w}_{u\,(z=e)} = \mathbf{E}^{w}_{u\,(z=b)} \cdot e^{-i(\beta_{TE}L_0+\frac{\pi}{2})}$$
$$= \frac{E_0}{\sqrt{2}} e^{-i(\varphi^{TE}_{ab}+\frac{\pi}{2}+\beta_{TE}L_0+\frac{\pi}{2})}.$$

at point "f" in the upper arm:

From "e" to "f", the propagating lightwave (now TM mode) accumulates a phase $\phi^{TM}_{ef} = \beta_{TM}L_{ef} = \beta_{TM}\frac{\Lambda}{2}$ with $\beta_{TM} = \frac{2\pi}{\lambda}n_{TM}$. Thus,

$$\mathbf{E}^{w}_{u\,(z=f)} = \mathbf{E}^{w}_{u\,(z=e)} \cdot e^{-i\beta_{TM}\frac{\Lambda}{2}}$$
$$= \frac{E_0}{\sqrt{2}} e^{-i(\phi^{TE}_{ab}+\frac{\pi}{2}+\beta_{TE}L_0+\frac{\pi}{2}+\beta_{TM}\frac{\Lambda}{2})}.$$

at point "c" in the lower arm:

The light maintains TE mode from "b" to "c" and acquires a phase of $\phi^{TE}_{bc} = \beta_{TE}L_{bc} = \beta_{TE}\frac{\Lambda}{2}$. Hence,

$$\mathbf{E}^{w}_{l\,(z=c)} = \mathbf{E}^{w}_{l\,(z=b)} \cdot e^{-i\beta_{TE}\frac{\Lambda}{2}}$$
$$= \frac{E_0}{\sqrt{2}} e^{-i(\phi^{TE}_{ab}+\beta_{TE}\frac{\Lambda}{2})}.$$

at point "f" in the lower arm:

Under previous assumption that phase match condition is satisfied at λ, then light at

point “f” in the lower arm fully converts to TM mode and acquires an additional phase of $\frac{\pi}{2}$ over its normal accumulated phase in the conversion region within length L_0, i.e.

$$\mathbf{E}^{w}_{l\ (z=f)} = \mathbf{E}^{w}_{l\ (z=c)} \cdot e^{-i(\beta_{TE}L_0+\frac{\pi}{2})}$$
$$= \frac{E_0}{\sqrt{2}} e^{-i(\phi^{TE}_{ab}+\beta_{TE}\frac{\Lambda}{2}+\beta_{TE}L_0+\frac{\pi}{2})}.$$

at point “g”(final):

Again, due to symmetry, there is $\frac{\lambda}{4}$ phase difference between upper and lower arm from point “f” to “g”, with upper arm longer. We have:

in lower arm,

$$\phi^{l}_{fg} = \beta_{TM} \cdot L_{\ fg} \equiv \phi^{TM}_{fg};$$

and in upper arm,

$$\phi^{u}_{fg} = \beta_{TM} \cdot (L_{\ fg} + \frac{\lambda}{4}) = \beta_{TM} L_{\ fg} + \frac{2\pi}{\lambda} \cdot \frac{\lambda}{4} \equiv \phi^{TM}_{fg} + \frac{\pi}{2}.$$

Also in the tapered section at output, 2 modes (symmetric and asymmetric) are excited, i.e. intensity from each arm drops by $\frac{1}{2}$, therefore E^w drops by another $\frac{1}{\sqrt{2}}$ factor. Thus,

$$\mathbf{E}^{w}_{u\ (z=g)} = \mathbf{E}^{w}_{u\ (z=f)} \cdot e^{-i(\phi^{TM}_{fg}+\frac{\pi}{2})}$$
$$= \frac{E_0}{\sqrt{2}} e^{-i(\phi^{TE}_{ab}+\frac{\pi}{2}+\beta_{TE}L_0+\frac{\pi}{2}+\beta_{TM}\frac{\Lambda}{2}+\phi^{TM}_{fg}+\frac{\pi}{2})} \cdot \frac{1}{\sqrt{2}}$$

and

$$\mathbf{E}^{w}_{l\ (z=g)} = \mathbf{E}^{w}_{l\ (z=f)} \cdot e^{-i\phi^{TM}_{fg}}$$
$$= \frac{E_0}{\sqrt{2}} e^{-i(\phi^{TE}_{ab} + \beta_{TE}\frac{\Lambda}{2} + \beta_{TE}L_0 + \frac{\pi}{2} + \phi^{TM}_{fg})} \cdot \frac{1}{\sqrt{2}}.$$

The total electrical field at the output is

$$\mathbf{E}^{w}_{out} = \mathbf{E}^{w}_{u\ (z=g)} + \mathbf{E}^{w}_{l\ (z=g)}.$$

The output light intensity can be expressed as

$$I_{out} = \left|\mathbf{E}^{w}_{out}\right|^2 = (\mathbf{E}^{w}_{out}) \cdot (\mathbf{E}^{w}_{out})^*,$$

with: $$\mathbf{E}^{w}_{out} = \frac{E_0}{\sqrt{2}} e^{-i(\phi^{TE}_{ab} + \beta_{TE}L_0 + \phi^{TM}_{fg} + \frac{\pi}{2})} \cdot [e^{-i(\beta_{TM}\frac{\Lambda}{2} + \pi)} + e^{-i\beta_{TE}\frac{\Lambda}{2}}] \cdot \frac{1}{\sqrt{2}}.$$

Hence:

$$I_{out} = \left|\mathbf{E}^{w}_{out}\right|^2 = (\mathbf{E}^{w}_{out}) \cdot (\mathbf{E}^{w}_{out})^*$$
$$= (\frac{E_0}{2})^2 [(e^{-i(\beta_{TM}\frac{\Lambda}{2} + \pi)} + e^{-i\beta_{TE}\frac{\Lambda}{2}}) \cdot (e^{+i(\beta_{TM}\frac{\Lambda}{2} + \pi)} + e^{+i\beta_{TE}\frac{\Lambda}{2}})]$$
$$= \frac{E_0^2}{4} [1 + e^{-i(\beta_{TM}\frac{\Lambda}{2} + \pi - \beta_{TE}\frac{\Lambda}{2})} + e^{-i(\beta_{TE}\frac{\Lambda}{2} - \beta_{TM}\frac{\Lambda}{2} - \pi)} + 1]$$
$$= \frac{E_0^2}{4} [2 + 2(\frac{e^{-i[(\beta_{TM} - \beta_{TE})\frac{\Lambda}{2} + \pi]} + e^{+i[(\beta_{TM} - \beta_{TE})\frac{\Lambda}{2} + \pi]}}{2})]$$
$$I_{out} = \frac{E_0^2}{4} (2 + 2\cos[(\beta_{TM} - \beta_{TE})\frac{\Lambda}{2} + \pi]).$$

For phase-matched wavelength $\lambda=\lambda_0$, $\Lambda = \frac{\lambda_0}{\Delta n}$.

Therefore: $$(\beta_{TM} - \beta_{TE})\frac{\Lambda}{2} = \frac{2\pi}{\lambda}\Big|_{\lambda=\lambda_0} \cdot (n_e - n_o) \cdot \frac{1}{2}\frac{\lambda_0}{\Delta n} = \pi,$$

hence: $$I_{out} = \frac{E_0^2}{4}(2 + 2\cos(2\pi)) = \frac{E_0^2}{4}(2+2) = E_0^2.$$

And if $\lambda \neq \lambda_0$, phase match condition is not satisfied and mode conversion does not

occur, causing the total phase difference between the upper and lower arm to be π at the output point "g". Hence, $I_{out} \to 0$.

By similar procedure, when the incident light is TM polarized, we also get $I_{out} = E_0^2$ for phase matched wavelength $\lambda=\lambda_0$ and $I_{out} = 0$ otherwise. In summary, for any polarized light at the input, the filter will route the light to the output only if the wavelength satisfies the phase match condition. If the phase match condition is not satisfied, the second-order (asymmetric) mode is encountered in the output branch and will be cut off by the single-mode output waveguide [38].

Fig. 41 illustrates this behavior in a symmetric Mach-Zehnder interferometer structure.

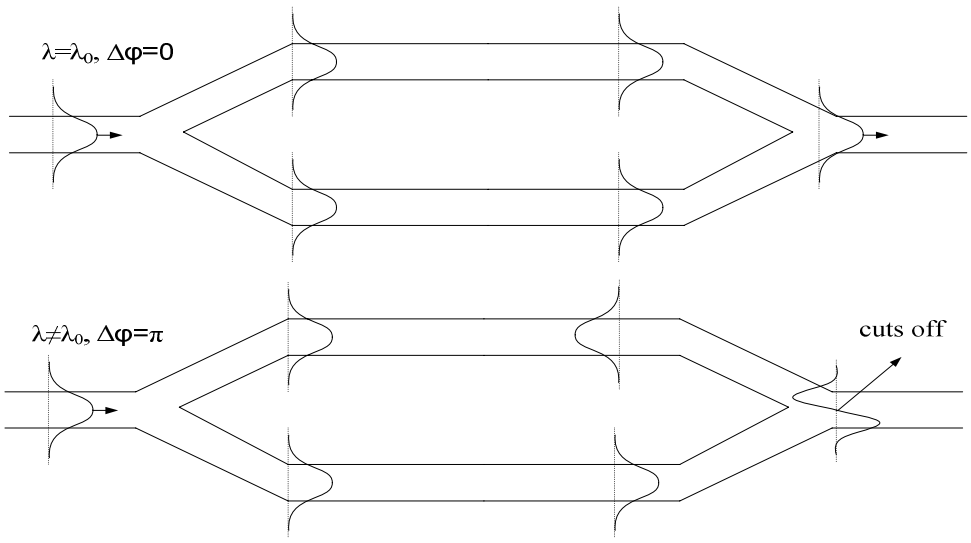

Fig. 41. Operation of the symmetric interferometric modulators with zero phase difference between the arms and π phase difference.

APPENDIX 4

THEORETICAL ANALYSIS IN MATLAB PROGRAM FOR EMF DEVICE

(16 ELECTRODE SETS)

```
function f=EMF16(M, sideband, channel, apodize)

%%%%%%%%%%%%%%%%%%%%%%%%%%%%%%%%%%%%%%%%%%%%%%%%%%%%%%%%%%%%
% Program written for the tunable EMF converter analysis
% for 16 electrode sets
% June, 2006
%%%%%%%%%%%%%%%%%%%%%%%%%%%%%%%%%%%%%%%%%%%%%%%%%%%%%%%%%%%%
% M: 0.1M nm will be the plot range for wavelength
% sideband: 1 for single sideband, 2 for two sideband
% channel: channel #, eg. -4
% apodize: 0 for non-apodized, 1 for apodized


if (sideband==2 && channel<0)
      Warning={'For 2 sideband, channel # can not be negative'}
      return;
end

if (abs(channel)>4)
      Warning={'Please input channel number between -4 and 4'}
      return;
end

% electrodes grating period, unit: meter
period=21e-6;
% center wavelength, unit: meter
lambda=1528.88e-9;
% birefrigence for Lithium Niobate
delta_n=lambda/period; %0.072804 for 1528.88;
% group index difference
delta_n_gr=0.08;
% L is the length of each polarization coupling region, unit: meter
L0=64*period;      % Assuming 64 periods per set

L=L0*[1 1 1 1 1 1 1 1 1 1 1 1 1 1 1 1];
% k0 is the value for uniform voltage
k0=pi/(2*16*L0);
```

```
kk=zeros(9,16,2);

a=[0.5:1:15.5]/16;

%raised cosine
t=[0.5:1:15.5]/16;
apo=1+0.5*cos(2*pi*(t-0.5));


%0 channel, 2 sideband
kk(5,:,2)=k0*[1 1 1 1 1 1 1 1 1 1 1 1 1 1 1 1];    % 2 sideband

%+/-1 channel, 2 sideband
b=cos(2*pi*a);
kk(6,:,2)=2*k0*b;    % good

%+/-2 channel,    2 sideband
c=cos(4*pi*a);
kk(7,:,2)=2*k0*c;    % good

%+/-3 channel,    2 sideband
c3=cos(6*pi*a);
kk(8,:,2)=2*k0*c3;    % good

%+/-4 channel,    2 sideband
c4=cos(8*pi*a);
kk(9,:,2)=2*k0*c4;    % good

%0 channel, 1 sideband.
kk(5,:,1)=k0*[2 0 2 0 2 0 2 0 2 0 2 0 2 0 2 0];    % 1 sideband

%-1 channel, 1 sideband.
d=cos(2*pi*a);
e=sin(2*pi*a);
f1=[d(1) e(2) d(3) e(4) d(5) e(6) d(7) e(8) d(9) e(10) d(11) e(12) d(13) e(14) d(15) e(16)];
kk(4,:,1)=2.0129*k0*f1;    % good

%+1 channel, 1 sideband.
f_1=[d(1) -e(2) d(3) -e(4) d(5) -e(6) d(7) -e(8) d(9) -e(10) d(11) -e(12) d(13) -e(14) d(15)
-e(16)];
kk(6,:,1)=2.0129*k0*f_1;    % good

%-2 channel, 1 sideband.
g=cos(4*pi*a);
```

```
h=sin(4*pi*a);
ii2=[g(1) h(2) g(3) h(4) g(5) h(6) g(7) h(8) g(9) h(10) g(11) h(12) g(13) h(14) g(15)
h(16)];
kk(3,:,1)=2.0523*k0*ii2;    % good

%+2 channel, 1 sideband.
ii_2=[g(1) -h(2) g(3) -h(4) g(5) -h(6) g(7) -h(8) g(9) -h(10) g(11) -h(12) g(13) -h(14) g(15)
-h(16)];
kk(7,:,1)=2.0523*k0*ii_2;    % good

%-3 channel, 1 sideband.
g3=cos(6*pi*a)./L*L0;
h3=sin(6*pi*a)./L*L0;
ii3=[g3(1) h3(2) g3(3) h3(4) g3(5) h3(6) g3(7) h3(8) g3(9) h3(10) g3(11) h3(12) g3(13)
h3(14) g3(15) h3(16)];
kk(2,:,1)=2*k0*ii3;    % channel 5 also selected

%+3 channel, 1 sideband.
ii_3=[g3(1) -h3(2) g3(3) -h3(4) g3(5) -h3(6) g3(7) -h3(8) g3(9) -h3(10) g3(11) -h3(12)
g3(13) -h3(14) g3(15) -h3(16)];
kk(8,:,1)=2*k0*ii_3;    % good

%-4 channel, 1 sideband.
g4=cos(8*pi*a);
h4=sin(8*pi*a);
ii4=[g4(1) h4(2) g4(3) h4(4) g4(5) h4(6) g4(7) h4(8) g4(9) h4(10) g4(11) h4(12) g4(13)
h4(14) g4(15) h4(16)];
kk(1,:,1)=1.571*k0*ii4;    % good

%+4 channel, 1 sideband.
g4=cos(8*pi*a);
h4=sin(8*pi*a);
ii_4=[g4(1) -h4(2) g4(3) -h4(4) g4(5) -h4(6) g4(7) -h4(8) g4(9) -h4(10) g4(11) -h4(12)
g4(13) -h4(14) g4(15) -h4(16)];
kk(9,:,1)=1.571*k0*ii_4;    % good


k=kk(5+channel,:,sideband);
if (apodize==1)
      k=k.*apo;
end


for NA=1:2*M+1; % change the step-length from -0.02M to 0.02M nm
      na=NA-M-1;
```

```
x(NA)=na*0.02;
delta=x(NA)*pi/(period*lambda*1e9)*delta_n_gr/delta_n;
% accurancy of delta Lamda is 0.02nm

%initialize the matrixrix
matrix=[1;0];

delta_nn=delta*(lambda+0.02*1e-9*na)/pi+(lambda+0.02*1e-9*na)/period;

%transfer matrix between coupling regions
if (sideband==1)
    phase1=pi*delta_n*7.75*period/(lambda+x(NA)*1e-9); % 7.75 for 1 sideband
    phase2=pi*delta_n*8.25*period/(lambda+x(NA)*1e-9); % 8.25 for 1 sideband
else
    phase1=pi*delta_n*8*period/(lambda+x(NA)*1e-9);     % 8 for 2 sideband
    phase2=pi*delta_n*8*period/(lambda+x(NA)*1e-9);     % 8 for 2 sideband
end
M1=[exp(-j*phase1) 0; 0 exp(j*phase1)]; % 1 sideband
M2=[exp(-j*phase2) 0; 0 exp(j*phase2)]; % 2 sideband

for ii=1:16
    miu=sqrt(k(ii)^2+delta^2);
    if miu~=0
        Ac=cos(miu*L(ii))+j*delta/miu*sin(miu*L(ii));
        Bc=-j*k(ii)/miu*sin(miu*L(ii));
    else
        Ac=cos(miu*L(ii));
        Bc=0;
    end
      matrix=[Ac*exp(-j*delta*L(ii)) Bc*exp(-j*delta*L(ii));
-conj(Bc)*exp(j*delta*L(ii)-j*2*pi*delta_nn/(lambda+x(NA)*1e-9)*L(ii))
conj(Ac)*exp(j*delta*L(ii)-j*2*pi*delta_nn/(lambda+x(NA)*1e-9)*L(ii))]*matrix;
    if ii~=16
        if (ii/2)==round(ii/2)
            matrix=M2*matrix;
        else
            matrix=M1*matrix;
        end
    end

end

y(NA)=10*log10((abs(matrix(2,1)))^2);% calculate the transfer function
if y(NA)<-60
    y(NA)=-60;
```

```
    end
end

%store voltage distribution
ffid=fopen('16vol.txt','wt');
for c=5:9
    fprintf(ffid,'%d\t',c-5);
    fprintf(ffid,'%5.3f ',kk(c,:,2)/k0);
    fprintf(ffid,'\n');
end
for c=1:9
    fprintf(ffid,'\n');
    fprintf(ffid,'%d\t',c-5);
    fprintf(ffid,'%5.3f ',kk(c,:,1)/k0);
end

x=x+lambda*1e9;
q=[x;y];
fid=fopen('EMF16.txt','wt');
fprintf(fid,'%8.4f        %6.2f\n', q);
fclose('all');
plot(x,y,'k');
set(gca,'FontSize',24);
xlabel('Wavelength shift (nm)');
ylabel('Relative Power (dB)');
axis([-inf inf -30 0]);
% Peak wavelength and FWHM
[C,I] = max(y);
Peak_wavelength=(I-M-1)*0.02;
t=I;
while y(t)>=-3
    t=t+1;
end
FWHM=2*((t-M-1)*0.02-Peak_wavelength)
digits(6)
Peak_wavelength=vpa((I-M-1)*0.02+lambda*1e9)
```

APPENDIX 5

FABRICATION PROCEDURE OF TUNABLE WAVELENGTH FILTER

- Dicing $LiNbO_3$ substrate (x-cut, y-propagation) into proper size. Clean samples with proper solvents.
- Deposit Ti film by DC Sputtering.
- Delineate waveguide pattern by positive photolithography process.
- Vacuum hard bake the photoresist and O_2 descum.
- Dry etch Ti film using reactive ion etching (RIE).
- Wet etch to remove residual Ti using diluted HF acid.
- Diffuse delineated Ti pattern.
- Polish end edges.
- Deposit SiO_2 film with RF Sputtering system.
- Anneal samples in wet O_2 ambient @ 900^oC for ~ 25 mins.
- Deposit 1800Å Al metal film with E-Beam evaporation and delineate electrodes pattern.
- Wire bonding to electrodes.

APPENDIX 6

CUTTING A SUBSTRATE WITH THE DICING SAW

- Mount blue tape and stick $LiNbO_3$ wafer on the tape.
- Turn on 4 knobs/switches for saw: air knob under bench (by heater &oil polisher, black); vacuum pump power switch under saw (silver); vacuum line switch (black, flip up); water line valve under saw (yellow)
- MEASURE RESISTANCE BETWEEN BLADE AND SPINDLE! Should be less than 1 or 2 kΩ (use lowest reading).
- **R** Turn on saw power (big red button).
- Select program button and check parameters, program 300 is used.
- Mode 30, speed=0.127 mm/s, 25000 rpm.
- For 1mm thick $LiNbO_3$ wafer, Height = 0.89 mm, Thickness=1.1mm.
- **R** Turn spindle on.
- Zero chuck (be prepared to press RESET if blade cuts into chuck).
- **R** Vapor lock wafer onto platform.
- Press ALIGN, align stage/sample with crosshairs using panel on right.
- Make a test cut on tape but not on the sample (to cut -- press SINGLE CUT).
- Align the substrate with cross hairs and cut.
- When finished, do steps marked R in reverse order to shut down system.

APPENDIX 7

SUBSTRATE CLEANING PROCEDURE

- Brush with a Q-tip using soapy water.
- Rinse thoroughly with D.I. water.
- Sonicate in Acetone for 10 minutes.
- Rinse with Methanol.
- Sonicate in Methanol for 10 minutes.
- Rinse with D.I. water.
- Sonicate in soap water for 10 minutes.
- Rinse with D.I. water.
- Sonicate in D.I. water for 10 minutes.
- Brush gently with a Q-tip using Methanol.
- Blow dry with N_2.
- Check sample surface under microscope.

APPENDIX 8

DC SPUTTERING PROCESS

- Vent the bell jar and load sample(s).
- Close bell jar and turn on mechanical pump on the back.
- Turn on ‘Chamber Roughing Valve’ and wait until roughing pressure below 50μm.
- Close Chamber Roughing Valve and open high vacuum valve all the way.
- Heat the chamber @ 60^{o}C for 40 mins.
- Wait about 2 hours until the pressure is below $3x10^{-6}$ Torr.
- Turn on the cooler for thickness monitor and set temperature @ 20 ˚C.
- Ar gas flow rate @ 140 sccm.
- Adjust high vacuum valve to make Hastings vacuum gauge @ 20 μm.
- Set thickness monitor.
- Turn on power supply and push the red button, turn dial slowly (to right).
- Sputtering condition (current: 40 mA).
- ~15 minutes pre-sputtering (check current frequently)
- Start deposition by adjusting sample position. Adjust voltage to fix current @ 40mA, but do not increase voltage more than 3600V.
- After finishing deposition, turn dial left, turn off power supply.
- Close LEAK valve and turn off Ar gas flow switches, close Ar gas duel.
- Wait for more than 2 hours before unload sample(s).

APPENDIX 9

POSITIVE PHOTOLITHOGRAPHY PROCESS

- Dehydrate sample @ 135°C for 5 minutes.
- Let sample cool for 10 minutes.
- Spin AZ5214 photoresist for 30 sec @ 5000 rpm.
- Soft bake sample for 2 minutes @ 100°C.
- Let sample cool for 10 minutes.
- Expose UV with mask for 3 seconds @ 10.5mW/cm^2 without filter.
- Develop in MF312:H_2O (1:1.2) solution for about 30~40 seconds.
- Thoroughly rinse sample in water.
- Soft blow dry with Nitrogen.

APPENDIX 10

O_2 PLASMA ASHING

- Vent and load sample into barrel asher.
- Pump chamber and O_2 line down to a pressure of 50 μm.
- Establish O_2 flow so that the chamber pressure is 500 μm.
- Turn on forward RF power to 100 watts.
- Tune RF system so that reflected power is less than 5 watts.
- Run RF for 5 minutes.
- Turn off power. Vent and take out sample.

APPENDIX 11

REACTIVE ION ETCH (RIE)

- Turn on the main power.
- Vent and load sample(s).
- Turn on mechanical pump.
- Open soft roughing line till pressure drops below 7000μm.
- Close soft roughing line, open high vacuum valve, turn on blower
- Wait until pressure drops below 20μm, turn throttle valve to auto.
- Wait until the pressure stabilizes at 70μm, then turn on the gases:

  Gas flow rate (reading): CHF_3 ~ 30 sccm, Ar ~ 3 sccm, He ~ 8 sccm.
- Wait until the flows stabilize, turn on RF power, adjust forward power to 350W, tune reflected power to 0, and start etching.
- After finishing etching, turn off RF power, close gases, turn throttle valve to open, wait 2 minutes.
- Close high vacuum valve, turn off Baratron and blower, vent chamber, take out samples.

APPENDIX 12

TITANIUM IN-DIFFUSION PROCESS

- Load cleaned sample onto alumina (Al_2O_3) sample holder, and put sample holder in the center of alumina tube.
- Use glass rod to push alumina tube to the center of quartz tube.
- Seal tube with quartz cap at front and connect to bubbler.
- Turn on compressed air and adjust airflow at the back of furnace.
- Adjust settings for desired temperature.
- Wait until the airflow stabilizes at 1 bubble/sec and then turn on control switch.
- Wait until current meter stabilizes then turn on element switch.
- It takes about 45 minutes for furnace to heat over 1000°C.
- When current meter starts to swing on/off, begin counting diffusion time.
- Maintain bubbling rate at 1 bubble/second at front during the process
- After completion of the diffusion, turn off element and control switch.
- After temperature drops below 200°C, close gas and open the front end by removing the quartz cap.
- After furnace fully cools down, take out alumina tube and the sample.

APPENDIX 13

POLISHING PROCESS

Mounting

- Apply one small drop of UV epoxy (Norland optical adhesive P/N 8101) to the waveguide surface of one sample.
- Place a second sample upside-down on top of the first sample so that the waveguide surfaces are together.
- Secure samples into polishing mount so that they protrude 2-3 millimeters.
- Expose under ultra-violet light for 10 minutes at each end to cure epoxy.

Rough polish

- Secure mount to polishing fixture.
- Mix 0.5 teaspoon of polishing grit with lapping oil and spread mixture evenly over the rough polishing plate.
- Polish at speed 6 RPM for approximately 10-15 minutes (just enough to plane the surface).
- Unfasten mounting fixture from polishing fixture and clean.

Fine polishing

- Mix 3 μm diamond polishing grit with water, soap and suspendex following recipe for proportions.
- Pour onto polishing wheel and into polishing tray.
- Put polishing jig onto the plate.

- Turn on pump to circulate slurry mixture.
- Polish for 60 minutes at 16 rpm.
- Clean all equipment thoroughly.
- Repeat fine polishing procedure with 0.3 μm diamond polishing grit.
- Polish for 45 minutes at 16 rpm.

Dissolve epoxy

- Soak sample in MF312 until it separates.
- Rinse thoroughly with water.
- Inspect edges quality and cleanness under microscope before optical testing.

APPENDIX 14

E-BEAM EVAPORATION PROCEDURE

Check Thickness Monitor

- Turn on thickness monitor. The light should flash twice. If it keeps flashing, there is something wrong with the thickness monitor.

Vent the system

- Flip on the control and make sure roughing valve and Hi-vacuum valve are closed.
- Open the N_2 gas tank; turn on the vent switch and open the valve in the back.

Load sample(s)

Pump down system

- Close the lid.
- Turn on the mechanical pump and open roughing valve. Pump until pressure <50μm.
- Close the roughing valve. Open Hi-vacuum valve in the back.
- Pump until the system pressure is less than $5x10^{-6}$ torr.

Set the thickness monitor

- Turn power on.
- Set the keyboard switch to Program. Set Control PWR to Auto.
- Set density, Z-ratio and tooling.
- Reset Keyboard switch to Lock and reset Control PWR to Main Power.
- Press ZERO button.

Deposition

- Open cooling water for thickness monitor and target gun. Wait until temperature stabilizes.
- Deposition.
- Rotate the crucible if you’re using more than one and repeat (be sure to plug off the main power while rotating)
- Turn off the ionization gauge
- Wait for 5 min and turn off the power supply
- Wait for 15 min, close cooling water for crystal and turn off crystal cooler.
- Wait for 45 minutes and close other cooling water under the front panel.
- Close Hi vacuum (Gate switch).
- Turn off control.

APPENDIX 15

RF SPUTTERING PROCESS

Sample loading

- Make sure the roughing valve and high vacuum valve are closed. Open vent switch on side (left side black switch below chamber).
- When top cover pops up, close vent valve and N2 cylinder. Raise the cover using toggle switch in front.
- Load sample and close the shutter. Bring down the cover using toggle switch.
- Turn on mechanical pump and open roughing valve.
- When chamber pressure is below 70μm on hasting DV-6 gauge, close the roughing valve and open high vacuum valve(CCW) all the way(Slowly at first).
- Heat the chamber for 45 min @ 50ºC. Turn on substrate chiller and target chiller.
- Wait until a gauge value of ~ 5×10^{-6} torr is reached for the chamber pressure.
- Open gas and establish gas flows of 8.5sccm for O_2, and 30sccm for Ar. Wait 15mins for the flow to stabilize.
- Close high vacuum until vacuum gauge show around 15. Wait for 10 min again.

RF sputtering

- Turn Main Power Switch "on" (black breaker-like switch on bottom at front of power supply). Wait till DRIVE light is on (takes 1 min).
- Push "Exiter" switch from “Test” to “Operate” position - should see interlock light come on and DRIVE will be off.

- Make sure RF output dial is closed - CCW all the way. Then push RF button ON.
- Dial RF knob slowly to 0.1 kW and minimize reflected power
- Close high vacuum almost all the way until plasma ignites. Gradually open high vacuum valve to lower down the chamber pressure to ~15μm range.
- Minimize reflected power to zero by adjusting two dial knobs.
- Increase RF power to 0.3 kW. Voltage should be ~ 1.1 KV.
- Minimize reflected power to zero.
- Pre-sputter for 15 mins. After plasma stabilizes, open shutter.
- Minimize reflected power to zero if necessary.
- For 1mm thick $LiNbO_3$ substrate, it takes about 50 mins to deposit 1700 Å thick SiO_2 film.

PARAMETERS

Vac: $4\sim5*10^{-6}$

Ar: 30sccm, O2: 8.5sccm, sputter pressure: 15 μm of Mercury

Substrate temperature during deposition: 15ºC

Terminate Deposition

- Close shutter and decrease RF dial to “0”, plasma goes out.
- Push “off” button , flip Exite switch to “Test" position.
- Close Ar and O_2 gas tanks while leaving gas flow switches still open for 5 mins.
- Close gas flow switch.
- Open high vacuum valve all the way and wait for 15 mins. Then close high vacuum valve.

- Chiller for target and substrate should be left on for 30 mins after deposition.
- Turn off Main Power on RF (black breaker like switch at front bottom.) 15 mins after deposition.
- Do not open chamber immediately, wait ~1 hr to unload sample.

APPENDIX 16

EMF MASK LAYOUT I: COMPLETE DEVICE OVERVIEW

Fig. 41 represents the schematic of wiring assembly. Details are given below.

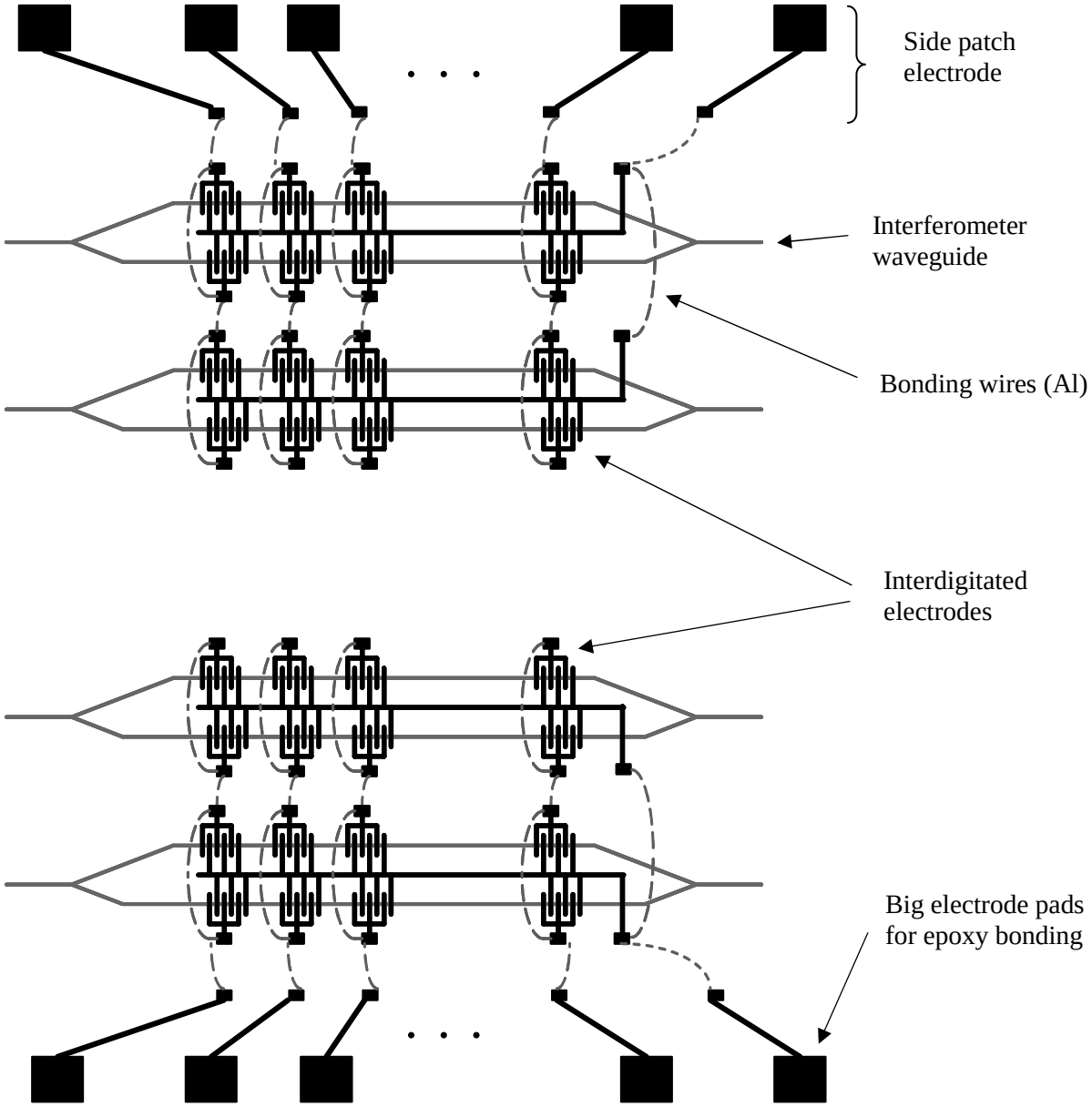

Fig. 42. Complete EMF device layout.

The side patch electrode configurations were produced on available previously-used $LiNbO_3$ substrates that were cut approximately 46×10 mm, by depositing 2000Å thick aluminum by e-beam evaporation then delineating the pattern by positive photolithography and wet etching. A pair of such patch electrode pieces were butted against the length of the sample containing EMF devices (one piece on each side), and the assembled group was then bonded on a Si chip using super glue for adhesion. Wire bonding (25μm diameter, Al) was used to interconnect the small pads as shown in Fig. 41. Electrical wires were bonded to the large pads using conductive epoxy and their other ends were snapped into the DAC output patch cord. A schematic perspective of a final assembly configuration is illustrated in Fig. 19.

APPENDIX 17

EMF MASK LAYOUT II: INTERFEROMETERS & CONVERTERS

WAVEGUIDES LAYOUT

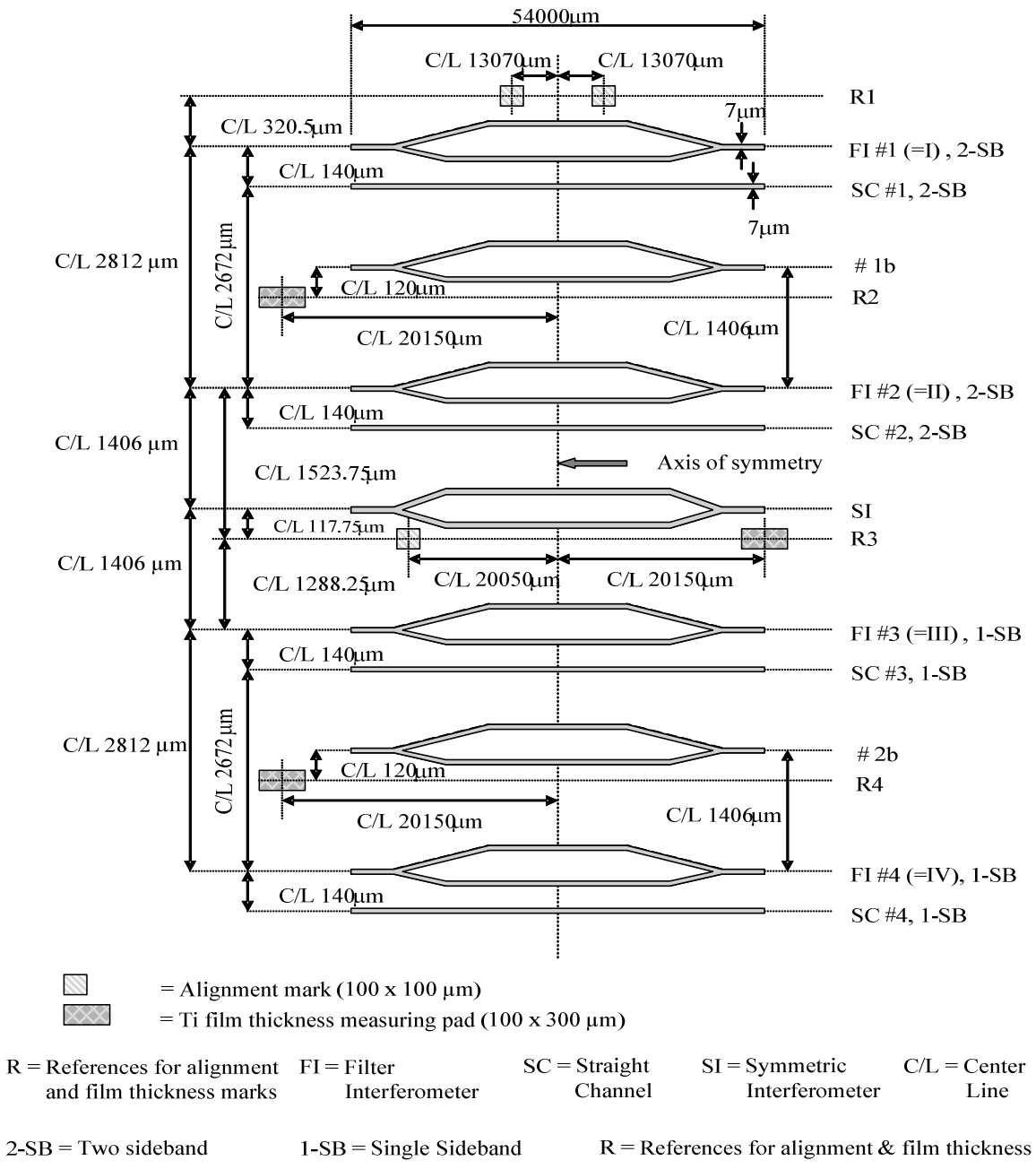

Fig. 43. Interferometers & converters waveguides layout.

APPENDIX 18

EMF MASK LAYOUT III: INTERFEROMETER WAVEGUIDE DETAILS

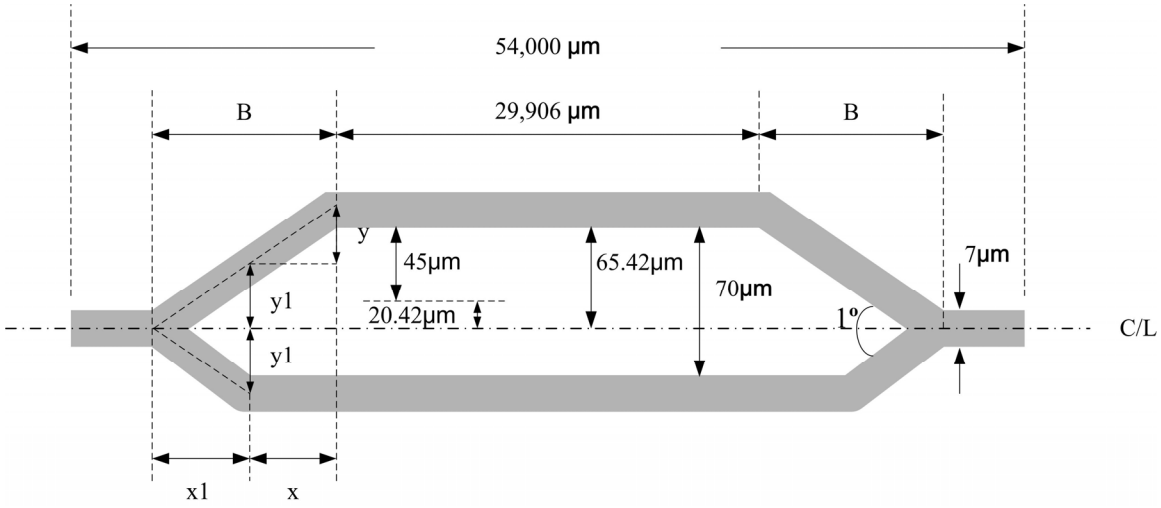

Note: dimension x_1, y_1, x, y and B refer to center dashed lines which are the axes of waveguides.

Fig. 44. Detailed configuration of interferometer waveguides.

Table 8. Detailed dimension of interferometers.

Device	FI#1, FI#2, FI#3, FI#4	SI	FI#1b, FI#2b
x_1 [µm]	3217.83	5557.55	3224.27
y_1 [µm]	28.08	48.50	28.14
x [µm]	4679.44	0	4666.56
y [µm]	40.84	0	40.72
B [µm]	7897.27	5557.55	7890.83

APPENDIX 19

EMF MASK LAYOUT IV: ELECTRODE FINGERS DIMENSIONS

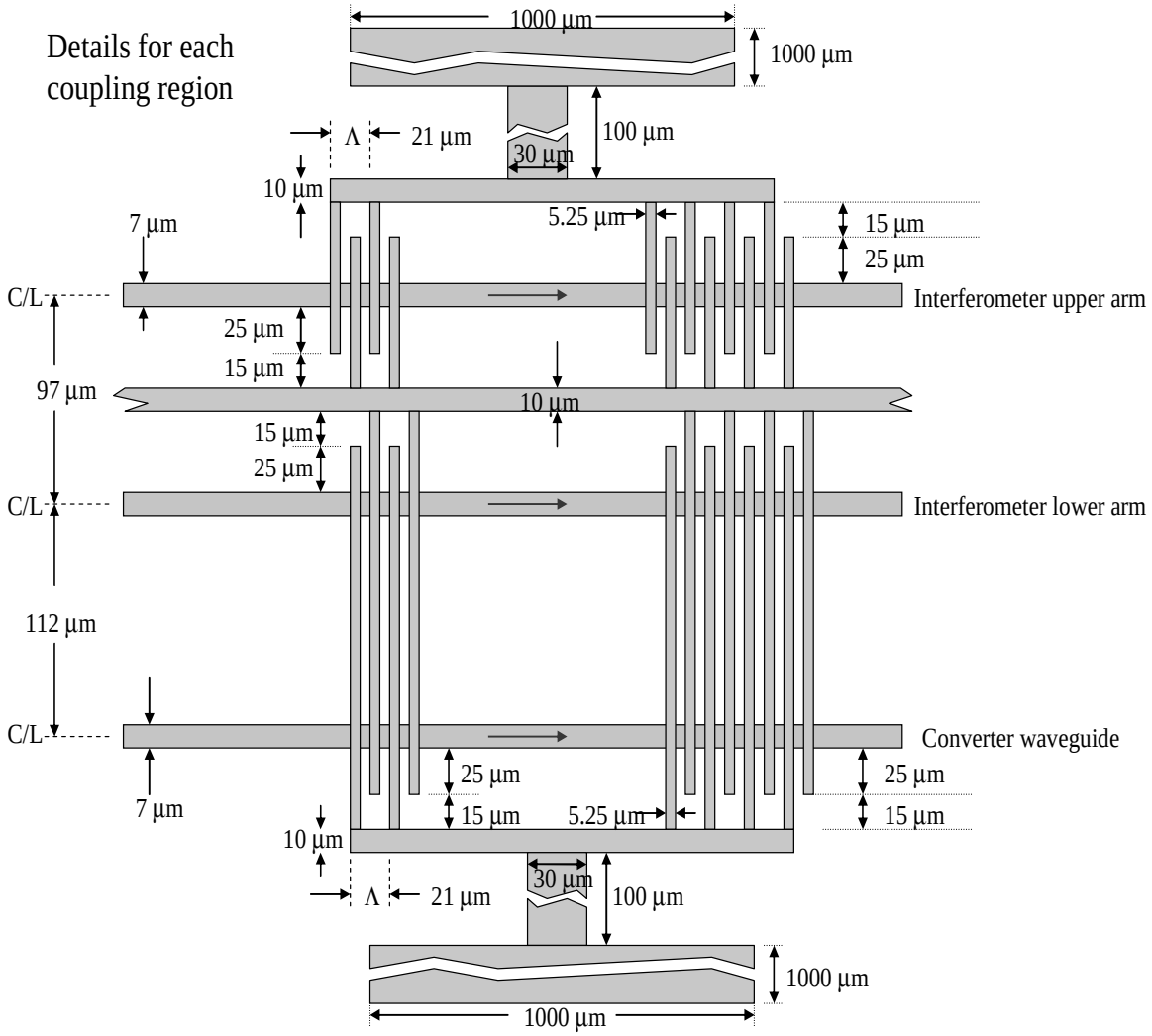

Fig. 45. Electrode fingers dimensions.

APPENDIX 20

EMF MASK LAYOUT V: SIDE PATCH ELECTRODES PATTERN

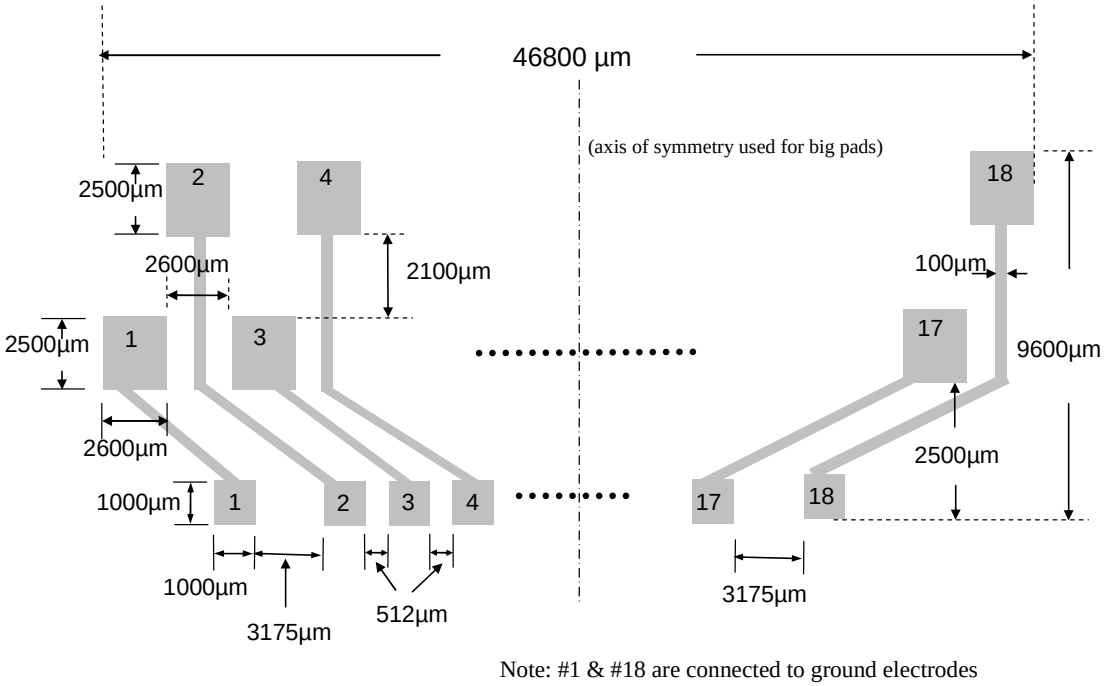

Fig. 46. Side patch electrodes layout.

VITA

Yang Ping was born in Hangzhou, Zhejiang Province, People's Republic of China. He received a B.S. in electronic engineering from Tsinghua University (P. R. China) in July 2000. Upon graduation, he attended Texas A&M University in August 2000 and received his M.S. degree in electrical engineering in August 2003. He received his Ph.D. degree in electrical engineering in December 2006. He can be reached at the following address:

Yang Ping

Department of Electrical and Computer Engineering

c/o Dr. O. Eknoyan

Texas A&M University

College Station, TX 77843-3128

USA